UNIVERSITY OF CALIFORNIA
RIVERSIDE

Facilitating Work With Photons Via Photomechanical Crystals and Multi-Exciton Materials

A Dissertation submitted in partial satisfaction
of the requirements for the degree of

Doctor of Philosophy

in

Chemistry

by

Adam Berges

September 2022

Dissertation Committee:
Dr. Christopher J. Bardeen, Chairperson
Dr. Leonard Mueller
Dr. James Davies

The Dissertation of Adam Berges is approved:

_____

_____

_____

Committee Chairperson

University of California, Riverside

Acknowledgements

"I leave Sisyphus at the foot of the mountain! One always finds one's burden again. But Sisyphus teaches the higher fidelity that negates the gods and raises rocks. He too concludes that all is well. This universe henceforth without a master seems to him neither sterile nor futile. Each atom of that stone, each mineral flake of that night filled mountain, in itself forms a world. The struggle itself toward the heights is enough to fill a man's heart. One must imagine Sisyphus happy."

— *The Myth of Sisyphus*, Albert Camus

I would first like to express my gratitude to my professor, Dr. Christopher J. Bardeen. There are few graduate students who've had the luxury of working for such an earnest, compassionate, and talented professor. Throughout the failures that inevitably come with science, Chris has offered guidance that has made me both a better researcher and scientist, giving me the tools to overcome those failures. Even when my ideas seem far-fetched or risky, Chris supported my curiosities and allowed me to take those chances and learn from my mistakes. He is a quick-witted, passionate mentor who is always open to criticism for the sake of facilitating good science. I cannot think of another person who is as talented and humble as Chris, and I will forever be grateful for the mentorship he has provided me. Next, I would like to thank Dr. Kerry Hanson for her guidance, consultation, and mentorship that has made the troubles that follow graduate school surmountable. Her perspective on microscopy, industry, and consultation is invaluable and has done much to orient me during my PhD.

I could not have accomplished nearly as much as I have by myself alone and have my wonderful coworkers, colleagues, and mentors to thank: Dr. Miguel Isararraz, Dr. Chad Cruz, Dr. Fei Tong, Dr. Hossein Mostafavi, Dr. Wangxiang Li, Dr. Xinning Dong, Emily Li, Nathan Tierce, Brandon Lui, Thomas Gately, Taylor Lewis, Touhid Bin Anwar,

Pranaya Ghate, Kevin Lam, and Marielle Sewell. Their jokes, advice, and cooperation made graduate school all the more bearable and I cherish the time I've spent with them. I would like to also express my gratitude to my wonderful collaborators for their indispensable help: Dr. Rabih Al-Kaysi, Dr. Wenwen Xu, Dr. Katharina Broch, and Dr. Ryan Hayward.

To my parents and family, whose hard work, dedication, and support has enabled me to make it this far in life: I love you dearly and I am grateful for the opportunities you've afforded me. Life has not been the kindest to us, but we have persevered, nonetheless. To my best friends José, David, and Rye, you provided me the necessary outlets to sustain myself through some of the most difficult times in my life and I cannot thank you enough for that.

And last, but by no means the least, I want to thank my loving wife, Taylor. I could not ask for a better partner in our brief time on this earth and there are not enough words in the English language to accurately capture my gratitude for your partnership. You've always been there to value and believe in me — at my highest and lowest points in life. Your warmth and confidence softened my heart when toil and self-criticism turned it to stone. I would not be the person, nor scientist, that I am today if it weren't for you. There is an exciting and uncertain future that lies ahead of us, but I know that no matter what hardship lies ahead of me, each night I can come home, share a delicious meal with you, and conclude that "all is well".

Portions of this dissertation are adapted with permission from the following materials:

Chapter 4:
Hausch, J.; Berges, A. J.; Zeiser, C.; Rammler, T.; Morlok, A.; Bredehöft, J.; Hammer, S.; Pflaum, J.; Bardeen, C. J.; Broch, K. Distinguishing between Triplet-Pair State and Excimer Emission in Singlet Fission Chromophores Using Mixed Thin Films. *The Journal of Physical Chemistry C* **2022**, *126* (15), 6686-6693. DOI: 10.1021/acs.jpcc.1c09297.

Chapter 5:
Berges, A. J.; Bardeen, C. J. Analysis of molecular photomechanical performance using a one-dimensional harmonic model. *Photochemical & Photobiological Sciences* **2022**. DOI: 10.1007/s43630-022-00261-9.

Chapter 6:
Berges, A. J.; Li, W.; Xu, W.; Tong, F.; Al-Kaysi, R. O.; Hayward, R. C.; Bardeen, C. J. Photomechanical Structures Based on Porous Alumina Templates Filled with 9-Methylanthracene Nanowires. *Crystals* **2022**, *12* (6), 808. DOI: 10.3390/cryst12060808

ABSTRACT OF THE DISSERTATION

Facilitating Work With Photons Via Photomechanical Crystals and Multi-Exciton Materials

by

Adam Berges

Doctorate of Philosophy, Graduate Program in Chemistry
University of California, Riverside, September 2022
Dr. Christopher J. Bardeen, Chairperson

Every year, the amount of solar energy reaching the Earth's surface is approximately 3.4×10^{24} J — nearly 10,000 times the global energy demand. Converting the abundance of solar energy into meaningful work remains a modern challenge in global sustainability. This dissertation focuses on materials that convert photons into two types of work: electrical and (photo)mechanical.

Photovoltaics used in solar cells rely on the generation of excitons from incident light and the band of acceptable wavelengths is dependent on the photovoltaic — typically silicon. Photons with energies that are too large or small to be accepted by silicon's bandgap are either wasted as heat or transmitted/reflected entirely. Performance can be improved by converting the energy of these photons downward (singlet-fission) or upward (triplet-triplet annihilation) towards silicon's bandgap. Both singlet-fission (SF) and triplet-triplet annihilation (TTA) are spin-allowed, multi-exciton processes that have been extensively studied for the past 60 years, and yet relatively little is known about the

correlated triplet pair intermediate. To discover whether a charge-transfer (CT) or excimer state is an intermediate in TTA, solutions of pyrene sensitized with tris-(2-phenyl pyridine) iridium (III) are analyzed. Direct formation of excimers by the annihilating pyrene triplets was not observed, suggesting that TTA only forms a single excited pyrene and there is not a CT intermediate. Analogously, solid SF materials such as anthradithiophene and tetracene are blended with [6]-phenacene, whose large bandgap functions as an inert spacer for local exciton generation. Investigation of the red-shifted luminescence following singlet-fission reveals that excimer formation is a parallel pathway to SF, reinforcing the previous discovery that excimers are not formed directly in either SF or TTA.

Photomechanical materials offer the potential to convert the energy of photons into expansion type work through volume changes generated by photoswitching molecules. There is presently no theoretical framework that establishes an upper limit on the efficiency of photomechanical systems in a manner similar to the Shockley-Quiesser limit for silicon photovoltaics. Using a 1-D harmonic oscillator to model a simple photomechanical cycle, this dissertation defines a maximum absorbed photon-to-work efficiency of 55.4%. Although this model neglects non-idealities of real systems, at 1.5 times the Shockley-Quiesser limit photomechanical materials have the potential to deliver a significant amount of work. Additional progress towards realizing this goal with photomechanical actuators is made through the optimization and characterization of porous alumina templates filled with 9-methylanthracene (9MA) nanocrystals. Demonstrating nearly complete conversion of the photoactive material through 9MA's negative photochromism, these templates bend and deform. This motion is tracked using a Michelson interferometer, revealing the type of

actuation in the template. Surface functionalization has a negligible impact on template loading but optimizing the solvent annealing conditions more than doubles the net loading. Reversible, linear actuation via photomechanical materials has yet to be realized, but advances made in this dissertation provide the basis for achieving this goal.

Table of Contents

List of Tables

List of Figures

Chapter 1. Introduction

Photons provided humanity the tools to develop key technologies for information, communication, and energy for several millennia[1]. Beginning nearly 4,000 years ago with the Taosi gnomon[2], early human civilization recognized the utility of sunlight and from it established a standard for time, navigation, and even city planning. South facing homes became an architectural strategy for heating homes during the winter when access to fuel and energy was limited and marked the beginning of the human effort to harness solar energy. With the advent of Euclid's *Optics*[3] in Ancient Greece, implementing glass and lenses allowed one to focus sunlight to generate heat locally on an object. This led to the famous example of the Heliocaminus baths in Hadrian's villa, where photothermal energy was harnessed to heat the baths. As science and civilization progressed, light and photons became an indispensable tool in how we understood the world around us and how we survived environmental challenges through agricultural and technological development. Today, in the midst of the energy crisis, we are faced by the same fundamental human challenge: how do we convert sunlight into meaningful work?

As we continue to face the challenges posed by climate change and attain the 1.5-2 °C annual warming target set by the Paris Agreement[4], a suitable solution for global energy demands is paramount. According to International Energy Agency, 4.18×10^8 terajoules (TJ) of energy were consumed globally in 2019 and is expected to reach 4.52×10^8 TJ by the end of 2022[5]. However, 3.4×10^{12} TJ of solar energy reaches the earth every year with an average density of 170 watts per square meter (W/m^2)[6]. If just 0.014% of this energy could be stored as electrical, chemical, or mechanical potential energy then our global

energy demands could be sufficiently and sustainably met with solar energy alone. With residential solar panels currently at a maximum efficiency of 22.8%[7] one might expect the energy crisis to be already solved, but significant challenges in energy storage and logistics[8] have yet to be remedied. To date, there are 4 major methods for storing the potential energy of light: chemical potential (e.g. food and agriculture), electrical potential (e.g. photovoltaics), heat (e.g. photothermal), and mechanical potential (e.g. photoswitches and photomechanical materials). This work focuses primarily on storing energy as electrical and mechanical potential and presents multiple advances to these methods.

While advances in electrical energy storage and distribution develop, improvements in photovoltaic module efficiency can supplement the immediate energy demand as increased efficiencies drive the cost of solar energy downward. One avenue for improving the efficiency is by using multi-exciton materials, which use processes such as singlet fission (photon down-conversion) and triplet-triplet annihilation (photon upconversion)[9]. These multi-exciton materials offer a method to convert photons whose energy is usually lost as heat into a useful energy range for generating photocurrent to perform electrical work. If considering a Si-based photovoltaic, then the solar response can be increased by 32% and 35% using photon down-conversion and upconversion respectively. In chapter 3, an investigation into the mechanism of triplet-triplet annihilation with fluorescent probes will shed light on the intermediate of this photophysical process. If triplet-triplet annihilation is proceeding through a charge transfer intermediate, then designing molecules and local environments to stabilize the intermediate will positively impact the rate of photon

upconversion, potentially increasing the performance of the multi-exciton materials when they are incorporated into solar cells.

Alternatively, the solar energy could be converted directly into mechanical work without relying on photovoltaic effects. Using photons to drive molecular machines[10], photomechanical materials offer a method to convert light directly into mechanical work. However, significant improvements to work efficiency and scalability must be addressed before this class of materials can supplement any meaningful energy demand or translate to practical devices. Nevertheless, photomechanical materials hold many promising applications in remote actuation and performing macroscopic work[11-13]. Compared to solar cells, which have a maximum theoretical efficiency of 33.7%[14] for Si single junction modules, the maximum efficiency for molecular photomechanical system is still unknown. The construction of a one-dimensional harmonic oscillator model for calculating these limits of work efficiency of photomechanical molecules will be the main focus of chapter 5.

This chapter will introduce key topics and mechanisms for the two overarching topics of this dissertation: the photophysics of photon upconversion and the relationship between mechanochemistry and organic photomechanical materials.

1.1 Photophysical Topics and Mechanisms

Both topics of this work explore a combination of basic and advanced photophysical processes as the relevant systems are studied. In this section, excitons, relaxation dynamics, excimers, spin-orbit coupling, energy transfer, sensitization, photon down-conversion, and photon upconversion will be discussed in general detail. Experimental methods and

specifications are addressed in chapter 2 and further conceptual details are included in the corresponding chapters of the work.

1.1.1 Excitons

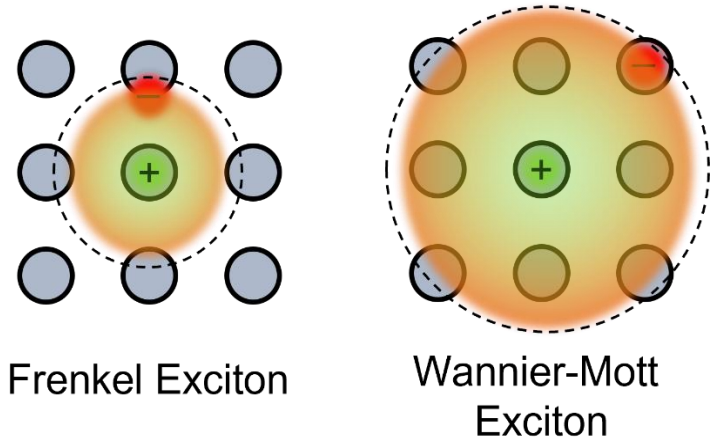

Figure 1.1 Cartoon representations of the Frenkel and Wannier-Mott Exciton in an arbitrary solid.

When an electron receives sufficient stimulus in a solid crystal, it is excited into a higher unoccupied orbital, leaving behind a hole. This excited electron still feels the Coulombic attraction to the positively charged hole that it has left behind but is repelled by the electrons surrounding it. Due to this repulsion, the electron does not immediately recombine with its hole and can instead defuse to nearby atoms in a manner that does not exchange any net charge. The delocalization of this excited electron-hole pair behaves similarly to sound waves that carry heat and motion throughout a crystal lattice. Thus the quanta of this delocalized excitation is dubbed an exciton[15].

The exciton has two distinct flavors based on the strength of the Coulombic attraction between the electron and the hole. In a low dielectric environment, there is less overall screening of the Coulombic forces between the electron and hole, resulting in a stronger

overall attraction. This binds the exciton tightly, limiting the separation of the electron-hole pair to distances typically on the same order of the unit cell when in a crystal, or within the same molecule for a molecular system. As a result, the effective radius of the exciton is small. This flavor is known as the Frenkel exciton (**Figure 1.1**, left)[15] and is the common exciton in molecular solids and solutions. When in an environment with large dielectric screening, the Coulombic interaction is weak, and the exciton has more freedom to diffuse throughout the material. This results in an exciton with a large effective radius, called the Wannier-Mott exciton (**Figure 1.1**, right) [16], which is common in inorganic semiconductors. The generation of excitons and their eventual recombination are of fundamental significance to fluorescence, photophysics, and photocurrent generation.

1.1.2 Excimers

First used to described excitons generated in gaseous singlet excited states[17], excited dimers (excimers) described the delocalization of an exciton across two adjacent atoms or molecules. In a molecular system, the diffusion of this exciton across the two molecules creates a stabilizing association of the molecules that shifts the excited state downward in energy relative to the original monomeric exciton. When the excimer relaxes (radiatively or non-radiatively), it becomes dissociative and returns to the singlet ground state pair if not sterically hindered[17]. Excimers are not isolated to the vapor phase and commonly dominate the fluorescent spectra of concentrated solutions or solid crystals of polyaromatic hydrocarbons such as anthracene and pyrene. The formation of these excimers involves a strong dipole-dipole coupling and/or mixing with a charge-transfer state to enable to the delocalization of the exciton across the two adjacent molecules. As a consequence, they

require short intermolecular distances, on the order of 3-5 Å in pyrene[18]. In the solid, pyrene maximizes its π-π interactions between adjacent molecules, adopting the slip-stack crystal packing. This promotes rapid excimer formation in the solid state and can lead to a fluorescence spectrum that is entirely excimer in a pure single crystal[19]. The kinetics of these excimers indicate that their formation is a diffusion limited process in solution but can outcompete the singlet radiative lifetime by several orders of magnitude. This makes excimer formation a useful tool for determining the distance between monomer constituents, as the excimer intensity is proportional to the local concentration of the monomer.

In chapter 3, pyrene's excimer formation will play a pivotal role in understanding the intermediate of triplet-triplet annihilation in the solution and in chapter 4 will be considered a competing pathway for the investigated singlet-fission materials. Both the monomer and the excimer excitons have several available pathways for relaxation, which will be discussed in the next section.

1.1.3 The Jablonksi Diagram

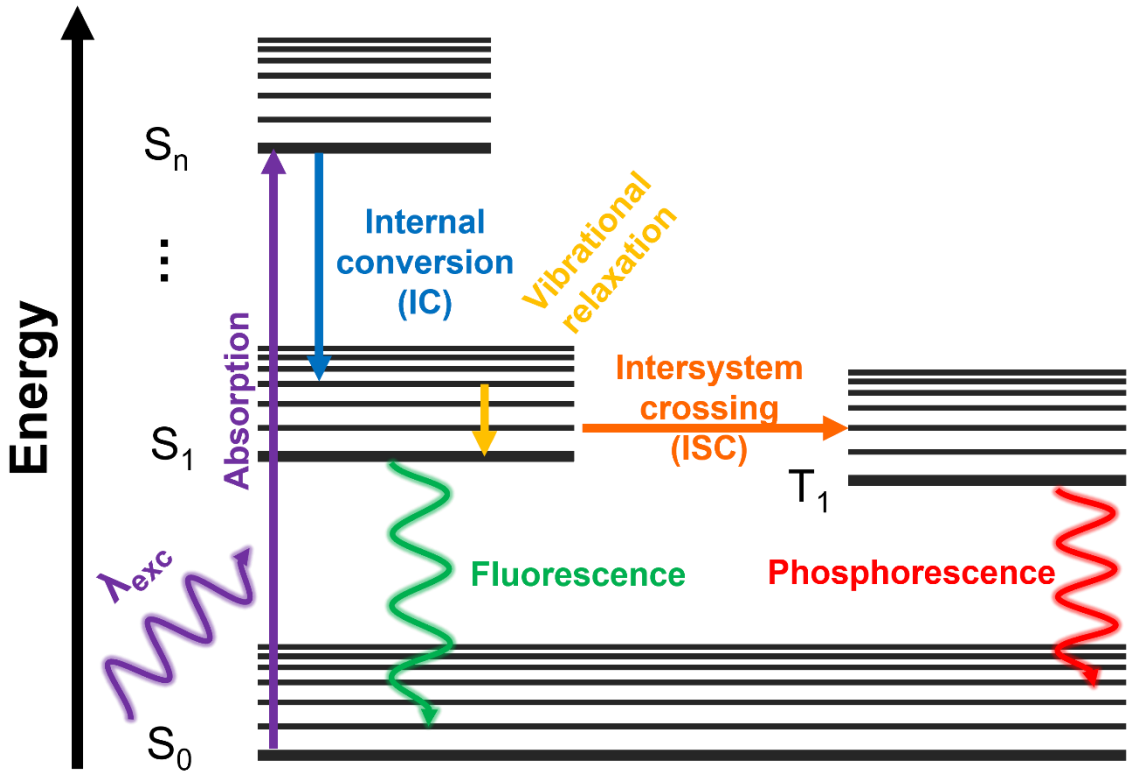

Figure 1.2 Jablonski Diagram for a typical photophysical system. Radiative (fluorescence and phosphorescence) and nonradiative (internal conversion, intersystem crossing) relaxation processes compete after the exciton (bound electron-hole pair) is generated.

The photophysics of organic molecules can be described by the simplified Jablonski diagram pictured above in **Figure 1.2**[20]. After the absorption of an incident photon with wavelength λ_{exc}, an electron is rapidly (1-10 fs) promoted from the highest occupied molecular orbital (HOMO) into some higher energy, unoccupied molecular orbital. For a typical organic molecule, the electron configuration of the HOMO is in the singlet state, hereafter referred to as S_0. Obeying the conservation of spin, the electron that is promoted is excited into some higher lying molecular orbital in a singlet excited state S_n. The electron

then rapidly undergoes internal conversion (IC), relaxing in accordance with the Franck-Condon principle[21, 22] on the 10 fs – 10 ps timescale and relaxes down to a lower lying electronic excited state. Within this excited state, the electron can vibrationally relax on an equally fast 10 fs – 10 ps time scale. The electron typically relaxes non-radiatively until it reaches the lowest lying electric excited state (i.e. the lowest unoccupied molecular orbital, LUMO), where it can then emit a photon and relax radiatively (fluorescence, usually 1 ps – 100 ns). Otherwise, it can continue to relax non-radiatively through IC by continuing to follow the Franck-Condon principle. If there is sufficient overlap in the triplet and singlet excited state vibrational energy levels, the electron can intersystem cross (ISC) and change its spin. This typically occurs on the 10 ns – 1 ms time scale and is outcompeted by other non-radiative and radiative relaxation pathways. The electron now in the triplet excited state can also vibrationally relax down to its lowest excited state before it relaxes non-radiatively through another intersystem crossing or emitting a photon (phosphorescence, 100 μs – 100 ms).

The atom or molecule in the excited state can also relax via collisional quenching[23]. Since this relaxation is dependent on collisions with nearby molecules, the excited atom or molecule can be quenched by either the same species or the solvent when within solution. This rapid relaxation can out compete fluorescence but can be attenuated by reducing collisions by either cooling down the solution or increasing the viscosity of the solvent.

1.1.4 Spin-Orbit Coupling and the Heavy Atom Effect

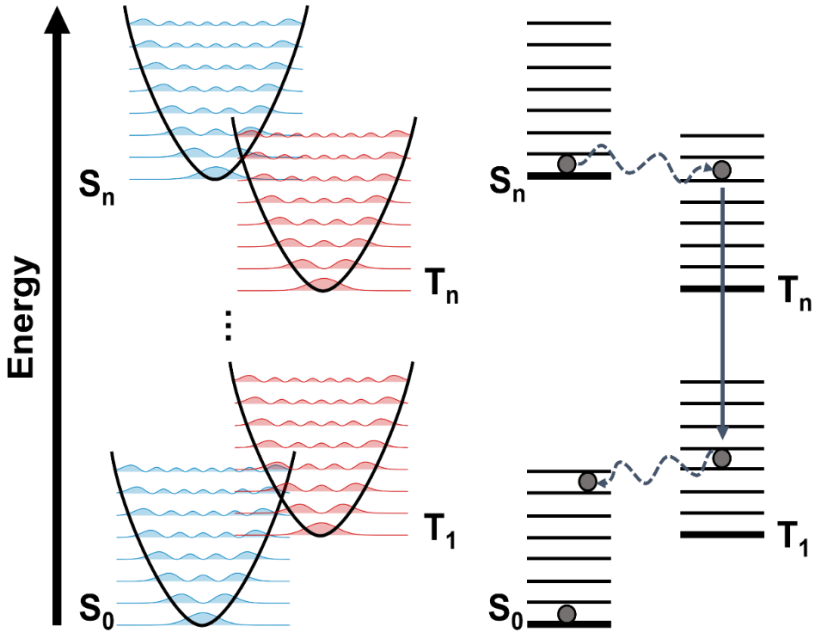

Figure 1.3 A qualitative representation and Jablonski diagram depicting the vibrational wavefunction overlap between the singlet (S_n) and triplet (T_n) excited states. Intersystem crossing (dashed) occurs when the excited electron enters the triplet (or singlet) manifold through this overlap. Afterwards, typical relaxation processes (solid) take place.

Since intersystem crossing is a spin-forbidden process that relies on the overlap of vibrational levels in the singlet and triplet manifolds, it is often thought to be a minor occurrence unless the electron has a significantly large spin-orbit coupling (SOC) term. This coupling of the spin and angular momentum of the electrons allows the spin to change direction under a sufficiently strong electric field generated by the nucleus of the atom and scales quartically with nuclear charge for a heavy atom[24]. Thus, larger nuclei exhibit stronger SOC and experience faster rates of ISC and larger quantum yields for triplet generation. A key component of triplet-sensitization relies on exploiting molecules with large SOC to efficiently generate triplets to inject into acceptor. The figure above describes the typical ISC mechanism for an atom or molecule where SOC has enabled significant

overlap of the vibrational energy levels (**Figure 1.3**, left) of the singlet and triplet manifold, resulting in ISC.

1.1.5 Triplet Sensitization and Energy Transfer

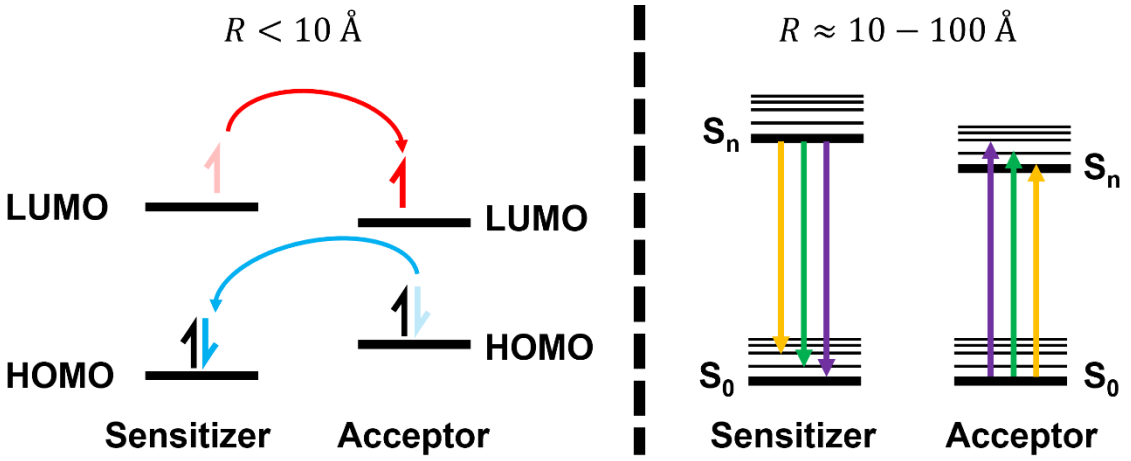

Figure 1.4 Schematic representation for Dexter energy transfer (DET, left) and Förster resonance energy transfer (FRET, right) mechanisms. Since the electrons must be exchanged in the former case, coupling to a charge transfer state and small intermolecular distances (R) must occur. Although FRET can occur at longer distances, its rate is proportional to R^{-6} and provides spatial information when applied for fluorescent labelling.
.

Since the $S_0 \rightarrow T_1$ transition is formally forbidden, its oscillator strength is essentially zero for organic molecules that lack heavy nuclei (e.g. S, Cl, Br, etc.) preventing direct promotion to the triplet state and decreasing the probability of wavefunction overlap and consequentially ISC. For molecules with large SOC terms, the oscillator strength for this transition increases and thus so do rates for ISC. To generate a sufficient triplet population in an ordinary organic molecule suitable for applications in photon upconversion a triplet sensitizer is often necessary[24-27]. Metal-organic triplet sensitizers take advantage of both the heavy atom effect as well as the El-Sayed[28] rule to generate a large SOC and a quickly populated triplet manifold. Triplet sensitization can proceed if the triplet energy of the donor is equal to or greater than the acceptor. The triplet population in the sensitizer can

then be injected into the emitting molecule (acceptor) through a Dexter-type energy transfer mechanism.

Unlike Förster resonance energy transfer (FRET) which occurs via dipole-dipole coupling for spin-allowed transitions[29], Dexter[30] energy transfer (DET) requires significant wavefunction overlap and thus very small (≈ 1 nm) intermolecular distances between the sensitizer and emitter. This allows the triplet sensitizer to inject an electron into the LUMO of the acceptor, which then returns an electron to the HOMO of the sensitizer (**Figure 1.4**, left). The rate of this energy transfer mechanism is proportional to $J \times \frac{K^2}{h} \times e^{-\frac{2R}{L}}$ where J is the spectral overlap integral, L is the sum of the Van der Waals radii, h is Planck's constant, K is an empirical constant in units of energy, and R is the intermolecular distance of the donor and acceptor molecule[31]. For an identical system capable of both mechanisms and a distance of R = 10 nm, the rate of FRET will be roughly 10^3 faster than DET, but is only 10 times faster when R = 1 nm. At a sufficiently high ratio of accepter to donor, the triplet energy of the sensitizer can outcompete other relaxation pathways available to the sensitizer's triplet excited state. For efficient generation of up-converted photons, it is crucial to have a sufficient sensitizer concentration to facilitate the energy transfer without losing too much of the population to parasitic pathways (e.g. phosphorescence, IC, etc.)

Since triplet sensitization uses DET to facilitate the energy transfer, solutions that are too viscous and limit the diffusion of the acceptor and donor molecules can hinder the process. Care should be taken when choosing a solvent for an acceptor/donor system that satisfies the above criteria, as highly viscous solvents may result in a significant amount of

the triplet population lost as phosphorescence as rates of collisional quenching and energy transfer are diminished.

1.1.6 Photon Upconversion and Down-conversion

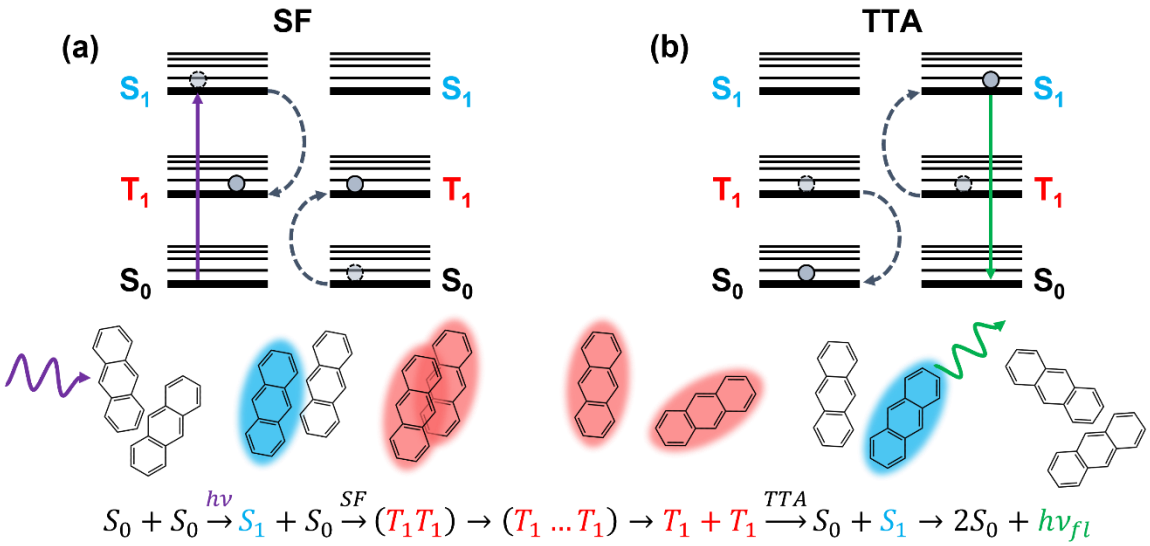

Figure 1.5 Jablonski diagrams for (a) the singlet fission and (b) the triplet-triplet annihilation processes in anthracene. The delayed fluorescence observed in anthracene arises from the generation of the correlated triplet pair resultant from singlet fission. This geminate pair later dissociates, after which these independent triplets can later meet and annihilate, reforming the singlet excited state that later emits a photon ($h\nu_{fl}$).

Previously discussed mechanisms for triplet generation (ISC, sensitization) are for formally spin-forbidden processes but are not an exhaustive list. It is in fact possible to generate triplets from a singlet excited state[32] using a formally spin-allowed process — singlet-fission (SF). Singlet-fission (**Figure 1.5a**), one type of photon down-conversion, is the spin-conserving photophysical process where a singlet excited molecule interacts with a singlet ground state molecule to produce an excited singlet, triplet, or quintet excited state pair in a four-electron system[33]. The production of a coupled triplet pair generates an overall singlet-character of the exciton pair, thereby conserving spin. This allows to SF to produces triplets as fast as 100 fs in the solid state[34]. A molecular system capable of SF can

be either endothermic ($E(S_1) < 2E(T_1)$) or exothermic ($E(S_1) > 2E(T_1)$) and can out-compete other photophysical relaxation processes.

The delayed fluorescence sometimes used to identify singlet fission results from subsequent triplet-triplet annihilation (TTA)[26], otherwise known as photon upconversion (**Figure 1.5b**). Originally studied in polyarene and polyacene systems, sensitized TTA allows the upconversion of an incident photon that generates triplet in the sensitizer to the blue-shifted fluorescent photon generated by the acceptor/annihilator. This mechanism is thought to proceed via a Dexter-type energy transfer through a charge-transfer intermediate as demonstrated below:

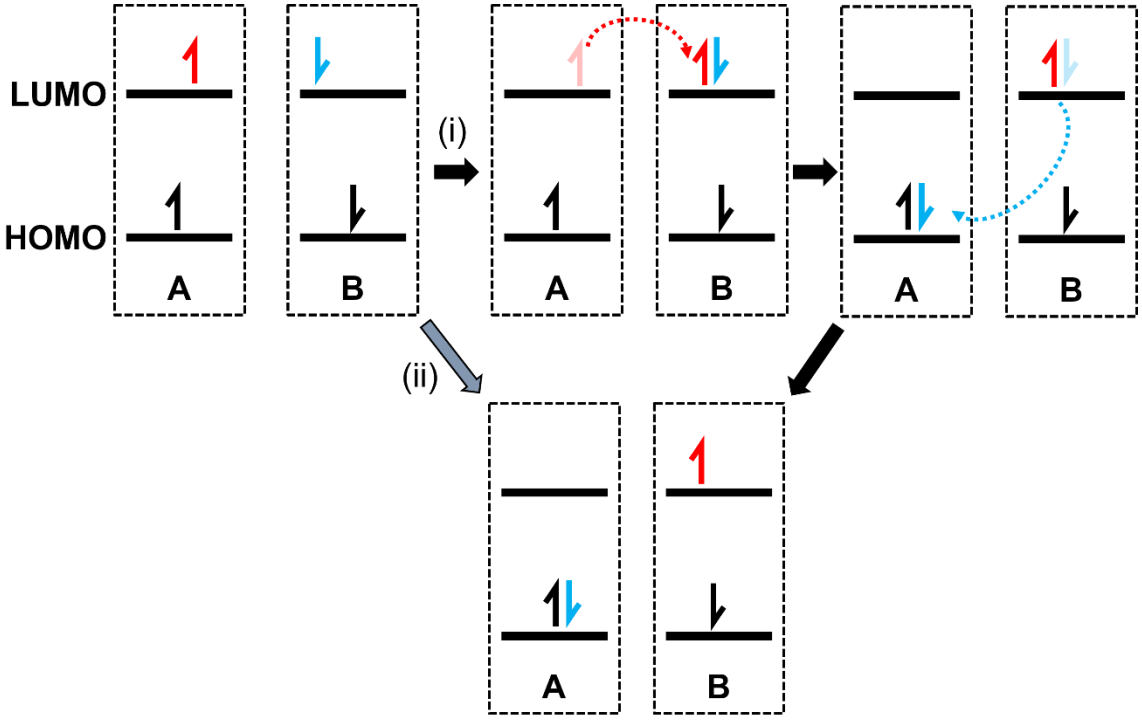

Figure 1.6 A cartoon describing the two different Dexter-type transfer mechanisms thought to occur in triplet-triplet annihilation: (i) one-step electron transfers and (ii) concerted two-step electron transfer.

With the development of metal-centered organic sensitizers with excitonic bands suitable for near-IR and visible excitation[35, 36], TTA was once again popularized due to its

applications in solar cells[9]. Despite its revitalization in research, there is relatively little known about the intermediate of TTA beyond its relationship to charge transfer states[35, 37-39]. Early reports of TTA in solid organic co-crystals indicate that some long-range mechanisms might be enabled by trap states in the crystal[39], and recently, through Förster type energy transfer[40]. To date, there is no consensus on whether TTA occurs exclusively through a charge transfer intermediate or other non-radiative mechanism. Elucidation of this mechanism will provide a basis for designing efficient photon upconversion materials to improve photovoltaic modules, which may significantly reduce the cost for residential and commercial users of solar panels.

1.2 Mechanochemistry and Photomechanical Concepts

Although the roots of mechanochemistry span several centuries[41, 42], its founding is often accredited to Lea's experiments on colloidal silver allotropes[42]. Mechanochemistry explores an alternative thermodynamic route for making and breaking chemical bonds by applying mechanical force. In the absence of direct heating, mechanical stress/strain on a molecule distorts its potential energy surface, decreasing the energy barrier for bond formation/dissociation. This enables a myriad of chemical reactions for preparing catalysts[43, 44], alloying metals[45, 46], and synthesizing organic molecules[47-49]. The converse of this relationship between mechanical work and chemical reactions has been explored extensively in the recent revival of photomechanical research[10, 11, 50-53], but many fundamental questions about its limitations and scalability remain. This section will briefly describe core concepts of mechanochemical and photomechanical models that are explored

in the later chapters on photomechanical work efficiency and inorganic-organic composite actuators.

1.2.1 The Eyring, Zhurkov, and Bell Mechanochemical Models

Beginning with Eyring's model[54] for the flow of viscous fluids, later expanded by Zhurkov's study[55] on crack propagation through a solid, and finally Bell's model[56] of cellular adhesion, a framework for understanding the rate of mechanochemical reactions as a function of activation energy and applied force is established. The Zhurkov-Eyring equation, also known the Boltzmann-Arrhenius-Zhurkov equation (BAZ)[57], relates the mean time to failure τ of a solid to the bond energy E_b, the applied stress σ, the sensitivity constant γ, and the thermal energy kT:

$$\tau = \tau_0 \times \exp\left(\frac{E_b - \gamma\sigma}{kT}\right)$$

(eqn. 1.1)

where τ_0 is the rate of failure when no force or stress is applied.

In his model, Bell gives physical meaning to the sensitivity constant γ, defining it as the displacement in the reaction coordinate (i.e. in the case of cellular adhesion, bond distance) and finds that at the limit of bond cleavage, the activation energy $\Delta E^{\ddagger} \approx 0$, meaning that product of the applied force and reaction coordinate must be equal to the bond energy of the molecule. This establishes the critical force (f_c) per potential bond to be:

$$f_c \sim \frac{kT}{r_0} \ln(KN)$$

(eqn. 1.2)

where r_o is the reaction coordinate, K is the ratio of the forward and reverse rate constants for the bond formation/dissociation, and N is the number of molecules capable of bonding. This model provides a useful framework for estimating the maximum force a bond can sustain before the rate of dissociation dominates bond formation. However, this model originally assumed no other changes occur on the potential energy surface of the system and may fail to capture how mechanical force alters the landscape when higher dimensional forces are applied (i.e. simultaneous torque and linear stress).

1.2.2 Evans-Ritchie Tilted Potential Energy Surface

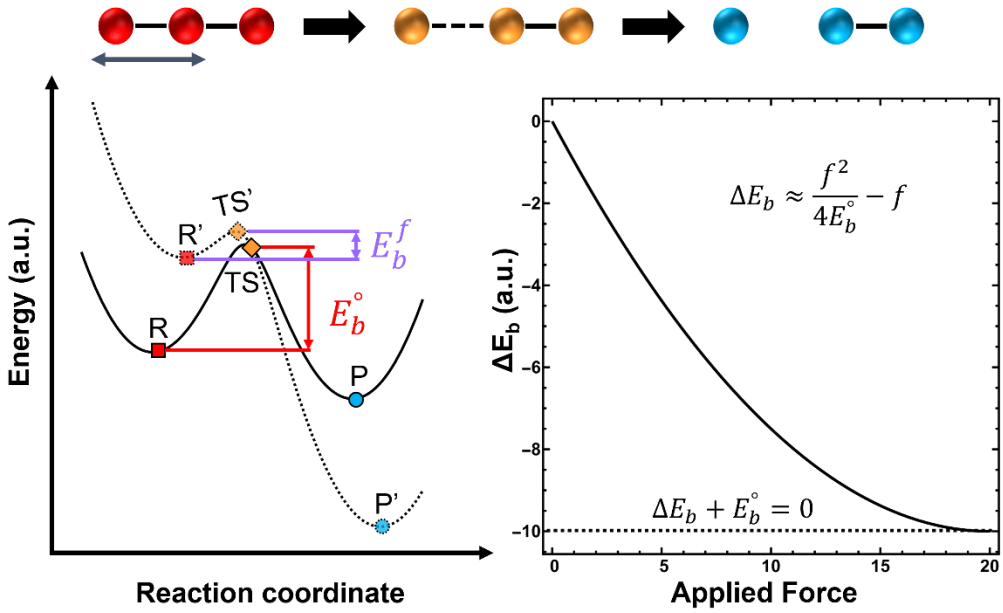

Figure 1.7 Qualitative representation of the Evans-Ritchie tilted potential energy surface model. The simplified potential energy surface (left) for a triatomic molecule is plotted as a function of the reaction coordinate (i.e. bond length). After a force is applied to the molecule, the reactant (R, red) and the transition stage (TS, orange) become similar in energy and geometry. When the bond breaks, the product (P, blue) is formed.

Evans and Ritchie generalized Bell's model for a system whose potential energy surface is altered by the applied mechanical force[58]. In their model, the change in the bond energy ΔE_b is proportional to the applied force (f) and the original bond strength E°_b of the

molecule (**Figure 1.7**). As the applied force alters the potential energy surface, it shifts the reactant and transition state closer together, effectively reducing the activation barrier to some E^f_b. This behavior is described naturally with bond cleavage of a triatomic molecule where the applied force (i.e. stretching of the bond) brings the reactant closer to the transition state until the bond readily breaks with the thermal energy available to the system.

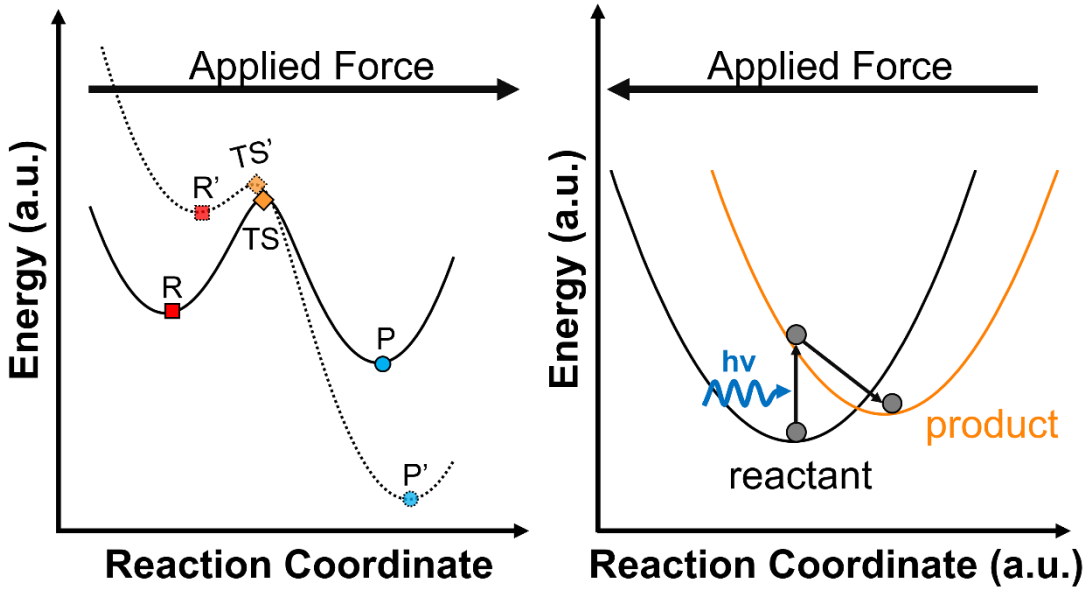

Figure 1.8 Cartoons of potential energy surfaces for mechanochemistry (left) and photomechanical reactions (right). In mechanochemical systems, the applied force is parallel to the reaction direction whereas in photomechanical systems it is antiparallel.

The Evans-Ritchie model can be applied to higher dimensional systems, just as mechanical force can be applied across multiple axes and dihedral angles of a molecule. For photomechanical systems, one is usually interested in the antithesis of this model — how a change in the reaction coordinate produces a mechanical force. Gaub's experiment on azobenzene functionalized oligonucleotides[12] provides a method for directly measuring this work with atomic force microscopy and from this experiment, estimates the maximum

efficiency of work generated by a single azobenzene molecule. Although recent works have shed light on how the mechanical limitations of a photomechanical material relates to its macroscopic efficiency[53], an equivalent model that determines the maximum work efficiency of a single photomechanical molecule has yet to be derived. Chapter 5 seeks to remedy this by proposing a simple one-dimensional harmonic model (**Figure 1.8**) to predict the maximum work efficiency for a photomechanical molecule.

1.2.3 Photoswitches

The key component to a photomechanical material is the generation of a change in length, volume, or crystal packing through the stimulation of a photoswitching molecule. A photoswitch can be any molecule that experiences a structural change when exposed to light and may include photo-induced isomerization, dimerization, cyclization, or dissociation reactions[13, 50-52, 59-63]. Generally, photoswitches can be reversible or irreversible, although the former is typically considered for applications in photomechanical materials. Reversible photoswitches can be separated into two classes based on the stimulus for the back reaction: T-type (thermal) or P-type (photo). Although these molecules perform some structural geometry change, they may not necessarily produce a change in the macroscopic structure of the crystal or composite it is hosted in, with unsubstituted azobenzene being a famous example. Several different photoswitching

molecules are listed in below in the **Figure 1.9** below but are not an exhaustive list of candidates for incorporation into photomechanical materials:

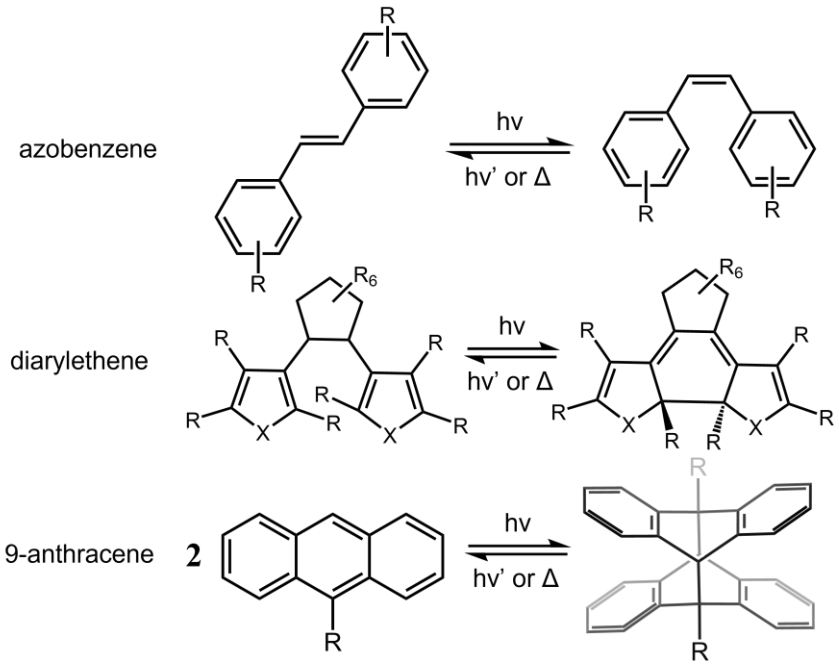

Figure 1.9 Common photoswitches used in photomechanical systems. R denotes any substituent (e.g. alkyl, halide, ester, etc.) and X represents C, N, or S.

Although these photoswitching molecules do not produce a meaningful change in volume or length when in the solution phase, they can generate macroscopic work in the solid phase[63] or when incorporated into polymer or elastomer hosts[62]. Alignment of these photoswitches is crucial to harvesting mechanical work in a pure or composite system but is challenging to control in a scalable way[60]. This work will explore systems that organize organic photoswitching nanocrystals with inorganic and organic composites in chapter 6.

1.2.4 Photochromism

Photoswitches also exhibit photochromism[61, 64], where their absorbance changes during or after the photoreaction takes place. Photochromic molecules are classified as either a positive or negative photochrome depending on whether they increase (**Figure 1.10a**) or decrease (**Figure 1.10b**) their absorbance in the visible spectrum after reacting.

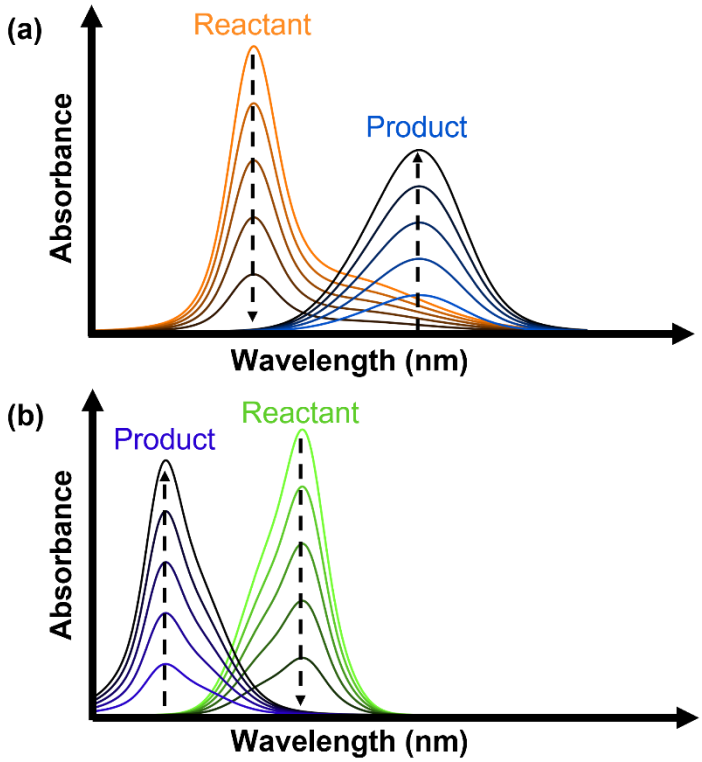

Figure 1.10 Absorbances for two generic photochromic molecules. The positive photochrome (a) will become more colorful as the reaction progresses whereas the negative photochrome (b) becomes colorless.

For solid state applications of photomechanical actuation, negative photochromism is desired as the optical beam penetration will not decrease as the reaction proceeds, allowing an entire crystal or thin film to react completely given a long enough exposure duration. Comparing the penetration depth of a 335 nm excitation source through a 0.1 mM solution of pyrene, trans-azobenzene, and cis-azobenzene demonstrates the drastic difference in

relative intensity of the light source. Using previously reported molar extinction coefficients for pyrene (**Figure 1.11a**) in cyclohexane[65] (ε_{pyrene} = 54,000 M^{-1} cm^{-1}) and azobenzene (**Figure 1.11b**) in methanol[66] (ε_{trans} = 17,383 M^{-1} cm^{-1}, ε_{cis} = 378 M^{-1} cm^{-1}), the relative intensity of the beam can be readily calculated from transmittance using the Beer-Lambert equation.

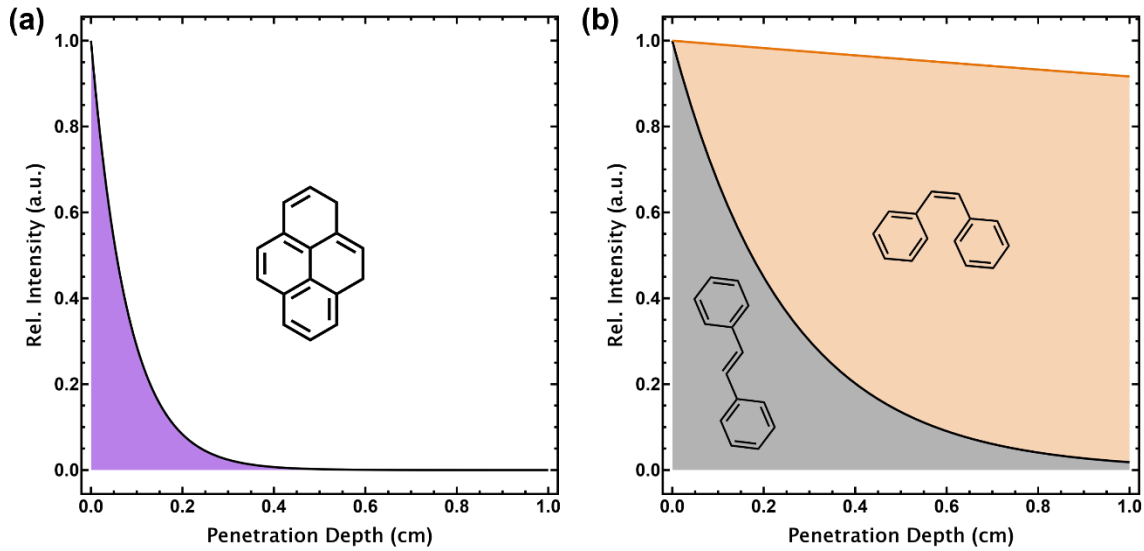

Figure 1.11 Calculated penetration depths of 0.1 mM solutions **(a)** pyrene (purple), **(b)** trans-azobenzene (grey), and cis-azobenzene (orange) using a 335 nm light source using the Beer-Lambert law to calculate the transmittance. Only in cis-azobenzene does light fully penetrate the 1 cm beam path without losing more than 10% of its original power.

1.2.5 Templates and Hosts for Photomechanical Crystals

There are three general strategies for harnessing the mechanical potential of photoswitching molecules: substitution into a polymer (**Figure 1.12a**)[12, 62, 63], growing mesoscale single crystals (**Figure 1.12b**)[52, 59], or templated nanocrystal hosting (**Figure 1.12c**)[11, 60].

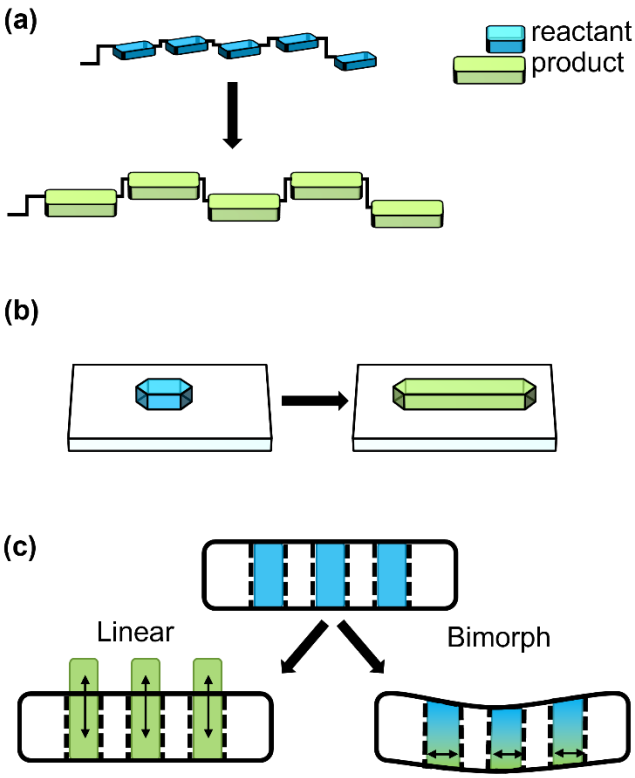

Figure 1.12 A cartoon depicting the three design strategies for hosting photomechanical molecules and their methods of actuation after exposure to light **(a)** substitution of polymer backbone, **(b)** single crystals, **(c)** templated crystal growth.

Each method has their strengths and weaknesses for realizing photomechanical potential in a practical setting. Directly substituting photoswitching molecules into polymer backbones or liquid crystal elastomers provides a bottom-up approach to building photoresponsive materials that is conducive to scalability but suffers from a weak Young's modulus due to the polymer host. Meso- and micro-scale crystals, however, provide a much larger Young's modulus to withstand larger loads but tend to fracture from internal stress caused by the photoreaction leading to irreversible damage of the crystal[67]. Templated nanocrystal hosting minimizes the internal stress and prevents fracturing that

occur with larger crystals but is limited by poor control of the crystal orientation during growth and the impedance matching of the template and active material[11, 68].

1.3 Preview of Research Projects

This work aims to answer three major questions concerning photomechanical materials and multi-exciton photophysics:

1. Does triplet-triplet annihilation proceed through a Dexter-type charge-transfer intermediate, or is a long-range, Förster-type mechanism at play?
2. What is the maximum work efficiency for a molecular photomechanical system?
3. Can templated growth of nanocrystals produce a linear photomechanical actuator?

If the TTA proceeds through a Dexter-type, charge-transfer intermediate, then design of solid-state up-conversion materials for use in photovoltaics will be fundamentally limited as the sub nanometer interaction distance will prevent steric strategies that reduce energy loss to parallel channels[69]. In chapter 3, the charge transfer intermediate and electron exchange mechanism of triplet-triplet annihilation is probed using a triplet-sensitized pyrene solution. Since pyrene's monomer fluorescence changes with the local polar environment and the monomer to excimer fluorescent ratio increases as the intermolecular distance of neighboring pyrene molecules decreases, the fluorescent spectrum of the up-converted solution will provide information on the intermediate of triplet-triplet annihilation. If the triplet population in pyrene is generated solely through sensitization, then any subsequent fluorescence from pyrene occurs directly after the annihilation event. From this experiment, we conclude that the intermediate of TTA occurs at an interaction distance and orientation that is incompatible for direct excimer formation.

This means that the functionalization of annihilating molecules to inhibit excimer formation should not have a negative impact on the TTA mechanism in the solution phase. It also indicates that it may be possible to develop solid state TTA systems with molecular spacers that prevent excimer formation but allow photon upconversion.

An analogue of this type of system is explored in chapter 4 for heterogenous singlet-fission films of anthradithiophene (ADT), tetracene (TET), and [6]-phenacene (6PH). Due to the ≈ 1 eV difference in band gap, 6PH acts as an inert spacer and the photoluminescence of ADT:6PH films provide insight into the role of excimer formation in the singlet-fission process. The red-shifted luminescence observed in these films has a large dependency on local polar environment, suggesting a large charge-transfer admixture and thus an excimer character. This allows us to conclude that the excimer is formed in parallel to singlet-fission and that the red-shifted luminescence is not due radiative relaxation of the correlated triplet pair. The ADT:TET films also serve as a prototypical example of solid state heterofission films, where a singlet exciton can undergo spontaneous fission into two triplets on chemically distinct molecules (e.g. ^{3}ADT and ^{3}TET). Despite the similarities in their band gap energies, no conclusive evidence of singlet heterofission is observed in these blends.

For photomechanical materials, there is presently no model to predict the maximum efficiency of photomechanical, molecular systems. If the maximum theoretical efficiency exceeds the Shockley-Quiesser limit, then photomechanical materials may be the best approach for harnessing solar energy. If, on the other hand, 1% is the most one could hope for, then contemporary research on photomechanical materials is a wasted effort. In chapter 5, this work develops a 1-dimensional model harmonic model for determining the

work efficiency limits in a molecular system. Although it is a simplified model that does not consider the coupling to higher lying excited states, it provides a framework to analyze the performance of a photomechanical molecule and how the force of a load affects the photochemistry by building off the approach of the Evans-Ritchie potential energy surface model. From this model, we determine the maximum theoretical work efficiency to be 55.4 % for an ideal system — over 1.5x the Shockley-Quiesser limit for Si-based solar cells. Applications to a real system will require significant improvements to the model, but it establishes a basis for predicting the behavior of photomechanical molecules and justifies the pursuit of photomechanical research.

Chapter 6 develops a photomechanical actuator using 9-methylanthracene nanocrystals formed in a porous anodized aluminum oxide (AAO). Nanorods of this negative photochromic crystal extracted from the membranes in aqueous solution demonstrate a ≈ 7% expansion along the long axis of the nanorod, suggesting that it is capable of linear actuation when incorporated into the AAO. However, linear actuation as depicted in **Figure 1.12c** isn't observed, but the photomechanical actuation of the template is quantified using Michelson interferometry. The solvent annealing process for embedding these organic photomechanical crystals into porous media is improved and the influence of surface functionalization is determined to be negligible.

The remaining section, chapter 7, will explore unpublished materials and alternative designs for photoswitching molecules using embedded viscous polymer microfibers and amorphous diarylethene microfibers. Microcrystals and nanorods of 4-fluoro-9-anthracenecarboxylic acid are suspended in polyethene oxide (M_w = 8,000,000 g/mol) and

aligned through hand-pulling of the viscous media for the polymer approach and demonstrate a potential bottom-up method for producing photomechanical fibers but face several challenges that inhibit photoactuation. Lastly, molecular microfibers on the 10-100 μm diameter scale are pulled directly from molten diarylethene derivatives and have a potential use in photoswitching fiber optics.

1.4 References

(1) Perlin, J. *Let it shine : the 6,000-year story of solar energy*; New World Library, 2013.

(2) Li, G. Gnomons in Ancient China. In *Handbook of Archaeoastronomy and Ethnoastronomy*, Ruggles, C. L. N. Ed.; Springer New York, 2015; pp 2095-2104.

(3) Euclid; Burton, H. E. *The Optics of Euclid*; Optical Society of America, 1945.

(4) Great Britain, F.; Commonwealth, O. *Paris Agreement : Paris, 12 December 2015*; Foreign and Commonwealth Office
TSO, distributor, 2017.

(5) International Energy, A. *World Energy Outlook 2021*; OECD Publishing, 2021.

(6) Breeze, P. Chapter 13 - Solar Power. In *Power Generation Technologies (Third Edition)*, Breeze, P. Ed.; Newnes, 2019; pp 293-321.

(7) Power, S. *Complete review of SunPower solar panels: Are they really the best?* 2022. https://www.solarreviews.com/blog/are-sunpower-solar-panels-the-best (accessed 06/14/2022).

(8) Kousksou, T.; Bruel, P.; Jamil, A.; El Rhafiki, T.; Zeraouli, Y. Energy storage: Applications and challenges. *Solar Energy Materials and Solar Cells* **2014**, *120*, 59-80. DOI: https://doi.org/10.1016/j.solmat.2013.08.015.

(9) Richards, B. S. Enhancing the performance of silicon solar cells via the application of passive luminescence conversion layers. *Solar Energy Materials and Solar Cells* **2006**, *90* (15), 2329-2337. DOI: https://doi.org/10.1016/j.solmat.2006.03.035.

(10) Browne, W. R.; Feringa, B. L. Making molecular machines work. *Nature Nanotechnology* **2006**, *1* (1), 25-35. DOI: 10.1038/nnano.2006.45.

(11) Dong, X.; Guo, T.; Kitagawa, D.; Kobatake, S.; Palffy-Muhoray, P.; Bardeen, C. J. Effects of Template and Molecular Nanostructure on the Performance of Organic–Inorganic Photomechanical Actuator Membranes. *Advanced Functional Materials* **2020**, *30* (2), 1902396. DOI: https://doi.org/10.1002/adfm.201902396.

(12) Hugel, T.; Holland, N. B.; Cattani, A.; Moroder, L.; Seitz, M.; Gaub, H. E. Single-molecule optomechanical cycle. *Science* **2002**, *296* (5570), 1103-1106. DOI: DOI 10.1126/science.1069856.

(13) Kuzyk, M. G.; Dawson, N. J. Photomechanical materials and applications: a tutorial. *Adv. Opt. Photon.* **2020**, *12* (4), 847-1011. DOI: 10.1364/AOP.387366.

(14) Shockley, W.; Queisser, H. J. Detailed Balance Limit of Efficiency of p-n Junction Solar Cells. *Journal of Applied Physics* **1961**, *32* (3), 510-519. DOI: 10.1063/1.1736034.

(15) Frenkel, J. On the Transformation of light into Heat in Solids. I. *Physical Review* **1931**, *37* (1), 17-44. DOI: 10.1103/PhysRev.37.17.

(16) Wannier, G. H. The Structure of Electronic Excitation Levels in Insulating Crystals. *Physical Review* **1937**, *52* (3), 191-197. DOI: 10.1103/PhysRev.52.191.

(17) Birks, J. B. Excimers. *Reports on Progress in Physics* **1975**, *38* (8), 903-974. DOI: 10.1088/0034-4885/38/8/001.

(18) Bains, G. K.; Kim, S. H.; Sorin, E. J.; Narayanaswami, V. The Extent of Pyrene Excimer Fluorescence Emission Is a Reflector of Distance and Flexibility: Analysis of the Segment Linking the LDL Receptor-Binding and Tetramerization Domains of Apolipoprotein E3. *Biochemistry* **2012**, *51* (31), 6207-6219. DOI: 10.1021/bi3005285.

(19) Birks, J. B.; Kazzaz, A. A.; Edwards, S. F. Excimer fluorescence XII. The pyrene crystal excimer interaction potential. *Proceedings of the Royal Society of London. Series A. Mathematical and Physical Sciences* **1968**, *304* (1478), 291-301. DOI: doi:10.1098/rspa.1968.0087.

(20) Jaffe, H. H.; Miller, A. L. The fates of electronic excitation energy. *Journal of Chemical Education* **1966**, *43* (9), 469. DOI: 10.1021/ed043p469.

(21) Condon, E. A Theory of Intensity Distribution in Band Systems. *Physical Review* **1926**, *28* (6), 1182-1201. DOI: 10.1103/PhysRev.28.1182.

(22) Franck, J.; Dymond, E. G. Elementary processes of photochemical reactions. *T Faraday Soc* **1926**, *21* (February), 536-542, 10.1039/TF9262100536. DOI: 10.1039/TF9262100536.

(23) Daintith, J. *A dictionary of chemistry*; Oxford University Press, 2008.

(24) Dirac, P. A. M.; Fowler, R. H. The quantum theory of the electron. *Proceedings of the Royal Society of London. Series A, Containing Papers of a Mathematical and Physical Character* **1928**, *117* (778), 610-624. DOI: doi:10.1098/rspa.1928.0023.

(25) Marian, C. M. Spin–orbit coupling and intersystem crossing in molecules. *WIREs Computational Molecular Science* **2012**, *2* (2), 187-203. DOI: https://doi.org/10.1002/wcms.83.

(26) Parker, C. A.; Bowen, E. J. Sensitized P-type delayed fluorescence. *Proceedings of the Royal Society of London. Series A. Mathematical and Physical Sciences* **1963**, *276* (1364), 125-135. DOI: doi:10.1098/rspa.1963.0197.

(27) Parker, C. A.; Joyce, T. A. Determination of Triplet Formation Efficiencies by Measurement of Sensitized Delayed Fluorescence. *T Faraday Soc* **1966**, *62* (526p), 2785-&. DOI: DOI 10.1039/tf9666202785.

(28) El-Sayed, M. A. Spin—Orbit Coupling and the Radiationless Processes in Nitrogen Heterocyclics. *The Journal of Chemical Physics* **1963**, *38* (12), 2834-2838. DOI: 10.1063/1.1733610.

(29) Förster, T. Transfer Mechanisms of Electronic Excitation Energy. *Radiation Research Supplement* **1960**, *2*, 326-339. DOI: 10.2307/3583604 (acccessed 2022/06/15/).JSTOR.

(30) Dexter, D. L. A Theory of Sensitized Luminescence in Solids. *The Journal of Chemical Physics* **1953**, *21* (5), 836-850. DOI: 10.1063/1.1699044.

(31) Murphy, C. B.; Zhang, Y.; Troxler, T.; Ferry, V.; Martin, J. J.; Jones, W. E. Probing Förster and Dexter Energy-Transfer Mechanisms in Fluorescent Conjugated Polymer Chemosensors. *The Journal of Physical Chemistry B* **2004**, *108* (5), 1537-1543. DOI: 10.1021/jp0301406.

(32) Singh, S.; Jones, W. J.; Siebrand, W.; Stoicheff, B. P.; Schneider, W. G. Laser Generation of Excitons and Fluorescence in Anthracene Crystals. *The Journal of Chemical Physics* **1965**, *42* (1), 330-342. DOI: 10.1063/1.1695695.

(33) Piland, G. B.; Burdett, J. J.; Dillon, R. J.; Bardeen, C. J. Singlet Fission: From Coherences to Kinetics. *J Phys Chem Lett* **2014**, *5* (13), 2312-2319. DOI: 10.1021/jz500676c.

(34) Jundt, C.; Klein, G.; Sipp, B.; Le Moigne, J.; Joucla, M.; Villaeys, A. A. Exciton dynamics in pentacene thin films studied by pump-probe spectroscopy. *Chemical Physics Letters* **1995**, *241* (1), 84-88. DOI: https://doi.org/10.1016/0009-2614(95)00603-2.

(35) Cruz, C. D.; Choi, H. H.; Podzorov, V.; Chronister, E. L.; Bardeen, C. J. Photon Upconversion in Crystalline Rubrene: Resonant Enhancement by an Interband State. *The Journal of Physical Chemistry C* **2018**, *122* (31), 17632-17642. DOI: 10.1021/acs.jpcc.8b02838.

(36) Singh-Rachford, T. N.; Castellano, F. N. Photon upconversion based on sensitized triplet–triplet annihilation. *Coordination Chemistry Reviews* **2010**, *254* (21), 2560-2573. DOI: https://doi.org/10.1016/j.ccr.2010.01.003.

(37) Beimborn, J. C.; Zagorec-Marks, W.; Weber, J. M. Spectroscopy of Resonant Intermediate States for Triplet–Triplet Annihilation Upconversion in Crystalline Rubrene: Radical Ions as Sensitizers. *The Journal of Physical Chemistry Letters* **2020**, *11* (17), 7212-7217. DOI: 10.1021/acs.jpclett.0c01999.

(38) Minaev, B. F. Theoretical model of triplet-triplet annihilation. *Soviet Physics Journal* **1978**, *21* (9), 1120-1124. DOI: 10.1007/BF00894558.

(39) Sternlicht, H.; Nieman, G. C.; Robinson, G. W. Triplet—Triplet Annihilation and Delayed Fluorescence in Molecular Aggregates. *The Journal of Chemical Physics* **1963**, *38* (6), 1326-1335. DOI: 10.1063/1.1733853.

(40) Staroske, W.; Pfeiffer, M.; Leo, K.; Hoffmann, M. Single-Step Triplet-Triplet Annihilation: An Intrinsic Limit for the High Brightness Efficiency of Phosphorescent Organic Light Emitting Diodes. *Physical Review Letters* **2007**, *98* (19), 197402. DOI: 10.1103/PhysRevLett.98.197402.

(41) Balaz, P.; SpringerLink. *Mechanochemistry in Nanoscience and Minerals Engineering*; Springer Berlin Heidelberg : Imprint: Springer, 2008.

(42) M, C. L. ART. L.--On Allotropic Forms of Silver;: Properties possessed by all the varieties in common and distinguishing them all from normal silver. A. Soluble Allotropic Silver. C. Gold-Yellow and Copper-colored Silver. *American Journal of Science (1880-1910)* **1889**, *37* (222), 476. American Periodicals; Periodicals Index Online.

(43) Hernández, J. G.; Friščić, T. Metal-catalyzed organic reactions using mechanochemistry. *Tetrahedron Letters* **2015**, *56* (29), 4253-4265. DOI: https://doi.org/10.1016/j.tetlet.2015.03.135.

(44) Xu, C.; De, S.; Balu, A. M.; Ojeda, M.; Luque, R. Mechanochemical synthesis of advanced nanomaterials for catalytic applications. *Chemical Communications* **2015**, *51* (31), 6698-6713, 10.1039/C4CC09876E. DOI: 10.1039/C4CC09876E.

(45) Froes, F. H.; Trindade, B. The mechanochemical processing of aerospace metals. *Journal of Materials Science* **2004**, *39* (16), 5019-5022. DOI: 10.1023/B:JMSC.0000039179.07490.39.

(46) McCormick, P. G.; Froes, F. H. The fundamentals of mechanochemical processing. *JOM* **1998**, *50* (11), 61-65. DOI: 10.1007/s11837-998-0290-x.

(47) Andersen, J.; Mack, J. Mechanochemistry and organic synthesis: from mystical to practical. *Green Chemistry* **2018**, *20* (7), 1435-1443, 10.1039/C7GC03797J. DOI: 10.1039/C7GC03797J.

(48) Wang, G.-W. Mechanochemical organic synthesis. *Chemical Society Reviews* **2013**, *42* (18), 7668-7700, 10.1039/C3CS35526H. DOI: 10.1039/C3CS35526H.

(49) Wiggins, K. M.; Brantley, J. N.; Bielawski, C. W. Polymer Mechanochemistry: Force Enabled Transformations. *ACS Macro Letters* **2012**, *1* (5), 623-626. DOI: 10.1021/mz300167y.

(50) Kim, T.; Zhu, L.; Al-Kaysi, R. O.; Bardeen, C. J. Organic Photomechanical Materials. *ChemPhysChem* **2014**, *15* (3), 400-414. DOI: https://doi.org/10.1002/cphc.201300906.

(51) Kondo, M. Photomechanical materials driven by photoisomerization or photodimerization. *Polymer Journal* **2020**, *52* (9), 1027-1034. DOI: 10.1038/s41428-020-0367-0.

(52) Kitagawa, D.; Tsujioka, H.; Tong, F.; Dong, X.; Bardeen, C. J.; Kobatake, S. Control of Photomechanical Crystal Twisting by Illumination Direction. *J Am Chem Soc* **2018**, *140* (12), 4208-4212. DOI: 10.1021/jacs.7b13605.

(53) Zhou, B.; Bernhardt, E.; Bhuyan, A.; Ghorbanishiadeh, Z.; Rasmussen, N.; Lanska, J.; Kuzyk, M. G. Theoretical and experimental studies of photomechanical materials [Invited]. *J. Opt. Soc. Am. B* **2019**, *36* (6), 1492-1517. DOI: 10.1364/JOSAB.36.001492.

(54) Powell, R. E.; Eyring, H. Mechanisms for the relaxation theory of viscosity. *Nature* **1944**, *154*, 427-428. DOI: DOI 10.1038/154427a0.

(55) Zhurkov, S. N.; Tomashevskii, E. E. Microscopic Investigation of Crack Propagation on Rupture. *Sov Phys-Tech Phys* **1957**, *2* (6), 1140-1148.

(56) Bell, G. I. Theoretical-Models for the Specific Adhesion of Cells to Cells or to Surfaces. *Adv Appl Probab* **1980**, *12* (3), 566-567. DOI: Doi 10.1017/S0001867800035254.

(57) Suhir, E. Survivability of species in different habitats: Application of multi-parametric Boltzmann-Arrhenius-Zhurkov equation. *Acta Astronautica* **2020**, *175*, 249-253. DOI: https://doi.org/10.1016/j.actaastro.2020.04.062.

(58) Evans, E.; Ritchie, K. Dynamic strength of molecular adhesion bonds. *Biophys J* **1997**, *72* (4), 1541-1555. DOI: Doi 10.1016/S0006-3495(97)78802-7.

(59) Al-Kaysi, R. O.; Bardeen, C. J. Reversible Photoinduced Shape Changes of Crystalline Organic Nanorods. *Advanced Materials* **2007**, *19* (9), 1276-1280. DOI: https://doi.org/10.1002/adma.200602741.

(60) Dong, X.; Tong, F.; Hanson, K. M.; Al-Kaysi, R. O.; Kitagawa, D.; Kobatake, S.; Bardeen, C. J. Hybrid Organic–Inorganic Photon-Powered Actuators Based on Aligned Diarylethene Nanocrystals. *Chemistry of Materials* **2019**, *31* (3), 1016-1022. DOI: 10.1021/acs.chemmater.8b04568.

(61) Hirshberg, Y.; Fischer, E. Photochromism and reversible multiple internal transitions in some spiropyrans at low temperatures. Part I. *Journal of the Chemical Society (Resumed)* **1954**, (0), 297-303, 10.1039/JR9540000297. DOI: 10.1039/JR9540000297.

(62) Ikeda, T.; Mamiya, J.-i.; Yu, Y. Photomechanics of Liquid-Crystalline Elastomers and Other Polymers. *Angewandte Chemie International Edition* **2007**, *46* (4), 506-528. DOI: https://doi.org/10.1002/anie.200602372.

(63) Russew, M.-M.; Hecht, S. Photoswitches: From Molecules to Materials. *Advanced Materials* **2010**, *22* (31), 3348-3360. DOI: https://doi.org/10.1002/adma.200904102.

(64) Hirshberg, Y.; Bergmann, E.; Bergmann, F. Absorption Spectra and Photo-Isomerization of Arylated Dienes. *J Am Chem Soc* **1950**, *72* (11), 5120-5123. DOI: DOI 10.1021/ja01167a084.

(65) Berlman, I. B. *Handbook of fluorescence spectra of aromatic molecules*; Academic Press, 1971.

(66) Vetráková, L. u.; Ladányi, V.; Al Anshori, J.; Dvořák, P.; Wirz, J.; Heger, D. The absorption spectrum of cis-azobenzene. *Photochemical & Photobiological Sciences* **2017**, *16* (12), 1749-1756. DOI: 10.1039/c7pp00314e.

(67) Medishetty, R.; Sahoo, S. C.; Mulijanto, C. E.; Naumov, P.; Vittal, J. J. Photosalient Behavior of Photoreactive Crystals. *Chemistry of Materials* **2015**, *27* (5), 1821-1829. DOI: 10.1021/acs.chemmater.5b00021.

(68) Guo, T.; Zheng, X.; Palffy-Muhoray, P. Impedance matching in an elastic actuator. *Soft Matter* **2021**, *17* (15), 4191-4194, 10.1039/D1SM00132A. DOI: 10.1039/D1SM00132A.

(69) Zhao, W.; Castellano, F. N. Upconverted Emission from Pyrene and Di-tert-butylpyrene Using Ir(ppy)3 as Triplet Sensitizer. *The Journal of Physical Chemistry A* **2006**, *110* (40), 11440-11445. DOI: 10.1021/jp064261s.

Chapter 2. Experimental Methods

2.1 Sample Preparation

2.1.1 Pyrene and $Ir(ppy)_3$

Pyrene (98% Pure, Sigma Aldrich) is used as received and weighed in an AND HR120 balance and added directly to solvent (tetrahydrofuran, THF, HPLC grade, dichloromethane, DCM, or orthodichlorbenzene, ODCB) without further purification. Solutions are prepared in volumetric flasks (e.g. 25-mL, 10-mL) and serial diluted using glass graduated pipettes. Solid tris(2-phenylpyridine) iridium (III) ($Ir(ppy)_3$, sublimed grade, Sigma Aldrich) is weighed and used as received to prepare a 100-mL stock solution in THF. The series of sensitized solutions are derived from these two stock solutions. Before steady-state and time-resolved fluorescence experiments are performed, solutions are deaerated with Ar for 20 minutes in a screw-cap, 1 cm beam path fused-silica cuvette. Samples are also topped with a balloon of Ar to prevent reintroduced of oxygen through the septa.

2.1.2 Anthradithiophene, [6]-Phenacene, and Tetracene films[1]

Anthradithiophene (ADT, Sigma-Aldrich, 97% purity, the material contains a mixture of two different isomers, anti-ADT and syn-ADT), Tetracene (TET, Sigma-Aldrich, 99.99% purity), and [6]-phenacene (6PH, Lambson Japan Co. Ltd., 99% purity) were used as received. The samples were prepared by codeposition (organic molecular beam deposition) in a high vacuum chamber with a base pressure of 10^{-8} mbar. The molecules were resistively heated in individual Knudsen-cells, and the deposition rate for each molecule was controlled by a separate quartz crystal microbalance (QCM), calibrated using

X-ray reflectivity (XRR) measurements. All films have a nominal thickness of 80 nm and were deposited with a total growth rate of 6 Å/min on native silicon and quartz glass substrates, which were kept at room temperature during growth. The mixing ratio of each film was calculated in molar % of ADT.

2.1.3 9-methylanthracene Nanorod Filled Templates[2]

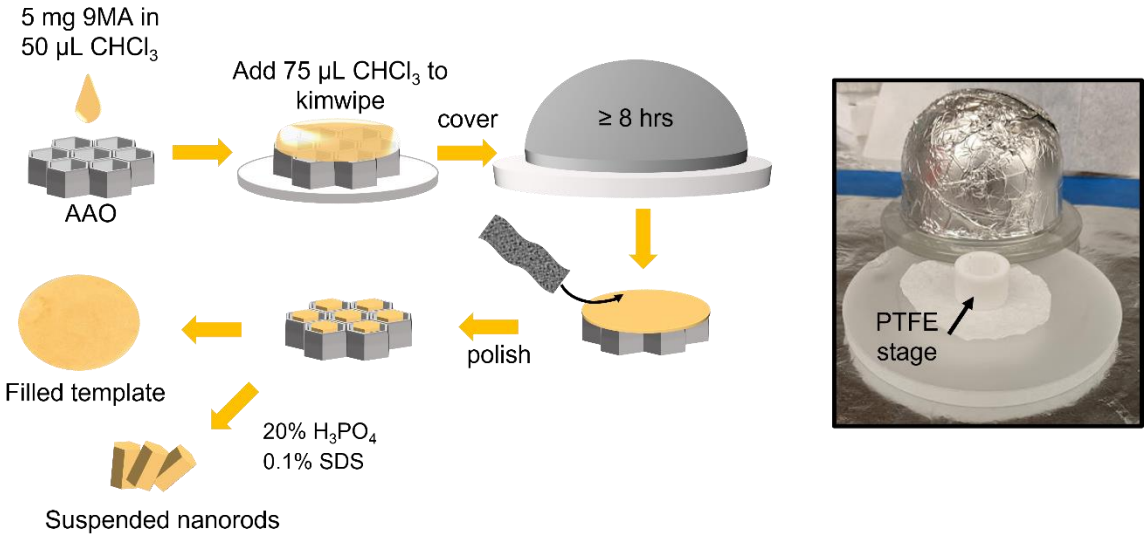

Figure 2.1 Flowchart detailing the new template filling procedure for 9MA in chloroform. Templates are pre-washed in chloroform before solution is added to the surface. Once dry, each sample is polished with 9 µm Al2O3, 5 µm SiC, 2 µm, 1 µm, 0.3 µm Al2O3 lapping paper. Inset: photograph of the apparatus used.

The crystal growth solutions were prepared by adding approximately 5 mg of solid 9-methylanthracene (9MA, 98%, Sigma Aldrich) to a glass vial containing 50 µL $CHCl_3$. The solution was then sealed in the vial and sonicated for 5 min in a room temperature water bath. An empty anodized aluminum oxide (AAO) template (Whatman Anodisc inorganic filter membrane, 13 mm diameter with a 0.2 µm pore diameter purchased) was wetted with $CHCl_3$ before it was placed on the PTFE stage in the solvent annealing apparatus. While the template was still wet, the 9MA solution was quickly added on top of

the template and a measured volume of $CHCl_3$ was added to the Kimwipe which was present below the sample stage. Typically, enough solvent is used to saturate 110% of the volume of the bell jar used (e.g. for a 163 cm^3 bell jar, a total volume of 125 µL was used, corresponding to a ≈ 180 cm^3 container of vapor). Each bell jar is covered with aluminum foil to prevent premature photodimerization by ambient lighting. The solvent was allowed to evaporate at room temperature overnight, after which the template was hand-polished using a series of lapping papers (9 µm Al_2O_3, 5 µm SiC, 2 µm Al_2O_3, 1 µm Al_2O_3, and 0.3 µm Al_2O_3). Each face of the template was polished until it appeared to be shiny and uniform.

2.1.4 Surface Functionalization of AAO Templates[3]

In order to make the AAO surface hydrophobic, a previously developed method to functionalize the surface with carboxylic acids is employed[4]. Lauric acid (≥98% Sigma Aldrich) was dissolved in denatured laboratory-grade ethanol at a concentration of 20 g/L. The solution was added to a 10 mL beaker and heated to 55 °C. Empty AAO templates were placed upright in the beaker, supported by a hollow PTFE cylinder, and the solution was stirred for 30 min. Afterwards, the templates were rinsed separately in Millipore water and fresh ethanol before drying in an oven at 80 °C for 15 min. The same procedure was used for 3-phenylpropionic acid (99% Sigma Aldrich); however, this additional process started with a concentration of 15 g/L in ethanol.

2.1.5 4-Fluoro-9-Anthracene Carboxylic Acid Nanorods

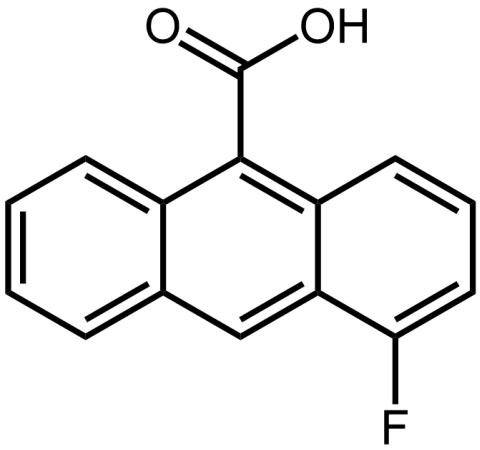

Figure 2.2 Structure of 4F9AC monomer, which undergoes a [4+4] cycloaddition reaction as described in **Figure 1.9**.

Following a similar procedure to 9MA in **2.1.3**, approximately 4 mg of 4-fluoro-9-anthracene (4F9AC, synthesis described elsewhere[5]) powder is weighed in a Sartorius ME-5 microbalance and added directly to a 2-mL vial where it is dissolved in 75 µL N,N dimethylformamide (DMF, dried with $MgSO_4$ and filtered with a Whatman qualitative filter). The AAO template is wetted with DMF and placed on the Teflon stage after which the solution is added directly to the template. The sample is covered with a bell-jar for 48 hrs and the DMF is allowed to dry. Afterwards, the which the template was hand-polished using a series of lapping papers (9 µm Al_2O_3, 5 µm SiC, 2 µm Al_2O_3, 1 µm Al_2O_3, and 0.3 µm Al_2O_3). The AAO is etched away using a 20 % wt. H_3PO_4, 0.1 % wt. sodium dodecyl sulfate (SDS, Sigma Aldrich) aqueous solution. The polished template is added to approximately 5 mL of the etchant solution and heated to 50 °C in the dark for 48-72 hrs.

2.1.6 PEO-8M microfibers

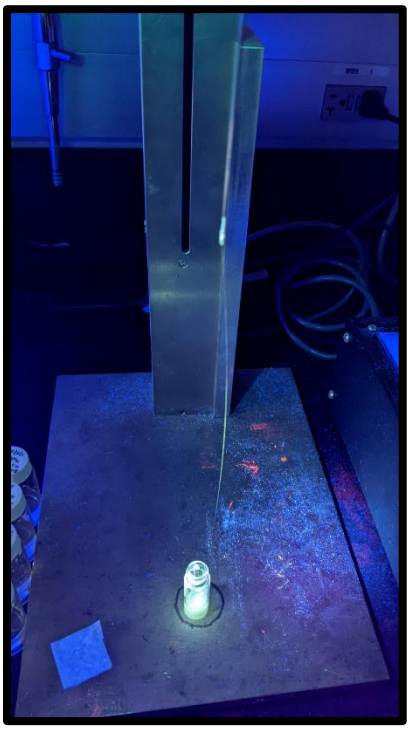

Figure 2.3 Microfiber of PEO-8M doped with 4F9AC nanorods, pulled directly from solution using the draw tower. The apparatus and microfiber are illuminated with a 365 nm flashlight. 4F9AC excimer fluorescence is visible in both the fiber and the solution.

Solid polyethylene-oxide (PEO-8M, M_w = 8,000,000 g/mol, Sigma Aldrich) is weighed in Mettler Toledo AB104-S balance and added directly to Millipore water. Sodium-dodecylsulfate (SDS, Sigma Aldrich) is weighed in a Sartorius ME-5 microbalance and added directly to the aqueous solution. For optimal viscosity[5], a 2 % wt. PEO-8M, 0.2 % wt. SDS, 1.0 g solution is prepared. Solutions are stirred at room temperature with a micro-stir bar at 1000 rpm until the polymer is completely dissolved (24-48 hrs). Microfibers are drawn with a 21 AWG needle pulled directly from the viscous solution. The needle is mounted at the top of the draw tower (see **Figure 2.3**) and the tip is submerged in the PEO-8M solution, and the vial is quickly pulled away and placed at the bottom of the tower. The fiber dries within 5 minutes, after which it is available to be mounted onto substrates.

Nanowires or sublimed microneedles of 4F9AC are added directly to an unmixed 2 % wt. PEO-8M, 0.2 % SDS, pH ≈ 3 ($NaHCO_3$, H_3PO_4) aqueous solution and stirred at 1000 rpm in the dark with a micro-stir bar until the polymer has completely dissolved. The solution must be kept at pH < 5 to prevent the 4F9AC from dissolving in the aqueous solution over time. If pH < 2, the PEO-8M degrades and hydrolyzes over the span of a week and loses its viscosity.

2.1.7 PMMA fibers

Figure 2.4 Fibers of PMMA doped with 4F9AC under illumination of a UV lamp, demonstrating the monomeric blue fluorescence.

Poly(methyl methacrylate) (PMMA, Sigma Aldrich) is weighed in a Mettler Toledo AB104-S balance and added directly to a pre-cleaned 20-mL scintillation vial. Acetone (HPLC grade) is added to the vial until a 50 % wt. solution is achieved. The solution is sonicated for 24-48 hrs until the polymer has completely dissolved. A 21 AWG needle is submerged into the viscous polymer solution and pulled slowly by hand to pull a millimeter scale fiber from the solution. If the solution dries out and solidifies, acetone is reintroduced, and the solution is sonicated until it dissolves again. To dope the fiber, solid 4F9AC is

weighed in a Sartorius ME-5 microbalance and added directly to the PMMA solid before co-dissolving in acetone. This results in the blue monomer fluorescence of doped fibers after UV irradiation and thus no photomechanical behavior.

2.1.8 Diarylethene Microfibers

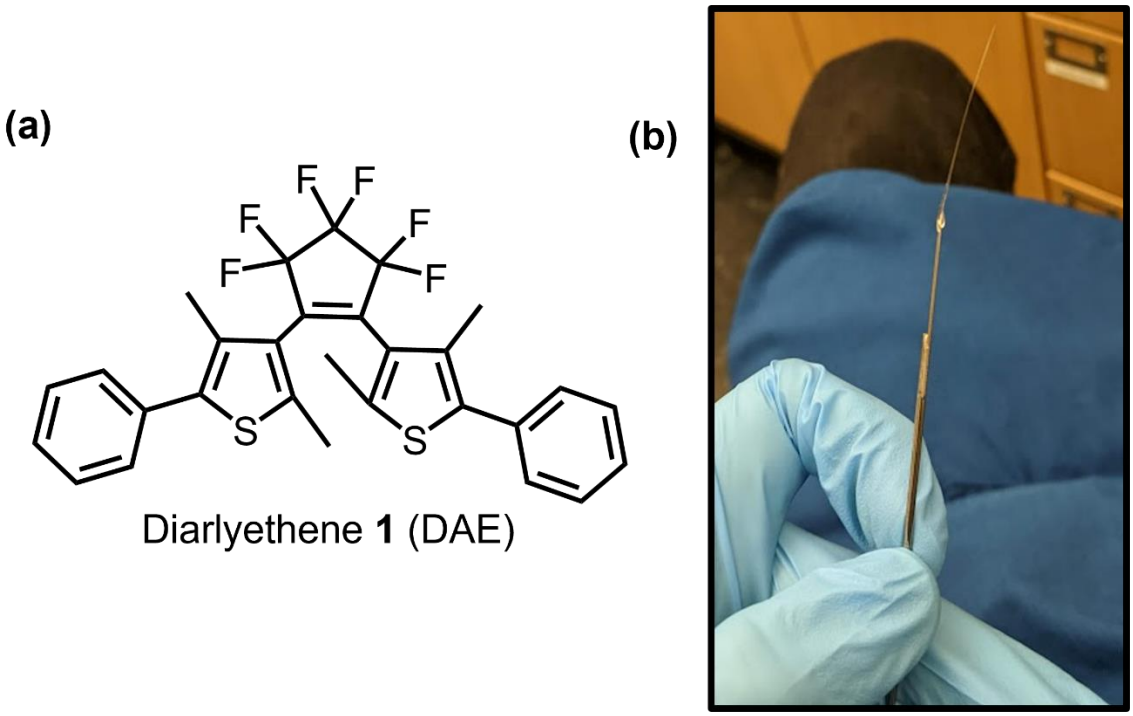

Figure 2.5 (a) Structure of the commercial diarylethene used for microfiber production and (b) an example of a molecular microfiber drawn from the molten liquid.

Commercial diarylethene, 1,2-Bis(2,4-dimethyl-5-phenyl-3-thienyl)-3,3,4,4,5,5-hexafluoro-1-cyclopentene (DAE, >98% Pure, TCI Chemicals B2629) powder is added directly to a 2-mL glass vial for melting. About 20-30 mg is required to form a sufficient volume of molten DAE for pulling fibers. The vial is placed is directly into a silicone oil bath raised to ≈ 138 °C and given approx. 1-2 minutes to fully melt. The vial is then raised and clamped 6 inches above the bath and given a minute to cool. After the minute has

passed, a ≈ 250 μm stainless steel needle is submerged into the molten crystal and pulled slowly by hand at 70-80 s of total cooling. Longer cooling periods result in a more viscous liquid, which is preferrable for pulling larger diameter microfibers but are ultimately shorter as the molten crystal is closer to complete solidification.

2.2 Characterization

2.2.1 Steady-State Absorbance Spectroscopy[1]

Sample solutions are added to a pre-cleaned 1 cm beam path UV grade fused-silica cuvette and measured at room temperature in an Agilent Cary 60 with a 0.5 nm interval and 0.0125 integration time. Solutions with high optical densities are measured in 50 or 200 μm beam paths using a variable beam path cuvette equipped with an insertable quartz column. The 9.95 mm and 9.8 mm lengths of the column's base reduce the beam path through the solution depending on the orientation of the column. Solvent backgrounds are measured and recorded with 50 μm, 200 μm, and 1 cm beam paths when appropriate. Cuvettes are rinsed with the solvent and then in triplicate with a 60:40 by vol. acetone and methanol mixture before being air-dried between samples.

For the ADT, TET, and 6PH blended films, absorption spectra were recorded with a PerkinElmer Lambda 950 UV–vis–NIR spectrometer.

2.2.2 Steady-State Fluorescence Spectroscopy

Samples are first deaerated for 15-20 mins with Ar and sealed with an Ar filled balloon after being added to a 1 cm UV grade fused-silica cuvette. Samples are typically measured at a 90 ° collection angle in a Horiba QM 400 fluorimeter with a 1 nm bandpass at the excitation and emission slits. For samples with large self-absorbance, such as pyrene,

quasi-front face collection is achieved by using a rotational mount to minimize the inner-filter effect.

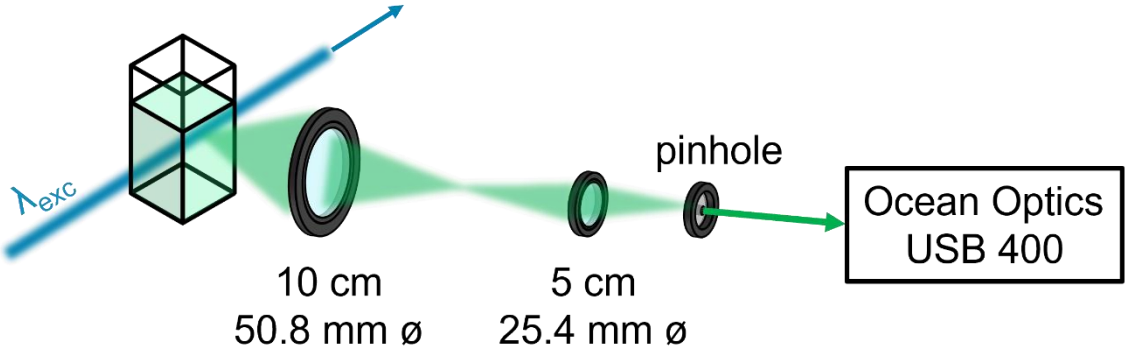

Figure 2.6 Alignment of the sample and spectrometer for the up-converted fluorescent emission experiment. The emission is relay imaged onto the pinhole of the fiber optic coupler.

For the steady-state upconversion experiments, solutions are measured with an Ocean Optics USB 400 spectrometer coupled to an optical fiber. The solution is excited on the edge of the cuvette and collected at a 90 ° collection angle to minimize the inner-filter effect. Spectra are averaged 5 times with 50-100 ms integration times to prevent bleaching of the spectrometer.

For the solid ADT, TET, and 6PH blended films, steady-state photoluminescence measurements were conducted with a pulsed laser diode LDH-P-C-470 (Pico-Quant, Germany) of 470 nm wavelength, a time-averaged power of 0.05 μW, and a repetition rate of 40 MHz. Using a Plan-NEOFLUAR 65x/NA 0.75 air-objective (Carl Zeiss AG, Germany), the laser pulses were focused on a spot with a 30 μm diameter on the sample, yielding a fluence of 1.77 × 10–4 μJ/cm2. As the detecting unit, an Acton SP300 spectrometer with a PIXIS 100 camera (both Princeton Instruments, USA) was used.

2.2.3 Time-Resolved Photoluminescence Spectroscopy[5]

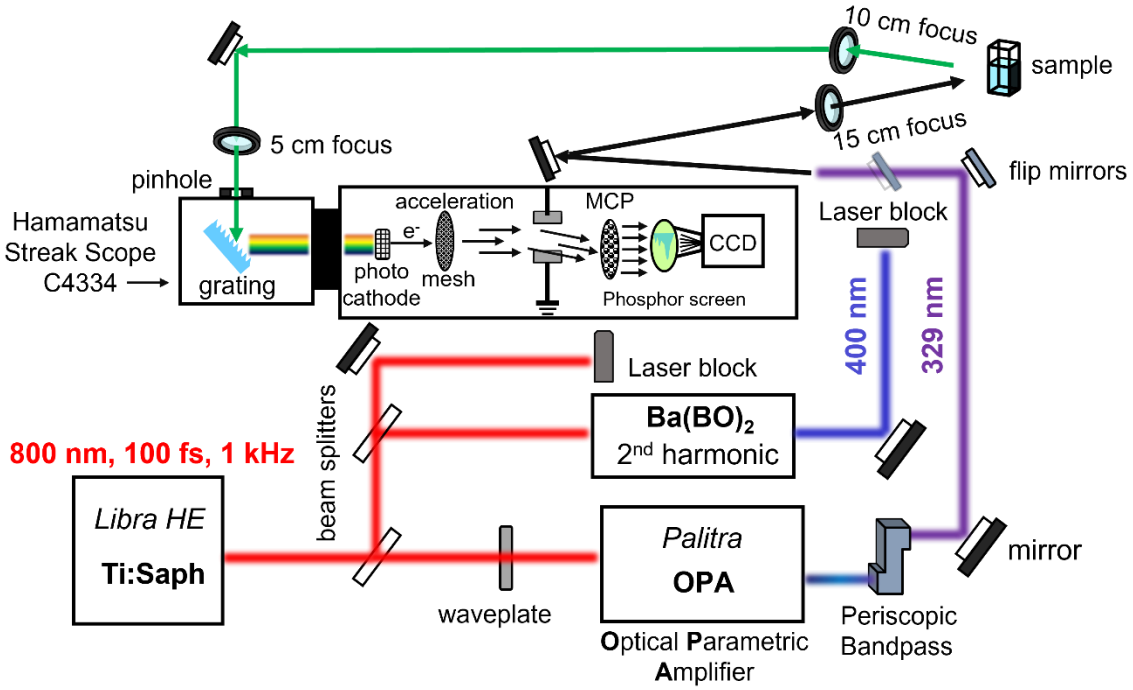

Figure 2.7 Diagram of the experimental set-up used for time-resolved photoluminescence using an excitation wavelength of 329 nm generated using the 800 nm, 1 kHz fundamental beam from the Coherent Libra HE coupled into an optical parametric amplifier.

The Hamamatsu C4334 streak scope has a temporal resolution of ≈ 20 ps and spectral resolution of 2.5 nm. The luminescent emission from the samples is relay images through a pinhole onto a monochromator. The monochromator separates the emission horizontally into separate wavelengths where it then hits a photocathode and generates electrons. These electrons are accelerated with a mesh inside a cathode tube and experience through a time-varying electric field which deflects the electrons vertically, generating temporal resolution. These electrons hit a multi-channel plate (MCP) then finally a phosphor screen. Luminescence from the phosphor screen is captured with a tapered fiber optic bundle coupled to a CCD camera. The pixel position and intensity correspond to the spatial (wavelength, horizontal) and temporal (vertical) information of the experiment.

For samples and solutions measured with the Hamamatsu C4334 Streakscope and Camera the excitation source is either: (i) the Ti:Saph fundamental beam at 800 nm and 1 kHz rep. rate (Coherent Libra HE), (ii) the frequency doubled 400 nm beam at a 1 (from fundamental) or 100 kHz rep. rate (Pockels cell, ConOptics), (iii) a sum-frequency generated beam from the coupled optical parametric amplifier (OPA, Palitra), or (iv) the acousto-optically modulated (Gouch and Housego) 460 nm laser diode at a 1 kHz rep. rate. Solutions are deaerated with Ar for 15-20 mins and sealed with an Ar filled balloon in a 1 cm beam path cuvette and solid samples are mounted to a Janis flow cryo-stat pumped down to 10^{-5} Torr. Streak images are integrated for 10^4-10^5 counts, depending on the brightness of the emission, with the multichannel plate gain set to 16. For the triplet sensitized pyrene solutions in THF, DCM, and ODCB, an average energy of 23.5 nJ was used during the 250 μs pulse. The solid-state ADT, TET, and 6PH blended samples were irradiated with a laser fluence of < 1.2 μJ/cm^2.

2.2.4 Grazing-Incidence Wide Angle X-ray Spectroscopy[1]

For the ADT, TET, and 6PH blended films, the mixing ratio of each film was calculated in molar % of ADT. XRR measurements were performed on a Ge XRD 3003TT instrument, and grazing incidence wide-angle X-ray scattering (GIWAXS) measurements, on a Xeuss 2.0 (Xenocs) in-house instrument with a Pilatus 300k detector, both using Cu Kα radiation (λ = 1.541 Å).

For the 9MA filled AAO templates, GIWAXS experiments were performed using a Ganesha SAXS-LAB (Holyoke) instrument at room temperature. The X-rays (λ = 1.54 Å, Cu Kα radiation) were incident at an angle of 2° to the sample's surface in order to reveal

the crystalline plane distribution with respect to the sample's normal direction. A slice of 9MA-filled AAO template (3 mm × 1 mm) was mounted on a Thorlabs Rotation Stage (ThorLabs, MSR P01). A Pilatus 300K detector was used to collect the 2D diffraction pattern. The sample to detector distance was 86.55 mm. All the GIWAXS raw data from the 9MA filled templates were processed using SAXSGUI software.

2.2.5 Michelson-Interferometry and Beam-Deflection[6]

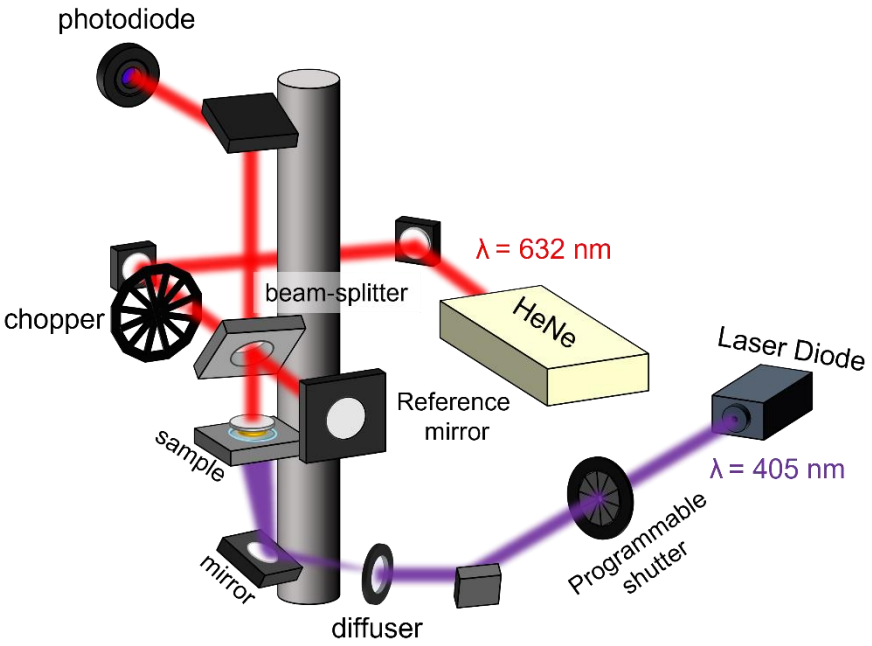

Figure 2.8 Diagram of the Michelson interferometer and beam-deflection experimental set-up. To allow reaction of the template without slippage of the mirror, the sample is irradiated from beneath the stage through the optical flat. The recombined 632 nm beam

Samples of 9MA filled AAO templates are placed on a λ/4 optical flat with a 25 mm diameter mirror placed on top of it. A 632 nm beam from a HeNe laser (SpectraPhysics 155) is chopped at 50 Hz and sent through a 50:50 beam splitter to split the source into the probe and reference path. The optical flat stage, beam splitter, and reference mirror are all adjusted until constructive interference is maximized when the beam paths recombine. The

reference mirror is positioned with a piezoelectric linear actuator (ThorLabs PE6) driven by an MDT 694B controller (Thorlabs) to confirm alignment of the reference and probe beam paths. The recombined signal is collected with a photodiode (ThorLabs SM1PD1A) after passing through a 630 nm longwave pass filter. The photodiode signal is measured with a lock-in amplifier (Stanford Research Systems, SR830) synchronized to the chopper controller (Stanford Research Systems, SR540) and collected via custom built LabView program. A 405 nm laser diode is used as an excitation source and illuminates the sample from beneath the stage with an average fluence of 18-19.5 $\mu W/mm^2$. The excitation source is blocked with a programmable shutter to synchronize collection and exposure for the interferograms.

2.2.6 Modelling of Interferometry[7]

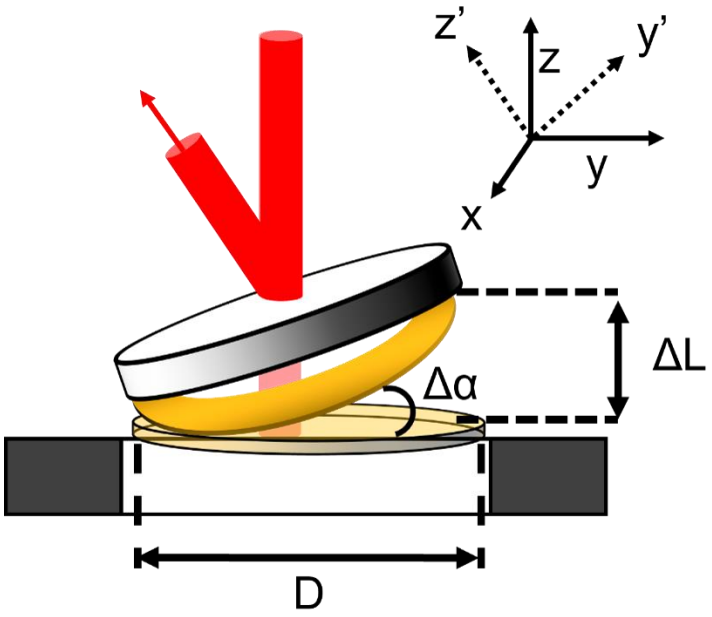

Figure 2.9 Cartoon of the Michelson interferometer at the sample beam path. When the template deforms and tilts the mirror, the angular displacement (Δα) and optical beam path difference (ΔL) can be coupled geometrically. This causes the sample beam path to tilt in the yz-plane, giving rise to the $E_2(x',y',z')$ field.

Once enough angular error has accrued on the probe beam path due to the sample's actuation, the two 632 nm beam paths no longer coincide on the photodiode's detector range. The photodiode is removed, and the beams are directed to the wall 4.9 m away from the sample stage. The center-to-center displacement is measured with a digital caliper and used to calculate the total angular displacement of the template.

The misalignment of a two-beam interferometer can be described as the intensity change in the sum of the two electric fields $E_1(x,y,z)$ and $E_2(x',y',z')$, where E_1 is the field from reference path and E_2 is the field from the misaligned sample path[1]. Assuming an infinite confocal parameter and radius of curvature while neglecting the Guoy phase shift, then the beam waist is also unchanged. If we consider only the misalignment in the yz-

plane with the tilt angle α resulting in an optical beam path difference L, then the fields can be described as:

$$E_1(x,y,z) = A \times \exp\left(-\frac{x^2+y^2}{w^2}\right) \times \exp(kz - \omega t)$$

$$E_2(x',y',z') = A \times \exp\left(-\frac{x'^2+y'^2}{w^2}\right) \times \exp(kz' - \omega t)$$

(eqn. 2.1)

where k is the wavevector of the laser source and A is the amplitude. If the angular tilt is assumed to be small, then $\sin(\alpha) \approx \alpha$, then the transformation of (x,y,z) → (x',y',z') can be simplified to:

$$x' = x$$

$$y' = y - (z - L)\alpha$$

$$z' = z - L + y\alpha$$

(eqn. 2.2)

After taking the sum of E_1+E_2 and simplifying, the intensity of the two combined beams is:

$$\iint |E_1 + E_2|^2 dxdy$$

$$I_{photo} = \iint I_0 \left(1 + \exp\left(-ik(y\alpha - L) - \frac{(-2y(z-L)\alpha) + (z-L)^2\alpha^2}{w^2}\right)\right) dxdy$$

$$\text{where } I_0 = A \times \exp\left(i\omega t - \frac{x^2+y^2}{w^2} - ikz\right)$$

(eqn. 2.3)

The evaluation of (eqn. 2.3) across an infinitely large xy plane evaluates to:

$$I_{photo} = (A^2 \pi w^2) \times$$

$$\left(1 + \exp\left(\frac{(-(k^2 w^4 + 4(L(t) - z)^2)\alpha(t)^2)}{8w^2}\right) \times \cos\left(kL(t) + \frac{k}{2}(L(t) - z)\alpha(t)^2\right)\right)$$

(eqn. 2.4)

where w is the beam waist, k is the wave number of the probe, z is the distance to the detector, L is the optical path difference, and α is the angular off-set. For the calculations used to model the 9MA filled templates, w = 1 × 10−3 m, k = 2π × 632.8×10^{-9} m^{-1}, z = 1 m and the factors due to the beam divergence and the Guoy phase shift have been neglected. Neglecting these factors is justified when the beam diameter is much greater than the optical wavelength and there is no focusing inside the interferometer. Assuming a linear time dependence of the Δα and ΔL such that L(t)=ΔL(t−t$_0$) and α(t)=Δα(t−t$_0$) where t$_0$ is the starting time for irradiation of the template, **(eqn.** 2.4) becomes:

$$I(t) = (A^2 \pi w^2) \times$$

$$\left(1 + \exp\left(\frac{-(k^2 w^4 + 4(\Delta L(t - t_0) - z)^2)(\Delta\alpha(t - t_0)^2)}{8w^2}\right) \times \ldots\right.$$
$$\left. \ldots \cos\left(k\Delta L(t - t_0) + \frac{k}{2}(\Delta L(t - t_0) - z)\left(\Delta\alpha(t - t_0)\right)^2\right)\right)$$

(eqn. 2.5)

which assumes that ΔL and Δα are independent, but if a circular template of diameter D tilts by an angle Δα, then the following substitution can be made into **(eqn.** 2.5) using the small angle approximation:

$$\Delta L(t) \approx \frac{D}{2} \times \Delta\alpha(t - t_0)$$

(eqn. 2.6)

2.2.7 Density of AAO Templates[1]

The skeletal density of the AAO templates is determined using Archimedes principle to measure the weight of individual templates first in air and then in ethanol to mitigate formation of air bubbles on the surface of the sample. Samples are measured in a mesh weigh boat suspended from the eyelet on the bottom face of the scale (AND HR120 analytical balance) so that the samples can be submerged in the auxiliary liquid. The temperature of the auxiliary liquid is monitored with a k-type thermocouple. The apparent weights are used in the following equation to determine the density of the sample ρ_i:

$$\rho_i = \frac{W_{air}}{W_{air} - W_{EtOH}}(\rho_{air} - \rho_{EtOH}) + \rho_{EtOH}$$

(eqn. 2.7)

where W_{air} is the weight in air, W_{EtOH} is the weight in ethanol, ρ_{air} and ρ_{EtOH} are the densities of air and ethanol respectively. The skeletal density is averaged across 10 different AAO templates and a cartoon of the set-up is included below:

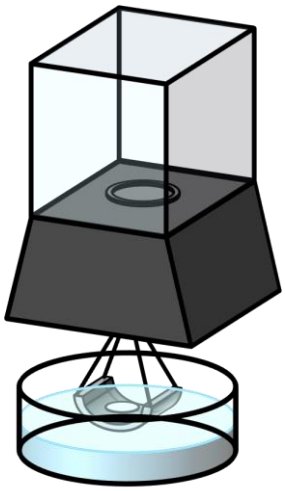

Figure 2.10 Cartoon of the apparatus used to measure the skeletal density of the AAO templates. Individual templates are supported in a mesh weigh boat and first measured in air, then completely submerged in the auxiliary liquid.

From the skeletal density (ρ_{skele}) of the AAO, we can determine the effective porosity of the templates. Given that a 60 µm thick, 13 mm diameter disk solid disk (V_{disk}) would have a volume of ≈ 7.96×10^{-2} cm^3, then it should have a weight of $W_{disk} = \rho_{skele} \times V_{disk} \approx$ 23.9 mg. Using the average observed weight of the porous template, W_{AAO} = 10.0 ± 0.1 mg, then the volume of the void space and the porosity (P) of the template can be calculated using:

$$V_{void} = \frac{W_{disk} - W_{AAO}}{\rho_{skele}}$$

$$P = \frac{V_{void}}{V_{disk}} = \frac{W_{disk} - W_{AAO}}{W_{disk}} = 1 - \left(\frac{W_{AAO}}{W_{disk}}\right)$$

(eqn. 2.8)

Using **(eqn.** 2.8), the porosity of the templates used in chapter 6 is approximately 58 ± 0.6 % and corresponds to ≈ 4.7 mg of 9MA as the weight of theoretical maximum fill.

2.2.8 Water Contact Angles for Functionalized Templates[1]

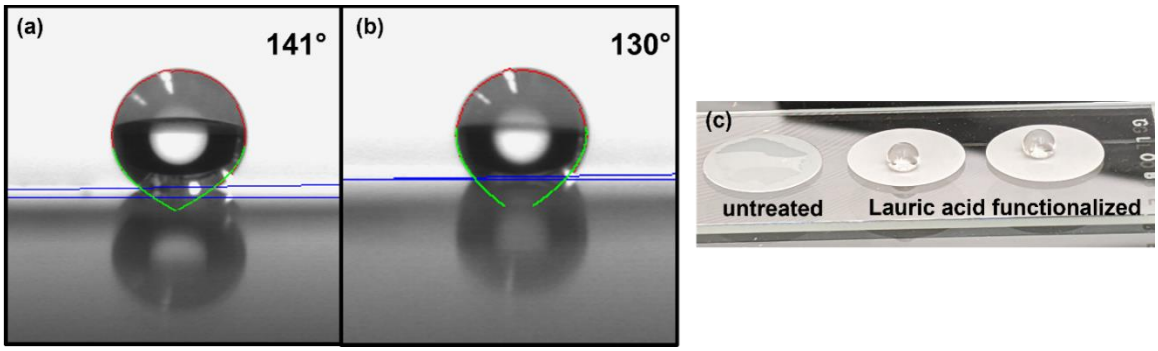

Figure 2.11 (A-b) Contact angle measurements of a 50 µL water droplet on a LA-functionalized AAO surface. Samples demonstrate superhydrophobic surfaces with contact angles ≥ 130°. The untreated AAO templates are sufficiently hydrophilic to form contact angles below the limit of detection of the instrumentation. Side by side qualitative comparisons are captured in **(c)** using 100 µL of water added to each surface via micropipette.

The water contact angles of the functionalized templates were measured using a Kruss D04010 EasyDrop system (Matthews, NC, USA) with a 50 µL droplet of water. Two lauric-acid functionalized templates and one bare template were tested to demonstrate the change in the hydrophilicity.

2.2.9 Scanning Electron Microscopy[8]

For the SEM measurements in chapter 6, polished AAO templates were cut into quarters with a razor blade. Two portions of the template were exposed to UV (405 nm laser) while the remaining pieces were kept in the dark as reference samples. The samples were then fixed to a glass slide using polyimide tape before coating with Au using electron beam evaporation (Temescal BJD 1800). The samples were imaged under a 10.0 kV electron beam in a Zeiss Leo XB 1540 microscope.

2.2.10 Atomic Force Microscopy[9]

For the AFM measurements in chapter 6, filled templates were fixed to a magnetic stage with double-sided tape and imaged using a tapping mode AFM (AFM Probe NSG01, NT-MIDT Spectrum Instruments, Digital Instruments Nanoscope IIIA). The samples were irradiated in-situ using a 405 nm laser diode that was attenuated to 50 mW before passing through a diffuser. Higher laser intensities could not be used due to the damage that is caused by the heating of the gold-coated SiC probe tip.

2.2.11 Brightfield Microscopy

Microfibers are imaged using Leica DM2700M and Olympus IX70 transmission microscopes. For PEO-8M microfibers, photomechanical dopants are excited using a 405 nm dichroic beam splitter to illuminate the sample with the Hg lamp built into the Olympus

IX70 microscope. Images and videos are recorded through the camera port beneath the binoculars.

2.3 Calculations

2.3.1 Brute force search for 1D Harmonic Oscillator Model[10]

All calculations are performed in Mathematica 12.3 using custom functions defined from the 1-D harmonic oscillator model. Using the definitions in (eqn. 5.4(eqn. 5.5, a matrix for the simplified Hamiltonian is constructed:

$$H_{tot} = \begin{bmatrix} E_a & V \\ V & E_b \end{bmatrix}$$

The potential energy surfaces (PES) $\lambda_{\pm}$ are constructed by evaluating the Eigenvalues of H_{tot} using the built-in function, giving the expanded form of (eqn. 5.3. The expressions are generated using the following:

```
Evalues = Eigenvalues[Htot]
λminus = Evalues[[1]]
λplus = Evalues[[2]]
```

For convenience in later calculations, a custom function is defined from the symbolic form of eqn. 3. using the replacement function (note that subscripts are avoided when defining the variables to prevent errors when referencing and replacing values):

```
LminusFxn[Ka_, Kb_, Xa_, Xb_, Delta_, Coupling_, Force_] :=
λminus/.{ka->Ka, kb->Kb, xa->Xa, xb->Xb, Δ->Delta, V->Coupling, A-
>Force}

LplusFxn[Ka_, Kb_, Xa_, Xb_, Delta_, Coupling_, Force_] := λplus/.{ka-
>Ka, kb->Kb, xa->Xa, xb->Xb, Δ->Delta, V->Coupling, A->Force}
```

Afterwards, the first and second derivatives are evaluated from symbolic form of λ_{-}, creating the λminusD, λminusD2 derivative expressions used to tract the extrema in the

lower PES. Similar to the process above, custom functions are generated using the replacement function and the derivative expressions:

```
LminDfxn[Ka_, Kb_,  Xa_,Xb_, Delta_, Coupling_, Force_] :=
λminusD/.{ka->Ka, kb->Kb, xa->Xa, xb->Xb, Δ->Delta, V->Coupling, A-
>Force}

LminD2fxn[Ka_, Kb_, Xa_, Xb_, Delta_, Coupling_, Force_] :=
λminusD2/.{ka->Ka ,kb->Kb, xa->Xa, xb->Xb, Δ->Delta, V->Coupling, A-
>Force}
```

Together, these two expressions can be used to determine the location of the minima along the lower PES :

```
LminimaXfxn[Ka_, Kb_, Xa_, Xb_, Delta_, Coupling_, Force_] :=
 x /. Solve[
   LminDfxn[Ka, Kb, Xa, Xb, Delta, Coupling, Force] == 0 &&
    LminD2fxn[Ka, Kb, Xa, Xb, Delta, Coupling, Force] > 0, x]
```

Counting the minima along λ_- for any particular set of k_a, k_b, x_a, x_b, Δ, V, and A is accomplished using:

```
LminimaCheckFxn[Ka_, Kb_, Xa_, Xb_, Delta_, Coupling_, Force_] :=
Count[LminimaXfxn[Ka, Kb, Xa, Xb, Delta, Coupling, Force], _Real]
```

Once the location of the minima is determined, the photon energy cost can be calculated for either the forward or reverse reaction using the following function:

```
Ephoton[Ka_, Kb_, Xa_, Xb_, Delta_, Coupling_, Force_,
  X1_] := ((λplus - λminus) /. {ka -> Ka, kb -> Kb,
     xa -> Xa, xb -> Xb, Δ -> Delta, V -> Coupling,
     A -> Force}) /. x -> X1
```

Due to the absence of a neat analytical solution for A_{stop} when $V \neq 0$, a numerical brute force search is employed according to the flowchart below:

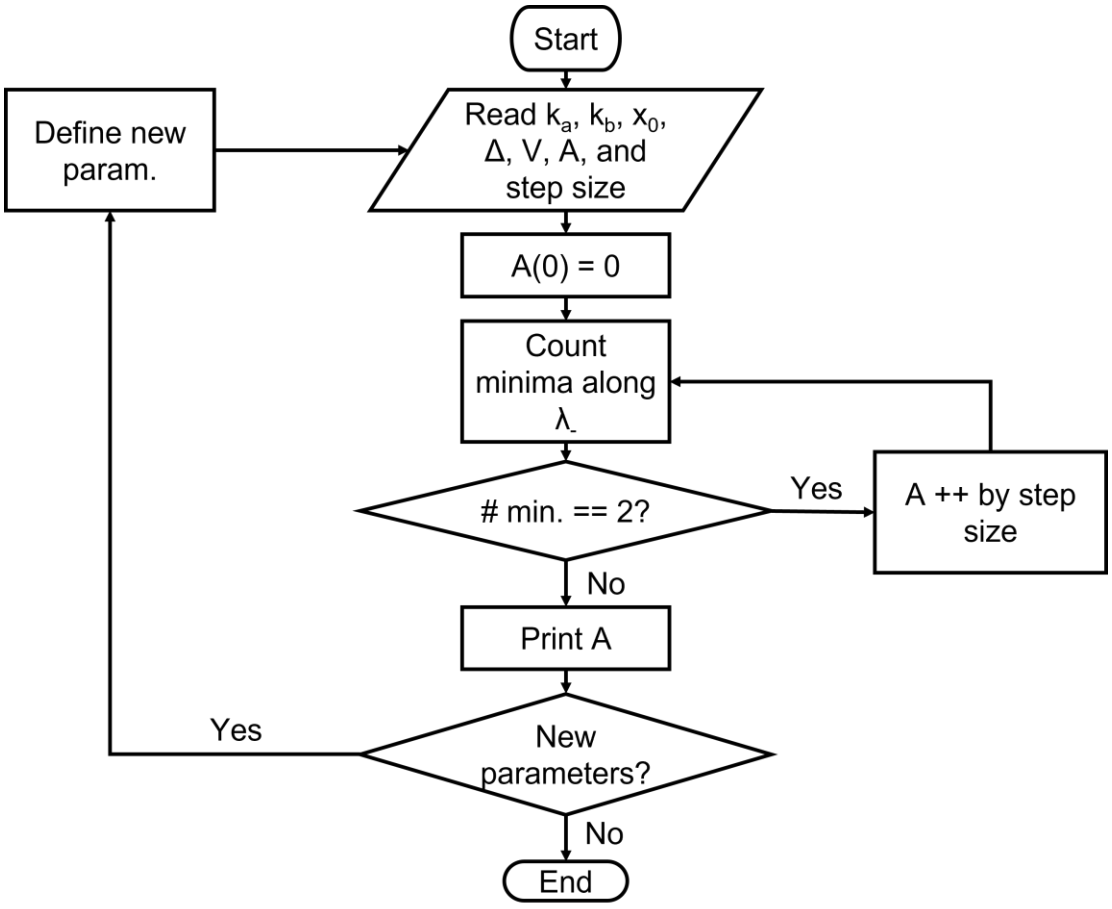

Figure 2.12 Flowchart describing the brute-force algorithm for determining the stopping force of a photomechanical molecular system where $V \neq 0$.

It is important to note, however, that the accuracy of the brute force search is limited by the magnitude of the step size. For large values of x_0 and small values of V, the system can endure large forces, which makes finer step sizes computationally taxing.

2.4 References

(1) Berges, A. J.; Li, W.; Xu, W.; Tong, F.; Al-Kaysi, R. O.; Hayward, R. C.; Bardeen, C. J. Photomechanical Structures Based on Porous Alumina Templates Filled with 9-Methylanthracene Nanowires. *Crystals* **2022**, *12* (6), 808.

(2) Norek, M.; Krasiński, A. Controlling of water wettability by structural and chemical modification of porous anodic alumina (PAA): Towards super-hydrophobic surfaces. *Surface and Coatings Technology* **2015**, *276*, 464-470. DOI: https://doi.org/10.1016/j.surfcoat.2015.06.028.

(3) Zhu, L.; Tong, F.; Salinas, C.; Al-Muhanna, M. K.; Tham, F. S.; Kisailus, D.; Al-Kaysi, R. O.; Bardeen, C. J. Improved Solid-State Photomechanical Materials by Fluorine Substitution of 9-Anthracene Carboxylic Acid. *Chemistry of Materials* **2014**, *26* (20), 6007-6015. DOI: 10.1021/cm502866e.

(4) Lee, H.; Inoue, Y.; Kim, M.; Ren, X.; Kim, I. S. Effective Formation of Well-Defined Polymeric Microfibers and Nanofibers with Exceptional Uniformity by Simple Mechanical Needle Spinning. *Polymers* **2018**, *10* (9), 980.

(5) Hausch, J.; Berges, A. J.; Zeiser, C.; Rammler, T.; Morlok, A.; Bredehöft, J.; Hammer, S.; Pflaum, J.; Bardeen, C. J.; Broch, K. Distinguishing between Triplet-Pair State and Excimer Emission in Singlet Fission Chromophores Using Mixed Thin Films. *The Journal of Physical Chemistry C* **2022**, *126* (15), 6686-6693. DOI: 10.1021/acs.jpcc.1c09297.

(6) D'Agostino, G.; Robertsson, L. Relative beam misalignment errors in high accuracy displacement interferometers: calculation and detection. *Applied Physics B* **2011**, *103* (2), 357-361. DOI: 10.1007/s00340-010-4321-2.

(7) Smith, R.; Fuss, F. K. Theoretical Analysis of Interferometer Wave Front Tilt and Fringe Radiant Flux on a Rectangular Photodetector. *Sensors* **2013**, *13* (9), 11861-11898.

(8) Mamada, M.; Katagiri, H.; Mizukami, M.; Honda, K.; Minamiki, T.; Teraoka, R.; Uemura, T.; Tokito, S. syn-/anti-Anthradithiophene Derivative Isomer Effects on Semiconducting Properties. *ACS Applied Materials & Interfaces* **2013**, *5* (19), 9670-9677. DOI: 10.1021/am4027136.

(9) Zwadlo, M.; Hagara, J.; Duva, G.; Hagenlocher, J.; Gerlach, A.; Zaluzhnyy, I.; Hodas, M.; Hinderhofer, A.; Siffalovic, P.; Schreiber, F. Structure of Thin Films of [6] and [7]Phenacene and Impact of Potassium Deposition. *Advanced Optical Materials* **2021**, *9* (14), 2002193. DOI: 10.1002/adom.202002193.

(10) Berges, A. J.; Bardeen, C. J. Analysis of molecular photomechanical performance using a one-dimensional harmonic model. *Photochemical & Photobiological Sciences* **2022**. DOI: 10.1007/s43630-022-00261-9.

Chapter 3. The Role of Excimer Formation and Charge-Transfer Intermediate in Triplet-Sensitized Upconversion of Pyrene Solutions

We begin the study of multi-exciton materials with the investigation of the charge-transfer intermediate and interaction distance of triplet-triplet annihilation (TTA). By sensitizing the triplet population of pyrene with a metal centered organic, triplets in pyrene can be generated without direct stimulation, thus any excimer fluorescence observed is the direct result of singlets formed by TTA. Here, we develop a method to decompose time-resolved fluorescent spectra of up-converted pyrene into its monomer and excimer components. The ratio of the excimer to the monomer provides spatial information on the TTA mechanism and suggests a long-range mechanism is at play.

3.1 Introduction

Triplet-triplet annihilation (TTA) and photon upconverting (UC) materials have enjoyed a renewed interest compared to their earlier studies in mid 1960s[1-4]. With advances in triplet sensitization[5, 6], nanoparticle functionalization[7, 8], and polymerization[9, 10], TTA-UC materials are now able to convert a broad range of wavelengths into higher energy photons depending on the chosen sensitizer and emitter[6]. With many prospective applications including solar energy[11], bio-imaging[12], optical data storage[13], organic light emitting diodes (OLEDs)[13, 14], and optogenetics[15], the attention TTA-UC materials have drawn is warranted. This attention is accompanied by several investigations into the mechanism behind TTA[16] and its counterpart singlet-fission (SF)[17, 18]. The fusion of two triplets into a higher energy singlet, triplet, or quintet, leaves behind several questions regarding the correlated triplet pair intermediate (^{1}(TT)) and the nature of the energy

transfer in this spin-allowed process. Direct observation of ^{1}(TT) is challenging but possible with NIR transient absorption spectroscopy[8, 19-21] and photoluminescent spectroscopy via Herzberg-Teller coupling[22, 23]. Since many of the organic molecules historically associated with TTA and SF also form excited dimers (excimers)[1, 4, 24, 25], several studies have tried to discern whether this state is conducive to TTA[26, 27] and SF[28, 29] and how it relates to the ^{1}(TT) intermediate.

As new information emerges about ^{1}(TT), old questions concerning the interaction distance of TTA and the formation of the excimer are raised. Early studies of TTA in pyrene concluded that the excimer was preferentially, if not directly, formed by TTA[1, 4, 24, 30]. Due to the increase in excimer to monomer (E/M) emission during prompt and delayed fluorescence, it was originally thought the excimer was formed due to the narrow interaction distance and solvent cage involved in TTA, thereby excluding an excited singlet-ground state re-encounter model in several derivatives of pyrene[30]. However, the increased E/M intensities may be due to nuances of the molecule's photophysics, as the inner-filter effect[31, 32] suppresses monomer fluorescence while direct excitation further obfuscates the relationship of both species in delayed fluorescence. Triplet sensitization alleviates some of these issues as the indirect population of pyrene triplets results in monomer fluorescence caused solely by TTA. Since TTA is commonly thought to occur through a Dexter type energy transfer (DET)[33, 34] mechanism, intermolecular distances in the range of a nanometer are expected, which correlates to a large local concentration of pyrene. If the DET includes a two-step, one electron exchange between the ^{1}(TT), one might then expect the fluorescent spectrum generated through sensitized TTA to be

exclusively excimer, but this is not what is observed[5, 35]. Furthermore, derivatives of pyrene that prevent excimer formation through steric hindrance do not suffer the same penalties when undergoing TTA[5]. This suggests that a longer-range mechanism might be accessible to solutions of pyrene since the reduced diffusion and increased intermolecular distance between two sterically hindered derivatives do not prevent upconversion. In this chapter, we seek to elucidate the role of the excimer during TTA through triplet sensitization using the well-studied pyrene and tris(2-phenylpyridine) iridium (III) system. By using time-resolved photoluminescence to screen out the sensitizer's emission and applying spectral decomposition to accurately assign the monomer and excimer areas, our results suggest that the re-encounter model is the likely mechanism and that TTA is occurring at an interaction distance that is larger than the critical excimer formation radius.

3.2 Results and Discussion

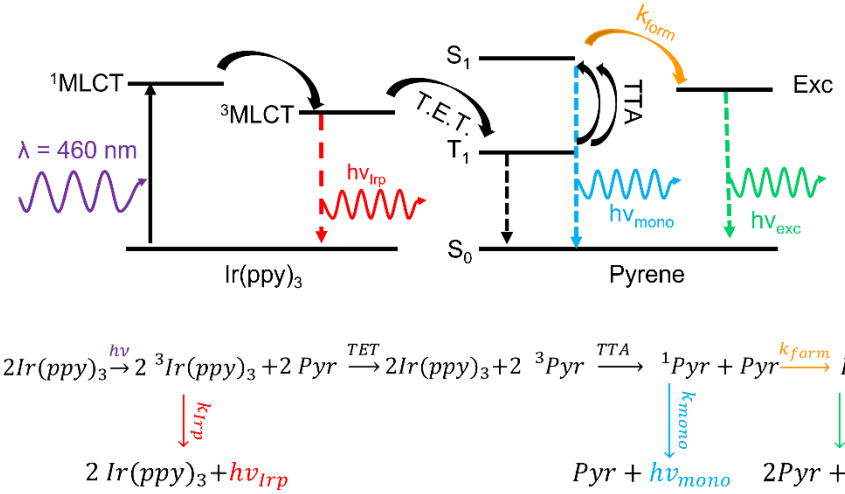

Figure 3.1 Reaction scheme and Jablonksi diagram for the triplet-sensitized upconversion of pyrene in solution. There are three major radiative relaxation pathways available: $Ir(ppy)_3$ luminescence (red), pyrene monomer fluorescence (blue), and pyrene excimer fluorescence (green).

Figure 3.1 above describes the relaxation pathways available to pyrene and $Ir(ppy)_3$ following excitation of the annihilator (**Figure 3.1b**) or sensitizer (**Figure 3.1a**). Selective excitation of $Ir(ppy)_3$ on the shoulder of the $S_0 \rightarrow S_1$ transition yields efficient intersystem crossing (ISC) via the metal-ligand charge transfer (MLCT) band, enabling $Ir(ppy)_3$ to transfer energy into pyrene via triplet-energy transfer (TET) without any direct excitation of annihilator[5] (**Figure 3.2a**). However, the overlapping fluorescence of the three species ($h\nu_{mono}$, $h\nu_{exc,}$ and $h\nu_{Ir(ppy)3}$ respectively in **Figure 3.1** presents two challenges when analyzing the upconverted spectra. First, lingering photoluminescence from the sensitizer (475-680 nm) significantly overlaps with the pyrene excimer fluorescence (400-650 nm) and obscures the excimer population, whilst moderate overlap of the monomer and excimer (390-500 nm) region compounds the issue (**Figure 3.2b**).

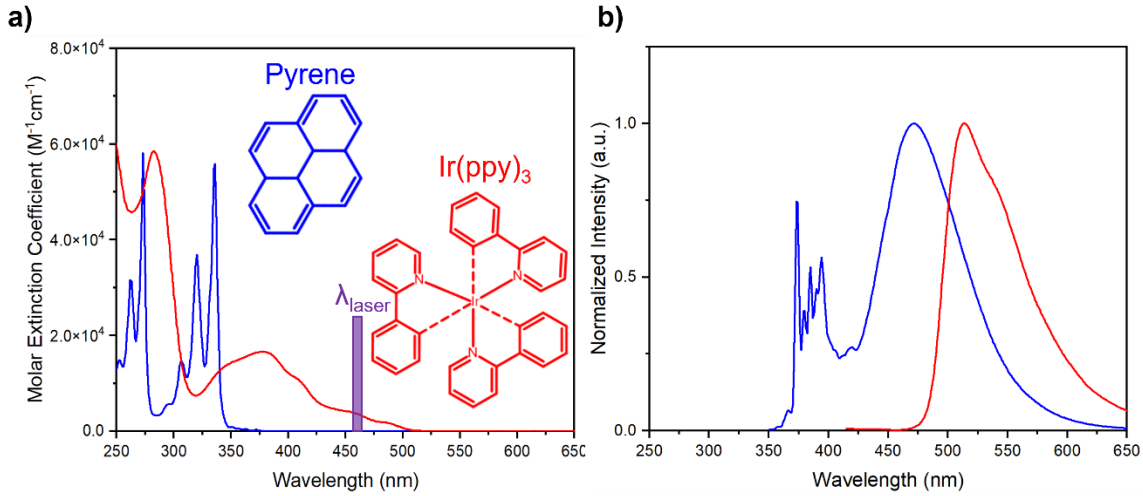

Figure 3.2 Steady state spectra of pyrene (blue) and $Ir(ppy)_3$ (red). **a)** Molar extinction data for pyrene and Ir(ppy)3, with the 460 nm laser excitation source in purple and **b)** fluorescent emission for ≈ 10-3 M solution of pyrene and 10-5 M solution of Ir(ppy)3 in THF.

The former can be solved by time-gating the sensitizer's quenched luminescence, but the latter issue requires a deeper spectral analysis of pyrene's fluorescent emission. At the dilute limit (10^{-4}-10^{-5} M), direct excitation of pyrene leads to exclusively monomer fluorescence, as the singlet relaxation outcompetes excimer formation. Fitting the spectral features under these conditions reveals 9 peaks spanning from 360-400 nm, with 2 broad shoulders extending into the 400-500 nm region. These 11 peaks remain in concentrated solutions, where the addition of 2 broader, red-shifted peaks constitute the familiar excimer fluorescence. The entire fluorescent spectrum of pyrene can then be described with these 13 peaks, as depicted in **Figure 3.3** for a de-aerated tetrahydrofuran (THF) solution. For any concentration of pyrene, the fluorescence spectrum can be described as a linear combination of its monomer and excimer components using (eqn. 3.1).

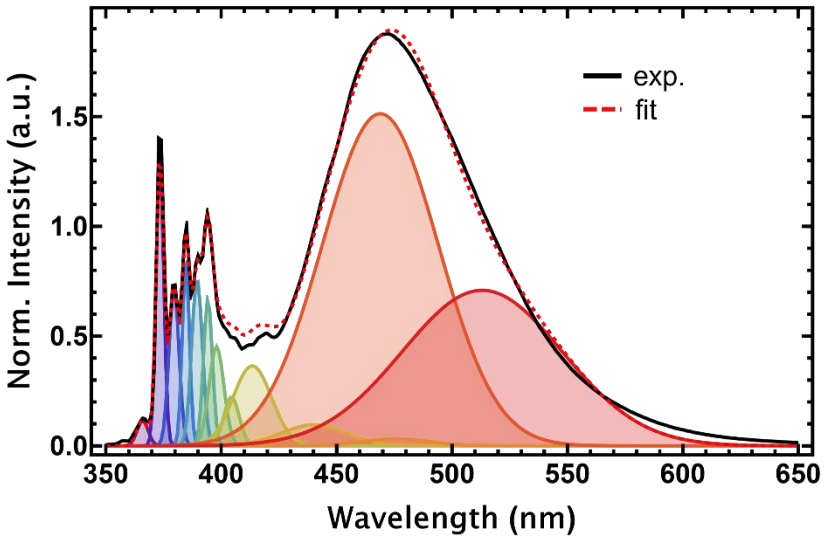

Figure 3.3 Decomposition of the steady state fluorescent spectrum for concentrated pyrene in THF solution. Each of the thirteen peaks are plotted beneath the experimental data (black) and the corresponding fit (red, dashed).

$$I(\lambda) = w_1 \times I_{mono}(\lambda) + w_2 \times I_{exc}(\lambda)$$

(eqn. 3.1)

where $I_{mono}(\lambda)$ and $I_{exc}(\lambda)$ correspond to their respective fluorescent intensities at the specific wavelength λ. Thus, any fluorescent spectrum of pyrene in a particular solvent can be fit by varying the weights w_1 and w_2 without having to refit all 13 peaks. **Figure 3.4** demonstrates this approach in several de-aerated solutions of pyrene in THF and the fit's agreement with the experimental observation. Once each weight is determined from the fit, the relative excimer and monomer populations can be calculated using their respective peak areas:

$$\frac{E}{M} = \frac{w_2 \times \int I_{exc}(\lambda) d\lambda}{w_1 \times \int I_{mono}(\lambda) d\lambda}$$

(eqn. 3.2)

The peak assignment of the monomer and excimer species need only be completed once per solvent to account for perturbations caused by diffusion and the local polar environment, allow (eqn. 3.2) to be calculated for a high throughput of samples. Extending this approach to the sensitized solutions clarifies the relative populations of the pyrene monomer and excimer after TTA. In each sensitized solution, the concentration of $Ir(ppy)_3$ is maintained at ≈ 50 μM with an excess of the annihilator to mitigate energy transfer back into the sensitizer. However, due to the spectral overlap of the pyrene monomer and $Ir(ppy)_3$'s metal-ligand charge transfer (MLCT) band[36], energy transfer back into the sensitizer cannot be entirely excluded, although such energy transfer will eventually result

in population of the pyrene triplet as $Ir(ppy)_3$ is both significantly quenched by pyrene and has an ISC approaching unity.

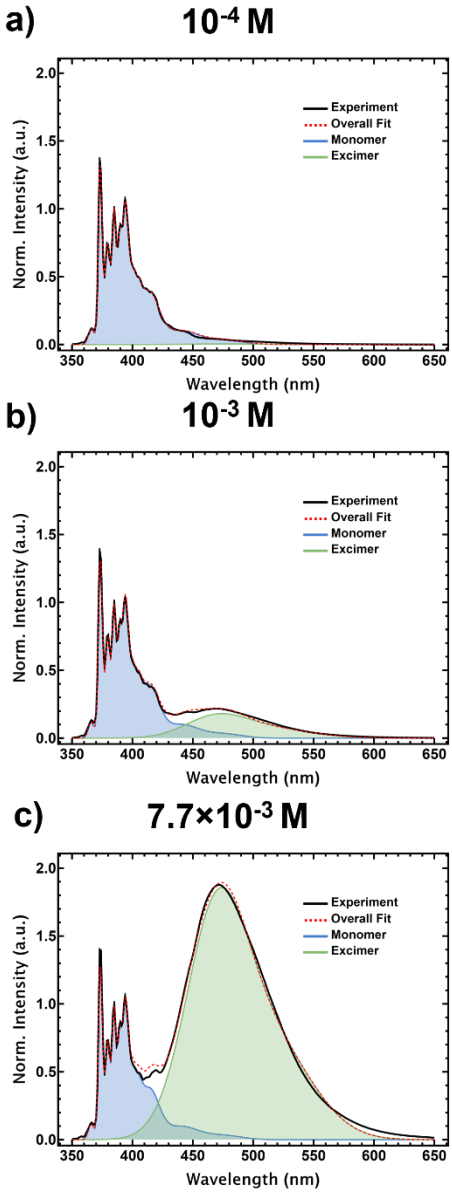

Figure 3.4 Fitting of the fluorescent spectra for several solutions of pyrene in THF. At the lowest concentration **(a)**, the weight of the excimer component is effectively zero and increases in the more concentrated **(b,c)** samples. Areas of the monomer (blue) and excimer (green) components are overlaid on top of the experimental data (black), in addition to the overall fit (red, dashed).

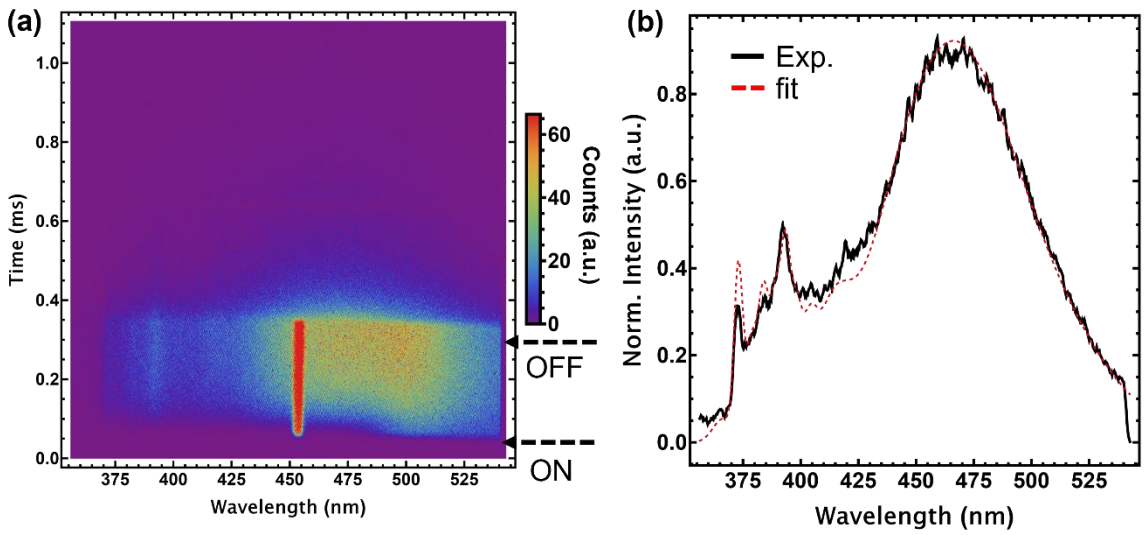

Figure 3.5 Sensitized up-conversion spectra for ≈ 3 mM pyrene sensitized with ≈ 50 μM $Ir(ppy)_3$. **(A)** The streak camera image of the time-resolved photoluminescent spectra in a 1 ms window. The remainder of the time window is integrated to produce the 2D fluorescent spectrum in **(b)** and is normalized to highest intensity in the upconverted spectrum. The overlaid fit is used to determine the relative areas of the monomer and excimer population.

In the upconverted solutions, the sensitizer is stimulated with a 250 μs pulse and emits its photoluminescence throughout the duration of the pulse (**Figure 3.5a**). Neither the pyrene monomer nor excimer fluorescence is observed until almost 50 μs into the pulse. At higher concentrations of pyrene, the $Ir(ppy)_3$ luminescence expires almost immediately after the pulse ends. Integration of the time window after the pulse concludes reveals the upconverted spectrum (**Figure 3.5b**) with the absence of $Ir(ppy)_3$, which is then fit using (eqn. 3.1). Due to differences in the spectral sensitivity of the steady state and time-resolved spectrometers, the parameters for the 13 peaks need to be reanalyzed for the upconversion experiment. Peak positions agree within 0.3 and 3% for the monomer and excimer respectively, and as seen in **Figure 3.5b**, still adequately captures the upconverted

fluorescence. Becoming a larger issue at higher concentrations, self-absorbance of the monomer emission distorts the spectrum and requires treatment to remove this inner-filter effect. This correction is performed similarly to previous examples in the literature[31] using (eqn. 3.3)-(eqn. 3.4).

$$\kappa(\lambda) = A_{soln}(\lambda, b) + A_{soln}(\lambda_{laser}, b)$$

(eqn. 3.3)

$$I_{corr}(\lambda, b) = \frac{I_0(\lambda, b)\kappa(\lambda, b)}{1 - \exp\big(-\kappa(\lambda, b)\big)}$$

(eqn. 3.4)

where I_0 is the observed fluorescence, A_{soln} is the optical density of the solution at that specific wavelength λ and beam-path b , and λ_{laser} is the excitation wavelength. Surprisingly, the upconverted spectra exhibit a suppressed 0-0 peak intensity even after self-absorbance has been corrected and is perhaps the first indication of an increased local concentration. When compared to their counterparts in direct excitation, the upconverted solutions exhibit an enhanced excimer fluorescence which is most apparent at higher concentrations (**Figure 3.6**), further supporting an increased local concentration following upconversion. If TTA is proceeding through a DET mechanism, then intermolecular distances resultant from the correlated triplet pair ought to be in the sub-nanometer regime, which would lead to a drastic increase in local pyrene concentration. One would then expect the excimer enhancement to be most pronounced at the lower concentrations ($\leq 10^{-4}$ M) of pyrene, but here the effect is barely observable.

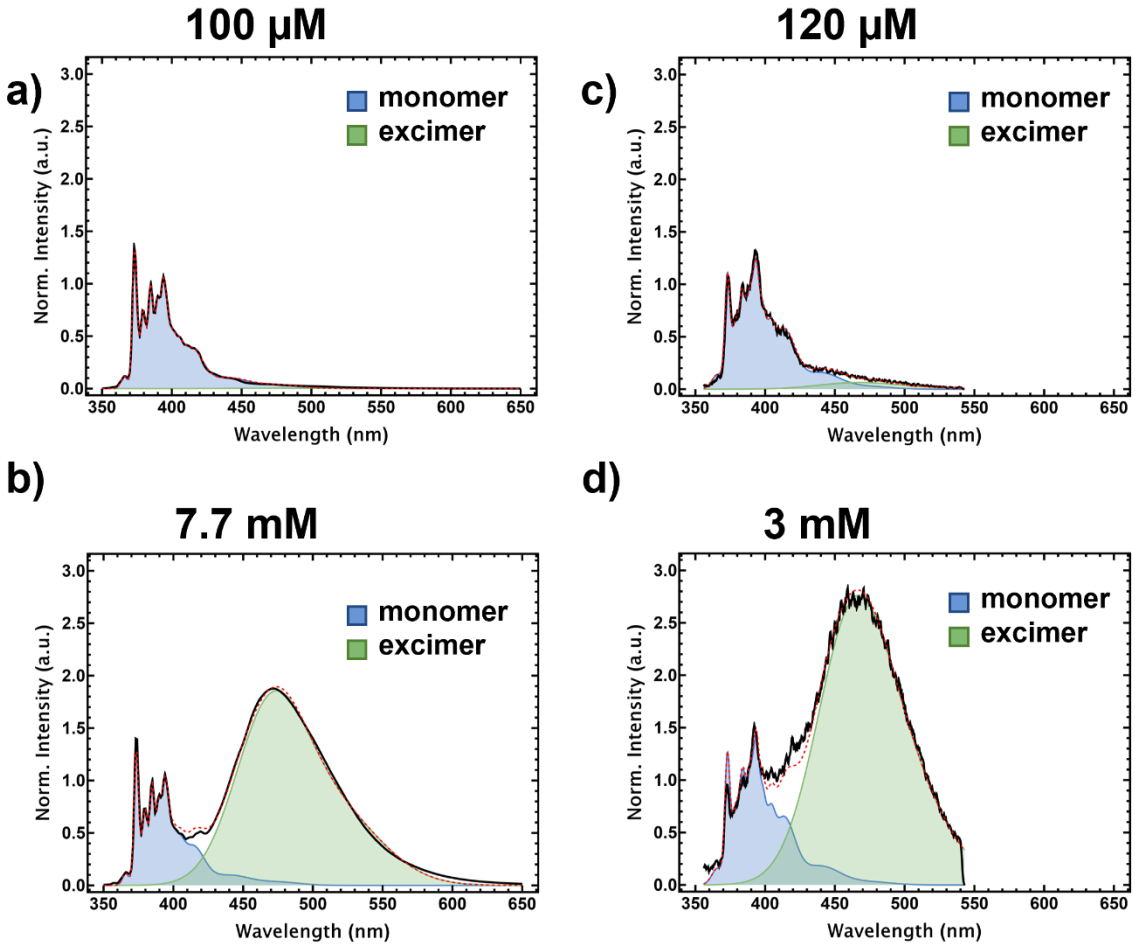

Figure 3.6 Steady state (**a,b**) and upconverted (**c,d**) fluorescent spectra for solutions of pyrene in THF. There is significant enhancement in the excimer signal after TTA in concentrated ($>10^{-3}$ M) solutions, with a minor effect in lower concentration ($\leq 10^{-4}$ M). Due to the spectral resolution of the instrument, the upconverted spectra terminate at ≈ 545 nm. For the sensitized solutions, ≈ 50 µM $Ir(ppy)_3$ is used to generate the triplet population.

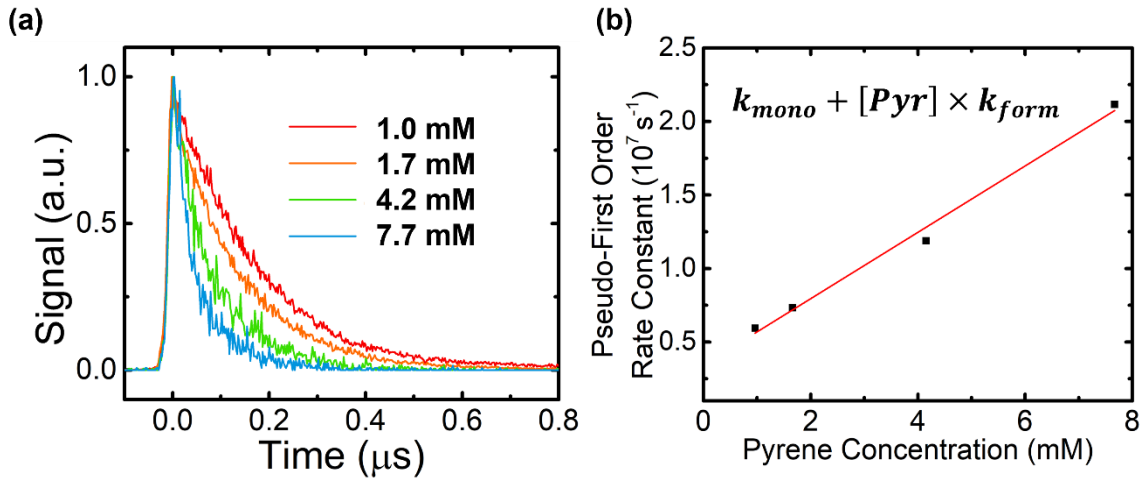

Figure 3.7 Time-resolved photoluminescent decays for the direct excitation of de-aerated pyrene solutions in THF. The self-quenching evident in the monomer spectrum **(a)** results in the formation of the excimer and the slope accompanying Stern-Volmer type plot **(b)** reveals the rate of excimer formation k_{form}.

Table 1 Comparison of photophysical rate constants for pyrene (k_{mono}, k_{form}, k_{exc}) and $Ir(ppy)_3$ ($k_{Ir(ppy)3}$) and their respective solvent viscosities (η).

	This work	ref. 36	ref. 32	ref. 36
Solvent	THF	cyclohexane	decane	toluene
η (mPa·s)	0.456 [37]	0.894 [37]	0.838 [37]	0.56 [37]
k_{mono} (s^{-1})	3.40×10^6	2.25×10^6	2.38×10^6	-
k_{form} (M^{-1} s^{-1})	2.30×10^9	6.7×10^9	3.11×10^9	-
k_{exc} (s^{-1})	1.29×10^7	1.55×10^7	2.78×10^7	-
$k_{Ir(ppy)3}$	9.8×10^5	-	-	1.0×10^6

To shed light on this phenomenon, it is necessary to return to pure solutions of pyrene and $Ir(ppy)_3$ to analyze the diffusion limited rate of excimer formation. Although pyrene has been extensively studied in non-polar solvents[32, 38], there is limited information on the excimer kinetics in THF. The rate of excimer formation can be extracted from a Stern-Volmer type analysis (**Figure 3.7b**) of the apparent monomer fluorescent lifetime (**Figure 3.7a**). The solvent properties and kinetics are summarized in **Table 1** and

demonstrate rates comparable to literature[32, 36, 38] in all but k_{form}. It is emphasized that the solutions of THF in this work are not dried, and since no precautions were taken to limit water content, it is possible that these solutions had a significant amount of water co-dissolved. Binary solutions of water and THF can become quite viscous ($\eta \geq 1$ mPa·s) as water content increases[39], and thus the upconverted solution's viscosity may have been closer to decane and cyclohexane. This may explain why the rate of excimer formation appears slower in THF but does not explain the lack of excimer enhancement in dilute solutions. Using the Smoluchowski expression[40] and diffusion data reported in the literature, the critical encounter radii for excimer formation is tabulated below in **Table 2**.

Table 2 Critical pyrene encounter radii for excimer formation (R^*_{exc}) calculated from different solvents and their respective k_{form}.

Solvent	η (mPa·s)	Diffusion Coefficient ($\times 10^9$ m^2 s^{-1})	$\mathbf{R^*_{exc}}$ (Å)
THF	0.456 [37]	1.58 [41]	1.9
Decane	0.838 [37]	1.23 [42]	3.3
Cyclohexane	0.894 [37]	1.81 [42]	4.9

Although this is only an approximation of the encounter radius, it is evident that the excimer is formed within nanoseconds from a singlet excited-ground state pair as long as they are within 2-5 Å of each other and k_{form} is on the order of 10^9 M^{-1} s^{-1}. It is puzzling, then, why the upconverted fluorescence does not exclusively come from the excimer, as this encounter radius is conducive to efficient DET and even dilute solutions of pyrene must be within this radius. Considering that pyrene is an exothermic annihilator, relaxation of some high lying S_n^* excited state formed through TTA would vibrationally relax within a few ps[43]. Even at 100 ps, a pyrene molecule has a diffusive length between 1.2-4.3 Å in

these solvents, which would still be within the excimer encounter radius following TTA and cannot completely explain this behavior.

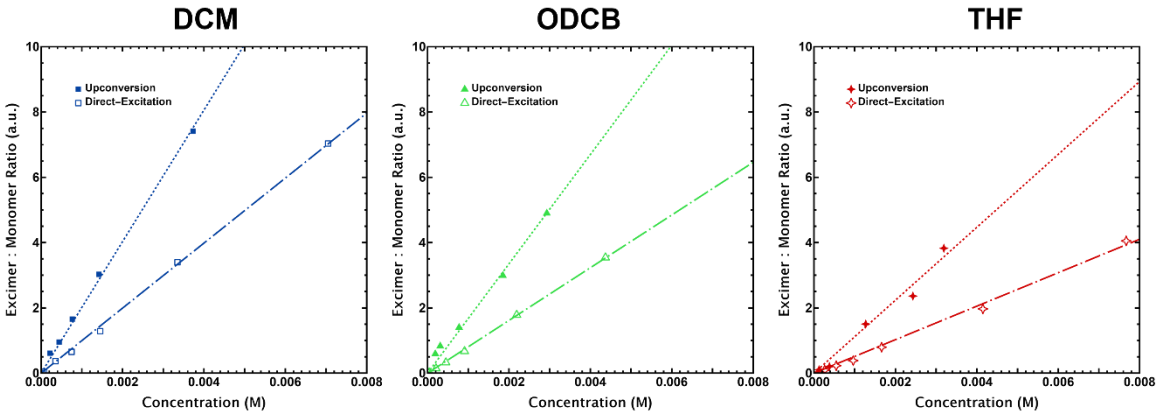

Figure 3.8 Plots of the E/M integrated area ratios for the upconverted spectra in **a**) methylene chloride, **b**) ortho-dichlorobenzene, and **c)** tetrahydrofuran. In all three cases, the slope for the upconverted solutions is increased by ≈ 2, with no obvious effect in increased viscosity. In each upconversion series, the concentration of pyrene is within 10^{-5}-3.5×10^{-3} M with a sensitizer concentration of ≈ 40-50 μM.

The upconversion experiment is repeated in de-aerated dichloromethane (DCM) and orthodichlorobenzene (ODCB) to exclude any secondary effects that could be caused by water content. Although similar in dielectric strength, ODCB is over three times as viscous as DCM and is a good candidate for directly comparing the diffusion limitation of excimer formation following TTA. In all three solvents, excimer enhancement is more pronounced at higher concentrations of pyrene with E/M of 0 when extrapolated at the infinitesimal limit (**Figure 3.8**). Plotting these ratios against the concentration of pyrene reveals a factor of ≈ 2 increase in the slope for upconverted spectra, regardless of the solvent viscosity. For pyrene in the absence of sensitization, careful solution of the kinetics reveals the relationship E/M in (eqn. 3.5).

$$\frac{E}{M} = \frac{\Phi_{exc} k_{form}}{\Phi_{mono} k_{exc}} \times [Pyr]$$

(eqn. 3.5)

The quantum yield for the pyrene monomer is well established, but little to no data exists on the quantum yield for the excimer in solution and typically only relative yields are reported. Unfortunately, the competing, interdependent pathways in the sensitized TTA kinetics prevent a neat solution for the E/M as seen in (eqn. 3.5). As such, the origin of the twofold increase is not apparent as intermolecular distances immediately after TTA would be nearly an order of magnitude greater at the infinitesimal limit. The slopes from **Figure 3.8** are summarized in **Table 3**, where the direct excitation data suggests an inversely proportional dependence on solvent viscosity. As E/M $\propto k_{form}$, which is a diffusion limited rate, this is not altogether surprising. This would also suggest that the true viscosity of the wet THF solutions were in excess of 1.3 mPa·s, corresponding to a water content of 70% or greater, which is improbable as solutions were sealed in scintillation vials and had limited time to absorb water from the atmosphere. Nevertheless, the viscosity does not have an impact on the excimer enhancement, and in all three cases, extrapolates to an intercept of zero.

Table 3 E/M ratios and their concentration dependence for directly excited and upconverted solutions of pyrene.

		Slope		
Solvent	η (mPa·s)	Upconverted	Direct Excitation	Factor
DCM	0.413 [37]	2010 ± 40	1000 ± 10	2.02 ± 0.02
ODCB	1.324 [37]	1670 ± 60	808 ± 7	2.07 ± 0.04
THF	≥ 0.456 [37]	1120 ± 60	510 ± 11	2.18 ± 0.06

At both extremes of solvent viscosity, there does not appear to be any pre-formation of excimer within the pulse duration, nor do the E/M trends suggest any non-zero E/M ratio at the infinitesimal limit. In the 1 ms time windows used for the experiment, the temporal resolution is only 2 μs and given that the excimer lifetime is on the order of nanoseconds, it is likely that this formation is faster than the instrument's resolution, causing the monomer and excimer to appear simultaneously (see **Figure 3.5**). This does not, however, explain the limited excimer in very dilute, upconverted solutions. If the encounter radius for TTA was instead on the order of 1 nm, then the annihilation products would be free to diffuse through the solution where the locally increased concentration would still benefit excimer formation but not exclusively form the excimer. There are surprisingly few studies that investigate the kinetics of excimer formation following TTA/SF, with conflicting conclusions on the role that the excimer plays[26, 27]. Without commenting on relative efficiencies of TTA or excimer fluorescence, it is evident through this work that TTA must not operate exclusively through a DET type interaction involving a charge transfer intermediate and other mechanisms must be at play. Thus, efforts to stabilize the excimer and charge-transfer states to improve TTA might be a fruitless endeavor and the intermolecular spacing of the annihilator may not be so critical once it approaches the nanometer limit. Still, functionalization of the annihilator to prevent loss to the excimer remains an avenue to improve solid-state, light harvesting layers based on these sensitized, upconverting materials.

3.3 Conclusion

Through time-resolved photoluminescence, directly excited and sensitized solutions of pyrene are investigated in THF, DCM, and ODCB. In all three solvents, the E/M is enhanced and demonstrates a twofold increase in concentration dependence after TTA. At the infinitely dilute limit, E/M extrapolates to zero in all systems, suggesting that the excimer is not pre-formed through TTA and consequently does not involve a charge-transfer intermediate. Although there is presently no explanation for the twofold increase in the E/M for pyrene after upconversion, the evidence pointing to a long-range mechanism for TTA merits further exploration. In the solid state, where molecular orientation and diffusion can be highly constrained, it may be possible to further investigate this phenomenon. However, sensitization for upconversion in the solid state can be difficult to achieve and is typically performed in elastomers or gels[44]. If phase separation can be avoided, co-deposited films of sensitizers and annihilators may provide a useful analog to this experiment and provide further insight to the photophysical limitations of TTA.

3.4 References

(1) Parker, C. A.; Bowen, E. J. Sensitized P-type delayed fluorescence. *Proceedings of the Royal Society of London. Series A. Mathematical and Physical Sciences* **1963**, *276* (1364), 125-135. DOI: doi:10.1098/rspa.1963.0197.

(2) Sternlicht, H.; Nieman, G. C.; Robinson, G. W. Triplet—Triplet Annihilation and Delayed Fluorescence in Molecular Aggregates. *The Journal of Chemical Physics* **1963**, *38* (6), 1326-1335. DOI: 10.1063/1.1733853.

(3) Parker, C. A.; Hatchard, C. G.; Joyce, T. A. Selective and Mutual Sensitization of Delayed Fluorescence. *Nature* **1965**, *205* (4978), 1282-1284. DOI: 10.1038/2051282a0.

(4) Parker, C. A.; Joyce, T. A. Determination of Triplet Formation Efficiencies by Measurement of Sensitized Delayed Fluorescence. *T Faraday Soc* **1966**, *62* (526p), 2785-&. DOI: DOI 10.1039/tf9666202785.

(5) Zhao, W.; Castellano, F. N. Upconverted Emission from Pyrene and Di-tert-butylpyrene Using Ir(ppy)3 as Triplet Sensitizer. *The Journal of Physical Chemistry A* **2006**, *110* (40), 11440-11445. DOI: 10.1021/jp064261s.

(6) Ye, C.; Zhou, L.; Wang, X.; Liang, Z. Photon upconversion: from two-photon absorption (TPA) to triplet–triplet annihilation (TTA). *Physical Chemistry Chemical Physics* **2016**, *18* (16), 10818-10835, 10.1039/C5CP07296D. DOI: 10.1039/C5CP07296D.

(7) Huang, Z.; Li, X.; Mahboub, M.; Hanson, K. M.; Nichols, V. M.; Le, H.; Tang, M. L.; Bardeen, C. J. Hybrid Molecule–Nanocrystal Photon Upconversion Across the Visible and Near-Infrared. *Nano Letters* **2015**, *15* (8), 5552-5557. DOI: 10.1021/acs.nanolett.5b02130.

(8) Mongin, C.; Garakyaraghi, S.; Razgoniaeva, N.; Zamkov, M.; Castellano, F. N. Direct observation of triplet energy transfer from semiconductor nanocrystals. *Science* **2016**, *351* (6271), 369-372. DOI: doi:10.1126/science.aad6378.

(9) Jha, K. K.; Prabhakaran, A.; Burke, C. S.; Schulze, M.; Schubert, U. S.; Keyes, T. E.; Jäger, M.; Ivanšić, B. D. Triplet–Triplet Annihilation Upconversion by Polymeric Sensitizers. *The Journal of Physical Chemistry C* **2022**, *126* (8), 4057-4066. DOI: 10.1021/acs.jpcc.1c09897.

(10) Limberg, D. K.; Kang, J.-H.; Hayward, R. C. Triplet–Triplet Annihilation Photopolymerization for High-Resolution 3D Printing. *J Am Chem Soc* **2022**, *144* (12), 5226-5232. DOI: 10.1021/jacs.1c11022.

(11) Richards, B. S. Enhancing the performance of silicon solar cells via the application of passive luminescence conversion layers. *Solar Energy Materials and Solar Cells* **2006**, *90* (15), 2329-2337. DOI: https://doi.org/10.1016/j.solmat.2006.03.035.

(12) Yang, Z.-S.; Ning, Y.; Yin, H.-Y.; Zhang, J.-L. Lutetium(iii) porphyrinoids as effective triplet photosensitizers for photon upconversion based on triplet–triplet annihilation (TTA). *Inorganic Chemistry Frontiers* **2018**, *5* (9), 2291-2299, 10.1039/C8QI00477C. DOI: 10.1039/C8QI00477C.

(13) Di, D.; Yang, L.; Richter, J. M.; Meraldi, L.; Altamimi, R. M.; Alyamani, A. Y.; Credgington, D.; Musselman, K. P.; MacManus-Driscoll, J. L.; Friend, R. H. Efficient Triplet Exciton Fusion in Molecularly Doped Polymer Light-Emitting Diodes. *Advanced Materials* **2017**, *29* (13), 1605987. DOI: https://doi.org/10.1002/adma.201605987.

(14) Chen, C.-H.; Tierce, N. T.; Leung, M.-k.; Chiu, T.-L.; Lin, C.-F.; Bardeen, C. J.; Lee, J.-H. Efficient Triplet–Triplet Annihilation Upconversion in an Electroluminescence Device with a Fluorescent Sensitizer and a Triplet-Diffusion Singlet-Blocking Layer. *Advanced Materials* **2018**, *30* (50), 1804850. DOI: https://doi.org/10.1002/adma.201804850.

(15) Chen, S.; Weitemier, A. Z.; Zeng, X.; He, L.; Wang, X.; Tao, Y.; Huang, A. J. Y.; Hashimotodani, Y.; Kano, M.; Iwasaki, H.; et al. Near-infrared deep brain stimulation via upconversion nanoparticle-mediated optogenetics. *Science* **2018**, *359* (6376), 679-684. DOI: doi:10.1126/science.aaq1144.

(16) Zhang, L.; van Eersel, H.; Bobbert, P. A.; Coehoorn, R. Clarifying the mechanism of triplet–triplet annihilation in phosphorescent organic host–guest systems: A combined experimental and simulation study. *Chemical Physics Letters* **2016**, *652*, 142-147. DOI: https://doi.org/10.1016/j.cplett.2016.04.043.

(17) Zimmerman, P. M.; Bell, F.; Casanova, D.; Head-Gordon, M. Mechanism for Singlet Fission in Pentacene and Tetracene: From Single Exciton to Two Triplets. *J Am Chem Soc* **2011**, *133* (49), 19944-19952. DOI: 10.1021/ja208431r.

(18) Piland, G. B.; Burdett, J. J.; Dillon, R. J.; Bardeen, C. J. Singlet Fission: From Coherences to Kinetics. *J Phys Chem Lett* **2014**, *5* (13), 2312-2319. DOI: 10.1021/jz500676c.

(19) Trinh, M. T.; Pinkard, A.; Pun, A. B.; Sanders, S. N.; Kumarasamy, E.; Sfeir, M. Y.; Campos, L. M.; Roy, X.; Zhu, X.-Y. Distinct properties of the triplet pair state from singlet fission. *Sci Adv* **2017**, *3* (7), e1700241. DOI: doi:10.1126/sciadv.1700241.

(20) Wan, Y.; Guo, Z.; Zhu, T.; Yan, S.; Johnson, J.; Huang, L. Cooperative singlet and triplet exciton transport in tetracene crystals visualized by ultrafast microscopy. *Nature Chemistry* **2015**, *7* (10), 785-792. DOI: 10.1038/nchem.2348.

(21) Sanders, S. N.; Pun, A. B.; Parenti, K. R.; Kumarasamy, E.; Yablon, L. M.; Sfeir, M. Y.; Campos, L. M. Understanding the Bound Triplet-Pair State in Singlet Fission. *Chem* **2019**, *5* (8), 1988-2005. DOI: https://doi.org/10.1016/j.chempr.2019.05.012.

(22) Bossanyi, D. G.; Matthiesen, M.; Wang, S.; Smith, J. A.; Kilbride, R. C.; Shipp, J. D.; Chekulaev, D.; Holland, E.; Anthony, J. E.; Zaumseil, J.; et al. Emissive spin-0 triplet-pairs are a direct product of triplet–triplet annihilation in pentacene single crystals and anthradithiophene films. *Nature Chemistry* **2021**, *13* (2), 163-171. DOI: 10.1038/s41557-020-00593-y.

(23) Cruz, C. D.; Chronister, E. L.; Bardeen, C. J. Using temperature dependent fluorescence to evaluate singlet fission pathways in tetracene single crystals. *The Journal of Chemical Physics* **2020**, *153* (23), 234504. DOI: 10.1063/5.0031458.

(24) Birks, J. B.; Kazzaz, A. A.; Edwards, S. F. Excimer fluorescence XII. The pyrene crystal excimer interaction potential. *Proceedings of the Royal Society of London. Series A. Mathematical and Physical Sciences* **1968**, *304* (1478), 291-301. DOI: doi:10.1098/rspa.1968.0087.

(25) Birks, J. B. Excimers. *Reports on Progress in Physics* **1975**, *38* (8), 903-974. DOI: 10.1088/0034-4885/38/8/001.

(26) Dover, C. B.; Gallaher, J. K.; Frazer, L.; Tapping, P. C.; Petty, A. J.; Crossley, M. J.; Anthony, J. E.; Kee, T. W.; Schmidt, T. W. Endothermic singlet fission is hindered by excimer formation. *Nature Chemistry* **2018**, *10* (3), 305-310. DOI: 10.1038/nchem.2926.

(27) Ye, C.; Gray, V.; Mårtensson, J.; Börjesson, K. Annihilation Versus Excimer Formation by the Triplet Pair in Triplet–Triplet Annihilation Photon Upconversion. *J Am Chem Soc* **2019**, *141* (24), 9578-9584. DOI: 10.1021/jacs.9b02302.

(28) Stern, H. L.; Musser, A. J.; Gelinas, S.; Parkinson, P.; Herz, L. M.; Bruzek, M. J.; Anthony, J.; Friend, R. H.; Walker, B. J. Identification of a triplet pair intermediate in singlet exciton fission in solution. *Proceedings of the National Academy of Sciences* **2015**, *112* (25), 7656-7661. DOI: doi:10.1073/pnas.1503471112.

(29) Hausch, J.; Berges, A. J.; Zeiser, C.; Rammler, T.; Morlok, A.; Bredehöft, J.; Hammer, S.; Pflaum, J.; Bardeen, C. J.; Broch, K. Distinguishing between Triplet-Pair State and Excimer Emission in Singlet Fission Chromophores Using Mixed Thin Films. *The Journal of Physical Chemistry C* **2022**, *126* (15), 6686-6693. DOI: 10.1021/acs.jpcc.1c09297.

(30) Bohne, C.; Abuin, E.; Scaiano, J. Characterization of the triplet-triplet annihilation process of pyrene and several derivatives under laser excitation. *J Am Chem Soc* **1990**, *112* (11), 4226-4231.

(31) MacDonald, B. C.; Lvin, S. J.; Patterson, H. Correction of fluorescence inner filter effects and the partitioning of pyrene to dissolved organic carbon. *Analytica Chimica Acta* **1997**, *338* (1), 155-162. DOI: https://doi.org/10.1016/S0003-2670(96)00306-6.

(32) Hanlon, A. D.; Milosavljevic, B. H. Appropriate excitation wavelength removes obfuscations from pyrene excimer kinetics and mechanism studies. *Photochemical & Photobiological Sciences* **2013**, *12* (5), 787-797, 10.1039/C2PP25307K. DOI: 10.1039/C2PP25307K.

(33) Zhang, Y.; Forrest, S. R. Triplet diffusion leads to triplet–triplet annihilation in organic phosphorescent emitters. *Chemical Physics Letters* **2013**, *590*, 106-110. DOI: https://doi.org/10.1016/j.cplett.2013.10.048.

(34) Zhang, C.; Zhou, H.-P.; Liao, L.-Y.; Feng, W.; Sun, W.; Li, Z.-X.; Xu, C.-H.; Fang, C.-J.; Sun, L.-D.; Zhang, Y.-W.; et al. Luminescence Modulation of Ordered Upconversion Nanopatterns by a Photochromic Diarylethene: Rewritable Optical Storage with Nondestructive Readout. *Advanced Materials* **2010**, *22* (5), 633-637. DOI: https://doi.org/10.1002/adma.200901722.

(35) Lee, H.-L.; Lee, M.-S.; Park, H.; Han, W.-S.; Kim, J.-H. Visible-to-UV triplet-triplet annihilation upconversion from a thermally activated delayed fluorescence/pyrene pair in an air-saturated solution. *Korean Journal of Chemical Engineering* **2019**, *36* (11), 1791-1798. DOI: 10.1007/s11814-019-0355-2.

(36) Holzer, W.; Penzkofer, A.; Tsuboi, T. Absorption and emission spectroscopic characterization of Ir(ppy)3. *Chemical Physics* **2005**, *308* (1), 93-102. DOI: https://doi.org/10.1016/j.chemphys.2004.07.051.

(37) Rumble, J. R.; Bruno, T. J.; Doa, M. J. *CRC handbook of chemistry and physics : a ready-reference book of chemical and physical data*; CRC Press/Taylor & Francis Group, 2021.

(38) Birks, J. B.; Dyson, D. J.; Munro, I. H.; Flowers, B. H. Excimer fluorescence II. Lifetime studies of pyrene solutions. *Proceedings of the Royal Society of London. Series A. Mathematical and Physical Sciences* **1963**, *275* (1363), 575-588. DOI: doi:10.1098/rspa.1963.0187.

(39) Nayak, J. N.; Aralaguppi, M. I.; Kumar Naidu, B. V.; Aminabhavi, T. M. Thermodynamic Properties of Water + Tetrahydrofuran and Water + 1,4-Dioxane Mixtures at (303.15, 313.15, and 323.15) K. *Journal of Chemical & Engineering Data* **2004**, *49* (3), 468-474. DOI: 10.1021/je030196t.

(40) Smoluchowski, M. Mathematical Theory of the Kinetics of the Coagulation of Colloidal Solutions. *Zeitschrift für Physikalische Chemie* **1917**, *19*, 129-135.

(41) E. Hoffman, R.; Shabtai, E.; Rabinovitz, M.; S. Iyer, V.; Müllen, K.; K. Rai, A.; Bayrd, E.; T. Scott, L. Self-diffusion measurements of polycyclic aromatic hydrocarbon alkali metal salts. *Journal of the Chemical Society, Perkin Transactions 2* **1998**, (7), 1659-1664, 10.1039/A800382C. DOI: 10.1039/A800382C.

(42) Safi, A.; Nicolas, C.; Neau, E.; Chevalier, J.-L. Measurement and Correlation of Diffusion Coefficients of Aromatic Compounds at Infinite Dilution in Alkane and Cycloalkane Solvents. *Journal of Chemical & Engineering Data* **2007**, *52* (3), 977-981. DOI: 10.1021/je6005604.

(43) Miyasaka, H.; Masuhara, H.; Mataga, N. Picosecond absorption spectra and relaxation processes of the excited singlet state of pyrene in solution. *Laser chemistry* **1983**, *1* (5), 357-386.

(44) Gray, V.; Moth-Poulsen, K.; Albinsson, B.; Abrahamsson, M. Towards efficient solid-state triplet–triplet annihilation based photon upconversion: Supramolecular, macromolecular and self-assembled systems. *Coordination Chemistry Reviews* **2018**, *362*, 54-71.

Chapter 4. Distinguishing between Triplet-Pair State and Excimer Emission in Singlet Fission Chromophores Using Mixed Thin Films

Since the excimer is not directly formed by TTA in pyrene, then the encounter distance required for up conversion must be incompatible with the excimer formation and thus renders it as a parallel decay channel for the singlet instead of mediating photon upconversion. Similarly, in photon down-conversion films, spectral evidence of the correlated triplet pair intermediate of singlet fission may be observed with Herzberg-Teller coupling. However, it lies energetically close to the red-shifted luminescence (RSL) typically caused by excimers in the solid state. This chapter identifies the source of RSL in blended films of ADT, TET, and 6PH and establishes the excimer as a relaxation pathway occurring in parallel to SF, analogous to TTA system studied in the previous chapter.

4.1 Introduction

In the optimization of organic optoelectronic devices, a crucial part is understanding the mechanism and contribution of loss channels. To obtain deeper insight into the involved processes, photoluminescence (PL) spectroscopy is a well-suited method, as it not only allows the detection of nonradiative channels via quenching but also is sensitive to specific radiative channels such as the population of trap states or excimer formation, both of which can be readily identified by spectroscopic signatures red-shifted from the exciton emission[1, 2]. Similar signatures are of particular importance for a specific class of organic semiconductors, namely singlet fission (SF) materials, as they can give insights into the details of this multistep, technologically relevant[3], process. SF describes the spin-allowed fission of a singlet exciton into two triplet excitons via an electronically coupled triplet-

pair state (^{1}(TT)) of singlet character[4] and has been successfully studied *inter alia*[5-7] via PL spectroscopy to elucidate the nature of the triplet-pair state intermediate and the related pathways of triplet-pair formation and triplet separation[8-16].

However, one complication that arises in the investigation of SF materials by PL spectroscopy is the fact that the intermediate ^{1}(TT) state is a dark state[17] that becomes only emissive via Herzberg–Teller coupling[13, 15, 18-20]. The resulting red shift of the corresponding emission compared to the energy of the ^{1}(TT) state leads to an overlap of its spectral signature with other contributions at low photon energies such as excimers[2, 11, 12, 14, 21-26] or trap-state emission[1, 13-15]. This poses the experimental challenge to disentangle the various contributions leading to emission features at low photon energies (in the following referred to as red-shifted luminescence features (RSL)) and to clarify whether the related states mediate SF[10, 12, 16, 21, 27-29] or constitute a loss channel[11, 14, 15, 22, 23, 25, 30-34]. This question directly relates to an ongoing debate in the literature, which concerns the role of excimer formation in the SF process[11, 12, 14, 21-26, 31, 34]. Excimers as a competing channel for SF have been observed experimentally in tetracene (TET)[11, 14, 34, 35] and antradithiophene (ADT) derivatives[20, 30], but have also been proposed as an intermediate state for SF[10, 27, 36, 37].

The challenges preventing a general elucidation of the nature of the many possible states which can cause RSL (X_{RSL}) in thin films of SF materials arise from the above-mentioned ambiguity in the assignment of spectral signatures[10, 13, 16, 20, 34] (10,13,16,20,34) and the lack of a tunable parameter that affects the energetic position of trap state emission, ^{1}(TT) state emission, and excimer emission differently. Here, we address this open question

in ADT, a chromophore whose derivatives have been reported to exhibit both SF and pronounced RSL[20]. ADT is codeposited with two spacer compounds to continuously change the intermolecular interactions, the number of nearest neighbors, and the polarizability of the local molecular environment. The spacer molecules TET and [6]-phenacene (6PH) are chosen to have singlet energies greater than that of ADT, making energy transfer from ADT to the spacers unlikely. The resulting changes in the dynamics of the different decay channels are probed by time-resolved PL spectroscopy (TRPL). Comparing the photoluminescence behavior of ADT in blends with spacer molecules of high and low polarizability[38], TET and 6PH (see **Figure 4.1a**), respectively, with ADT in solution, allows us, first, to confirm the occurrence of SF in ADT and, second, to distinguish between spectral contributions of the ^{1}(TT) state, trap states and excimers. We identify the latter as a parallel pathway to SF in ADT, allowing for a refinement of current models on the role of X_{RSL} debated in the literature[13, 14].

4.2 Results and Discussion

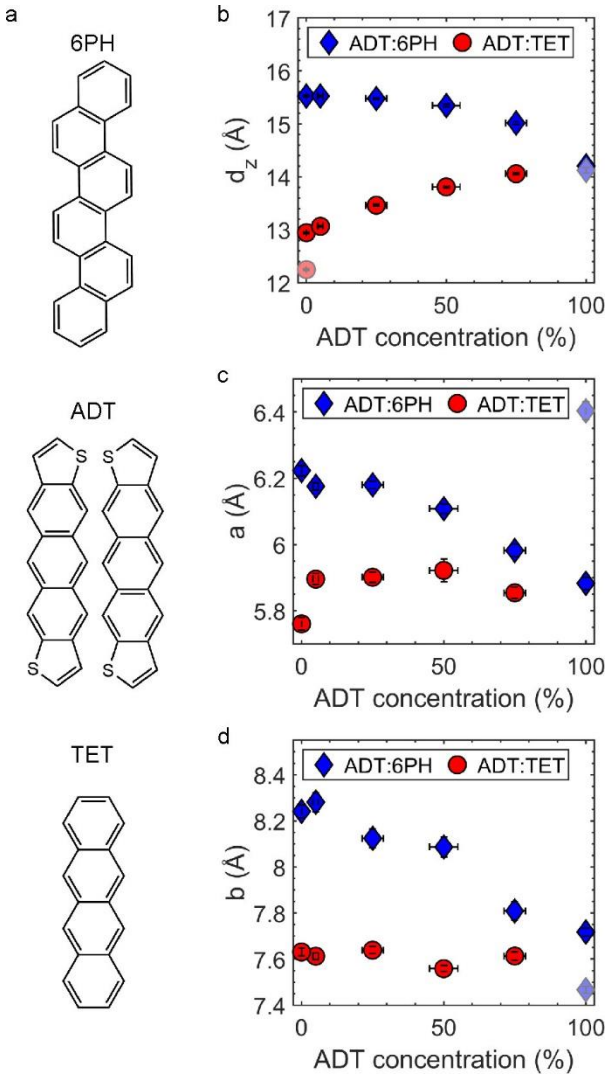

Figure 4.1 (a) Chemical structure of the investigated molecules. For ADT, the two isomers present in our samples are shown, see Supporting Information for details. **(b)** Out-of-plane lattice spacing and **(c,d)** in-plane unit cell parameters **(c)** a and **(d)** b, determined by X-ray diffraction. The faded data points indicate the unit cell parameters determined for the second polymorph of ADT or TET. Note that the in-plane unit cell parameters do not differ significantly between the two polymorphs of TET.

The ADT used here contains two different isomers, anti-ADT and syn-ADT (see above), with a mixing ratio of 1:1, expected from the synthesis pathway[39]. Purification of ADT in relevant quantities by HPLC or zone refinement is challenging inter alia due to its

poor solubility[40, 41]. However, both isomers show very similar single crystal unit cells[40], which makes it unlikely that the mixture of both isomers creates a much different structure, which is in agreement with our X-ray diffraction data. Although the chemical structures of the two isomers have different symmetries, DFT calculations yielded very similar $S_1 \leftarrow S_0$ transition energies and similar orientations of the corresponding transition dipole moment (TDM) compared to the long axis of the anthracene core of the molecule for both isomers (**Table 4**), suggesting a very similar photophysical behavior in the S_1 state of both isomers. The differences between the isomers for transitions to higher states (S_2-S_6) are expected to play a minor role in the photophysics at hand, as the processes discussed here are expected to take place after the molecular entity has already relaxed to the S_1 state.

Table 4 Energy, oscillator strength and TDM orientation for the energetically lowest six allowed optical transition. DFT calculations made after geometry optimization using the B3-LYP exchange correlation function and ref-TZVP as a basis function[a]. The given angle is the angle between the TDM of the respective transition and the long axis of the anthracene core of the molecule. For all transitions the TDM is in the molecular plane.

Molecule	Electronic transition	Energy	Osc. Strength	TDM orientation[a]
anti-ADT	$S_1 \leftarrow S_0$	2.449 eV	0.0641	58°
anti-ADT	$S_2 \leftarrow S_0$	3.372 eV	0	—
anti-ADT	$S_3 \leftarrow S_0$	3.411 eV	0.00093	72°
anti-ADT	$S_4 \leftarrow S_0$	3.796 eV	0	—
anti-ADT	$S_5 \leftarrow S_0$	4.293 eV	0.458	4°
anti-ADT	$S_6 \leftarrow S_0$	4.342 eV	1.849	1°
syn-ADT	$S_1 \leftarrow S_0$	2.457 eV	0.0436	90°
syn-ADT	$S_2 \leftarrow S_0$	3.310 eV	0.00510	0°
syn-ADT	$S_3 \leftarrow S_0$	3.418 eV	0.0118	0°
syn-ADT	$S_4 \leftarrow S_0$	3.888 eV	0.2789	0°
syn-ADT	$S_5 \leftarrow S_0$	4.288 eV	0.00211	87°
syn-ADT	$S_6 \leftarrow S_0$	4.424 eV	2.1697	0°

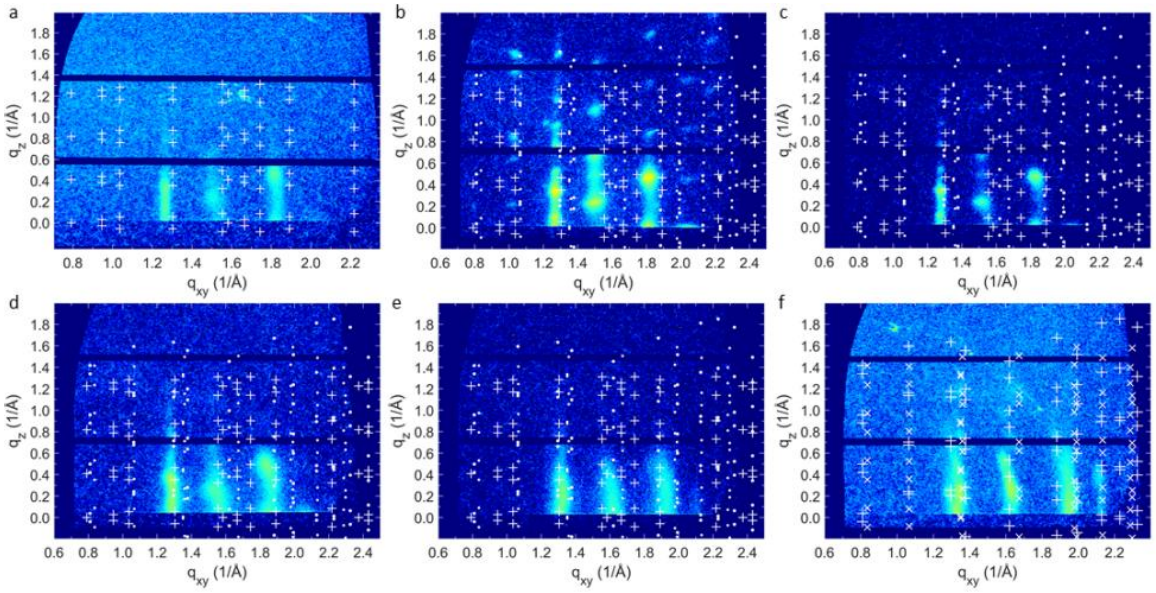

Figure 4.2 GIWAXS maps of ADT:6PH blends with 0 % **(a)**, 5 % **(b)**, 25 % **(c)**, 50 % **(d)**, 75 % **(e)** and 100 % **(f)** ADT. The circles (crosses) denote calculated Bragg-peak positions for anti-ADT and syn-ADT (6PH) based on literature values. In the neat films only the respective positions are given.

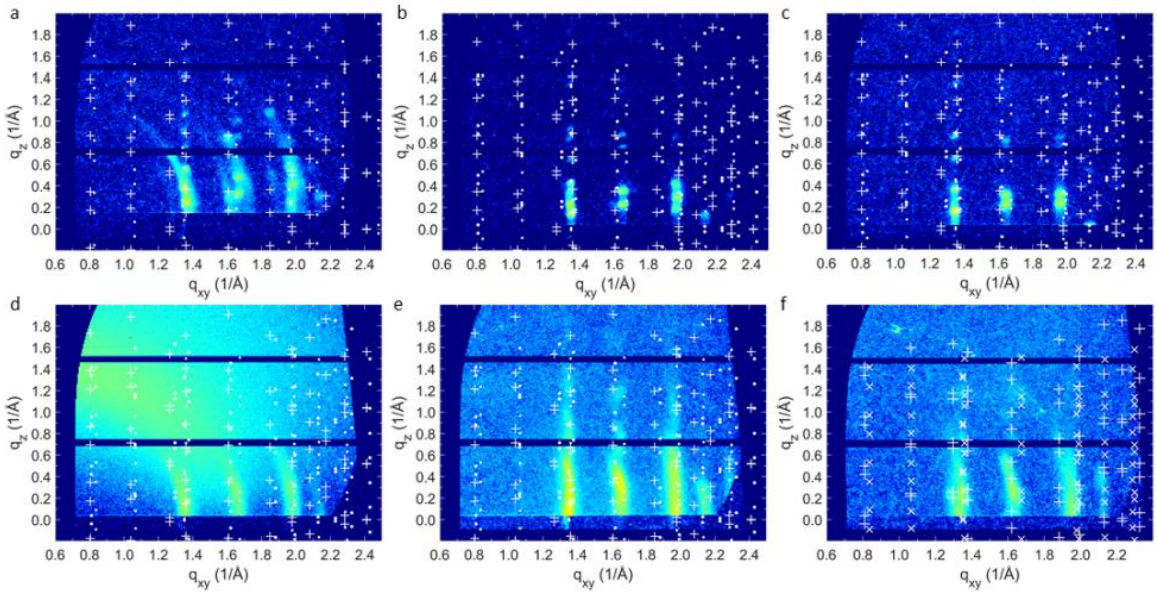

Figure 4.3 GIWAXS maps of ADT:TET blends with 0 % **(a)**, 5 % **(b)**, 25 % **(c)**, 50 % **(d)**, 75 % **(e)** and 100 % **(f)** ADT. The circles (crosses) denote calculated Bragg-peak positions for anti-ADT and syn-ADT (TET) based on literature values. In the neat films only the respective positions are given.

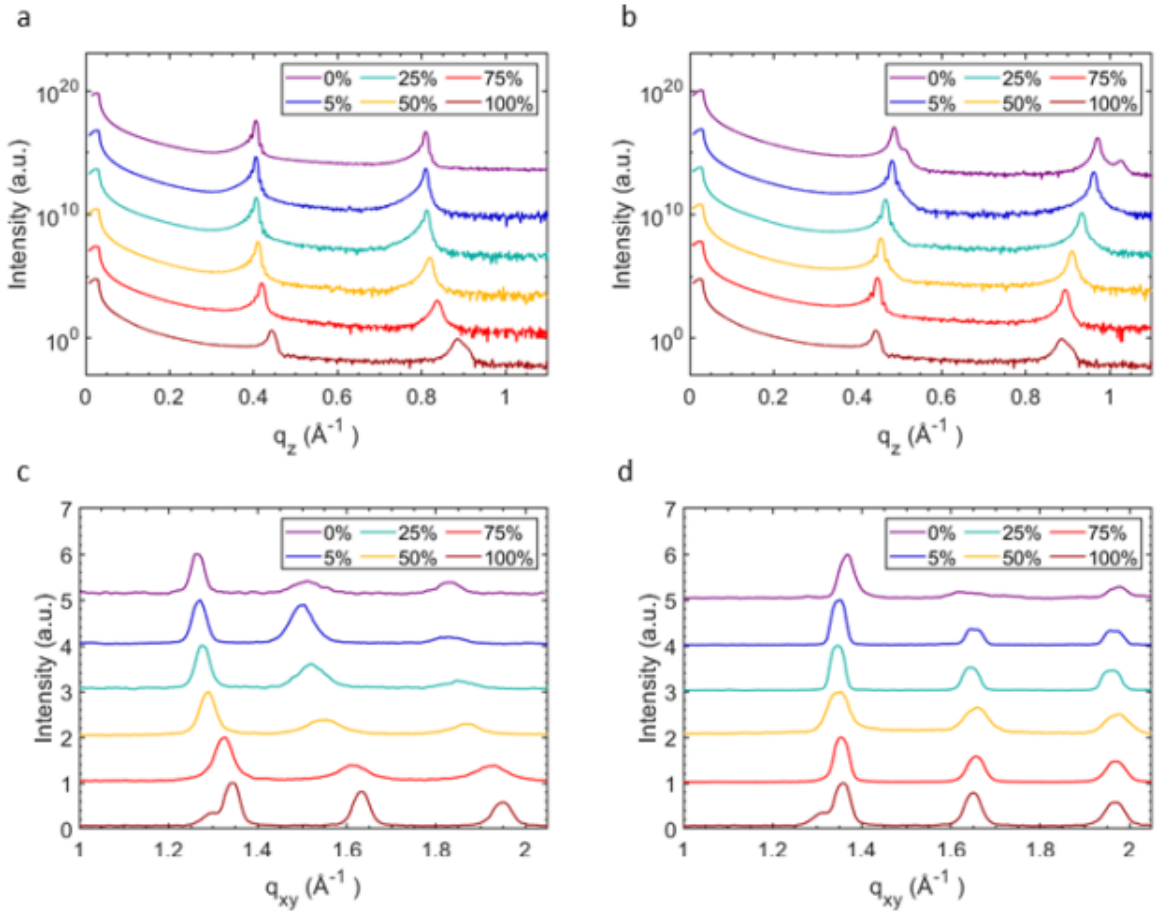

Figure 4.4 (a,b) XRR scans and **(c,d)** grazing incidence X-ray diffraction (GID) scans extracted by integrating the GIWAXS data in Figure 4.2 and 4.3 over q_z in a range of 0.1 – 0.3 Å^{-1} of ADT:6PH **(a,c)** and ADT:TET **(b,d)** blends. Data are offset for clarity.

The XRR-data shown in **Figure 4.4a-b** show a continuous shift of the Bragg peak position with ADT concentration between the positions of the neat films. The same trend can be seen for the position of the in-plane Bragg peaks in ADT:6PH mixtures (**Figure 4.4c**), while for ADT:TET mixtures the changes in the in-plane structure are too small between the mixtures to find a clear trend (**Figure 4.4d**). The latter can be rationalized by

the fact that neat ADT and neat TET have very similar in-plane unit cell parameters[40, 42]. We can conclude that the molecules in the neat films and in all the mixtures form a herringbone structure since the (1 0 0) and (0 1 0) peaks[40] are suppressed in the reciprocal space maps (**Figure 4.2** and **Figure 4.3**) and the GID line scans (**Figure 4.4c-d**) which is common for herringbone structures[43]. We extracted the unit cell parameters from the data in **Figure 4.4** by Gaussian fits assuming a monoclinic unit cell for the calculation of the in-plane lattice parameters and we find the above-discussed trend confirmed. From this we conclude that both mixed systems exhibit statistical intermixing, which means that a common lattice is formed in which the lattice sites are occupied statistically by molecules of either compound depending on the mixing ratio[43, 44]. This is further confirmed by the continuous shift of the position of the $S_0 \rightarrow S_1$ absorption peak in **Figure 4.5**. This shift is attributed to changes in the polarizability of the molecular environment due to the incorporation of spacer molecules (TET or 6PH)[44]. Since polarizability is a short-range effect, this shift also points towards statistical intermixing. Lastly, we note that for neat ADT and neat TET some of the Bragg peaks are doubletts and had to be fitted with two Gaussian functions, which results in two possible lattice parameters in **Figure 4.1**. The Bragg peak with a higher integrated intensity was taken as the reflection of the prevalent structure, while the lattice parameters calculated from the Bragg peaks with less integrated intensity are displayed in faded colors in **Figure 4.1**.

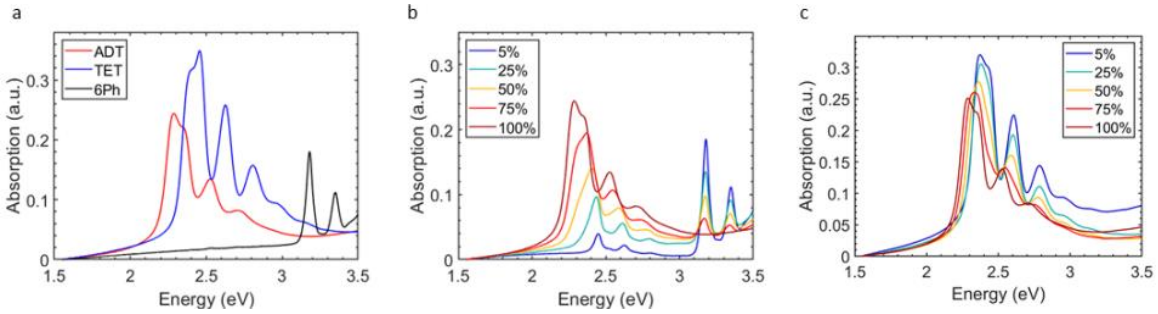

Figure 4.5 Absorption spectra of the neat films **(a)**, ADT:6PH blends **(b)** and ADT:TET blends **(c)**.

Since the two isomers of ADT are structurally and optically similar, we do not expect differences in the steric compatibility, the mixing behavior, or the intermolecular interactions of the two ADT isomers with the spacer molecules (TET and 6PH) studied here. Also, most previous studies on optical and electronic properties of ADT and its derivatives use a mixture of both isomers as well[13, 45-49]. (13,40−44) In the following we will thus refer to the isomerically mixed material as ADT. The structural properties of the two mixed systems (ADT:TET blends and ADT:6PH blends) are summarized in **Figure 4.1b-d**. There are clear differences in the dependence of the in-plane unit cell parameters a and b on the ADT concentration. While these parameters continuously increase with decreasing ADT concentration in blends with 6PH, they remain constant in blends of ADT with TET. This is consistent with statistical intermixing and with the fact that the neat ADT and TET films have comparable in-plane unit cell sizes, while it is clearly larger for neat 6PH (**Figure 4.1c-d**). Since the in-plane unit cell parameters describe the plane in which the molecular interactions are strongest[50], any changes in these parameters might affect the related intermolecular electronic coupling[51-53] and, consequently, the photophysics. However, by comparing two mixed systems with different trends, we can estimate the

impact of such structural changes on the PL spectra and the underlying excited state dynamics.

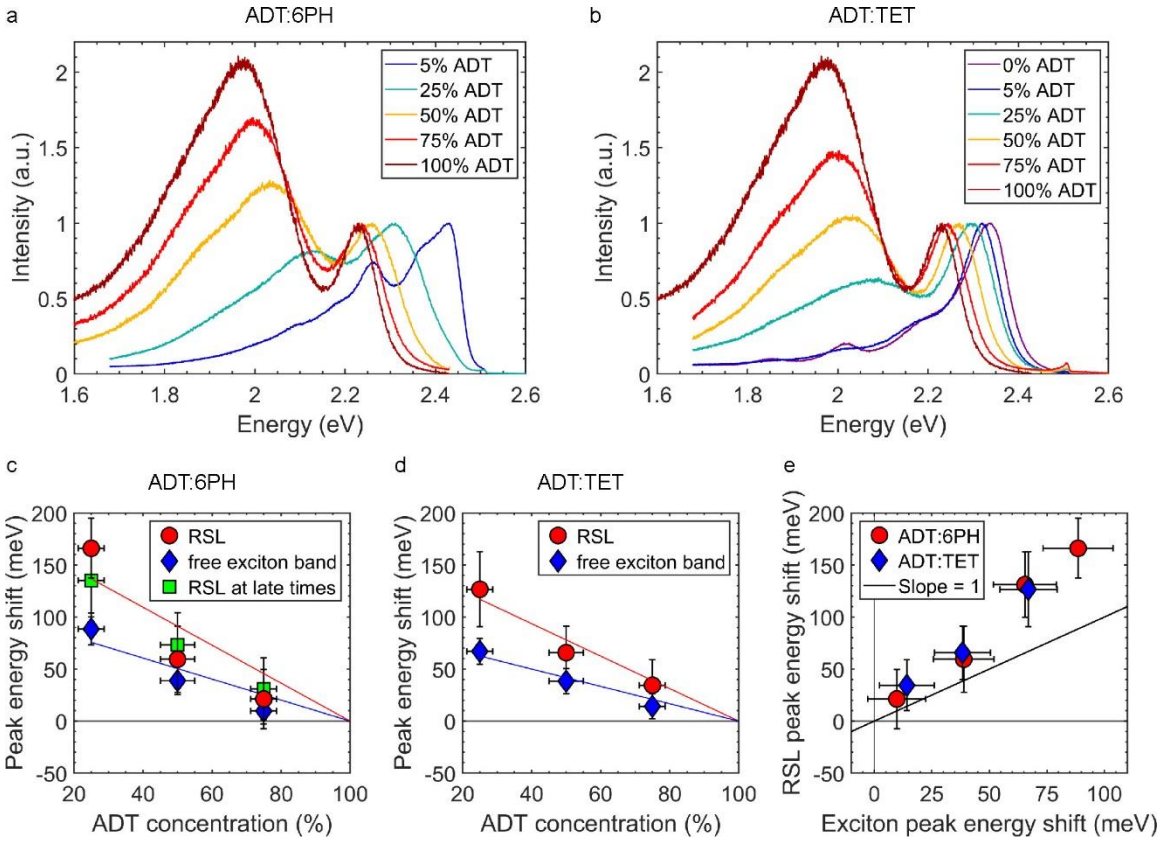

Figure 4.6 (a,b) Quasi-steady-state PL spectra of ADT:6PH **(a)** and ADT:TET blends **(b)** with different mixing ratios. The photon energy of the excitation was 2.54 eV. **(c,d)** Energetic shift of the RSL, the RSL at late times and the exciton peak position in ADT:6PH **(c)** and ADT:TET **(d)** blends compared to the respective positions for neat ADT. The red and blue lines are guide to the eye for the peak shift of the exciton (blue) and the RSL (red), respectively. **(e)** Energetic shift of the RSL against the shift of the free exciton emission for ADT:6PH and ADT:TET.

The steady-state PL spectra of the different samples are shown in **Figure 4.6**. The PL spectrum of neat ADT is dominated by two transitions, one at 2.21 eV, which we assign to emission of the free exciton based on the spectral shape and the small Stokes shift of 70 meV ($S_1 \leftarrow S_0$ in absorption at 2.28 eV from **Figure 4.5**). The second emission peak occurs

at 1.95 eV, red-shifted by ΔE = 260 meV compared to the first emission peak. This spacing is too large for a vibronic progression of the free exciton, which we would expect around ΔE = 150 meV based on the vibronic progression of the absorption spectrum (**Figure 4.5**), and we thus assign it to the before-mentioned RSL that has been observed also for other SF compounds[10, 11, 13, 14, 16, 20, 30].

Now considering the PL spectra of the blends, a first interesting result is the independence of the spectral shape on the codeposited compound and the dominant ADT contribution as can be seen in **Figure 4.6a,b**. The PL spectra of the ADT:6PH blend with 5 % ADT are dominated by emission from ADT molecules surrounded by only 6PH molecules and, thus, resemble the PL spectrum of ADT monomers. Due to their isolation, obviously, these ADT molecules are not capable of singlet fission or excimer formation. For the ADT:TET blend with 5 % ADT, however, different photophysics are observed. This is due to two factors. Firstly, in this blend TET is excited as well, which means that TET luminescence is expected to be observed. Secondly, the isolation of ADT molecules increases the energy of S_1, which allows for energy transfer from these isolated ADT molecules to TET. This energy transfer is competing with radiative decay of the exciton and therefore lowers the ADT luminescence intensity compared to that of the respective ADT:6PH blend.

In the following, we will restrict the discussion to blends with ADT concentrations above 5%. Comparing the positions of the two main features in neat ADT with their positions in the PL spectra of the blends (see **Figure 4.6c-d**), we observe a continuous shift to higher photon energies with decreasing ADT concentration in all cases, which can be

explained by changes in the polarizability of the local molecular environment in the blends compared to the neat film. The absolute value of the shift follows the optical band gap of the spacer molecules and the related polarizability[38], since the observed shift is larger in blends of ADT with the high band gap (low polarizability) spacer molecule 6PH compared to the low band gap (higher polarizability) spacer molecule TET. Further comparing the shift of the free exciton emission and the RSL for all blends, we find that the shift is more pronounced for the latter (see trendlines in **Figure 4.6c-d**), implying that X_{RSL} is more sensitive to changes in the polarizability of the environment than the free exciton. This increased sensitivity can be rationalized by a stronger charge transfer (CT) state admixture[52-54], which has been observed for excimers[31, 55] and gives us first insight into the nature of X_{RSL}. An additional noteworthy finding is the decrease of the intensity of the RSL relative to the free exciton emission with decreasing ADT concentration. For processes which strongly depend on interactions between neighboring molecules, like excimer formation or triplet-pair state formation, such an intensity decrease results from the replacement of nearest ADT neighbors by TET as well as 6PH[44]. Importantly, as the probability for a given number of ADT neighbors follows a binomial distribution[44] and is thus independent of the molecule (TET or 6PH) replacing ADT, this intensity decrease is identical in ADT blends with TET or 6PH. To summarize these first results, the coexistence of the RSL with emission of the free exciton makes these ADT based blends an ideal model system to investigate the origin of the RSL and its impact on SF using TRPL measurements.

Table 5 Time constants determined from exponential fits of the TRPL time traces

ADT concentration	0 %	5 %	25 %	50 %	75 %	100 %
ADT:TET exciton decay	50 ps	64 ps	47 ps	42 ps	32 ps	22 ps
ADT:6PH exciton decay		877 ps	113 ps	47 ps	38 ps	22 ps
ADT:RSL decay		1217 ps	1342 ps	1075 ps	949 ps	716 ps

Table 6 Spectral integration interval of the TRPL time traces. Each interval is centered around the luminescence peak position of the respective species and hence depends on the mixing ratio, the spacer molecule, and the excited state species of interest. All spectral intervals in the table are given in eV.

ADT conc.	0 %	5 %	25 %	50 %	75 %	100 %
ADT:TET exciton	2.26-2.39	2.26-2.39	2.26-2.39	2.23-2.35	2.21-2.34	2.16-2.28
ADT:6PH exciton		2.32-2.60	2.23-2.49	2.18-2.42	2.15-2.38	2.13-2.37
ADT:6PH RSL		2.09-2.32	2.02-2.23	1.97-2.17	1.94-2.14	1.93-2.12

Table 7 Optical bandgaps, determined by the energy of the lowest possible optical transition of the absorption spectrum, and HOMO and LUMO energies, ADT and 6PH calculated by DFT (B3-LYP/ref-TZVP), TET from Ref. 56.

Molecule	ADT	TET	6PH
Optical bangap	2.28 eV	2.39 eV	3.18 eV
HOMO	-5.0 eV	-4.9 eV	-5.7 eV
LUMO	-2.2 eV	-2.1 eV	-1.6 eV

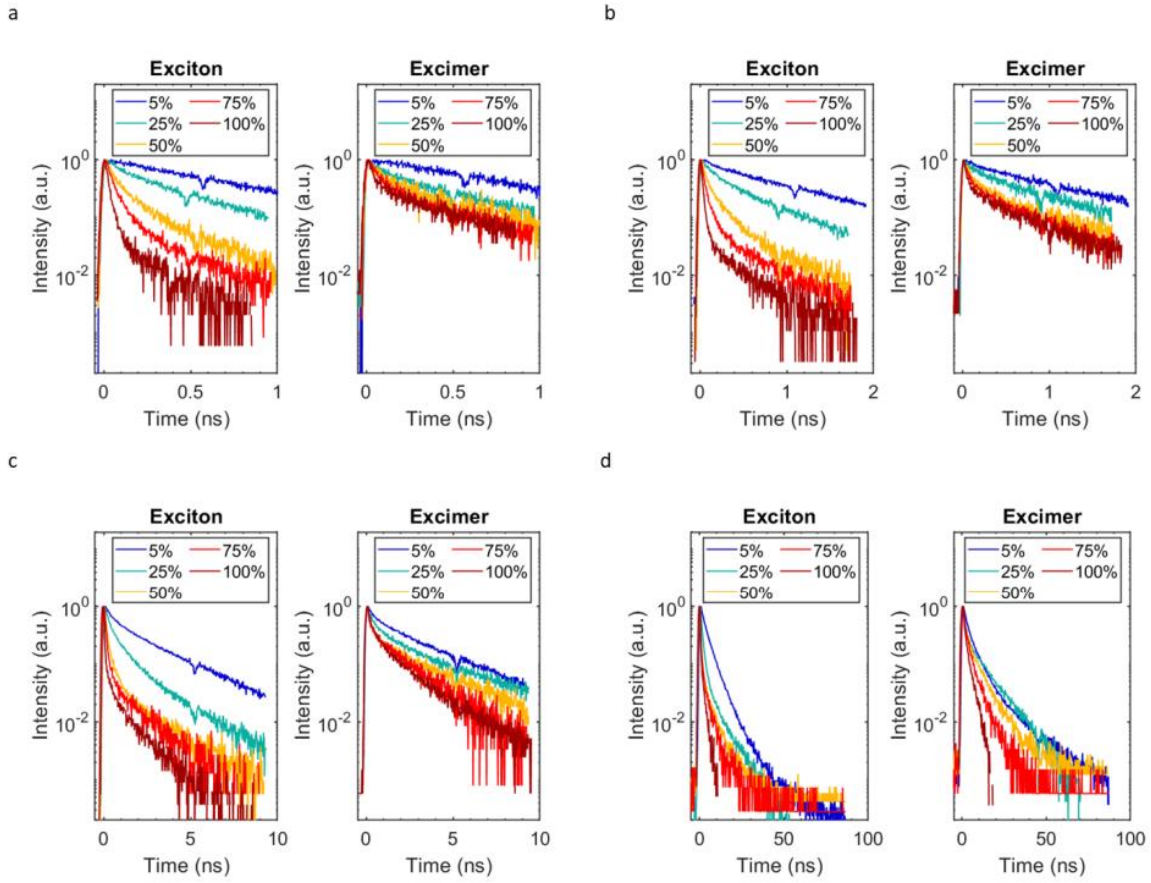

Figure 4.8 Time traces of the PL intensity decays of the exciton and the RSL for ADT:6PH blends of different mixing ratios. The dip in the data at half the time range of each respective measurement is an artifact of the setup.

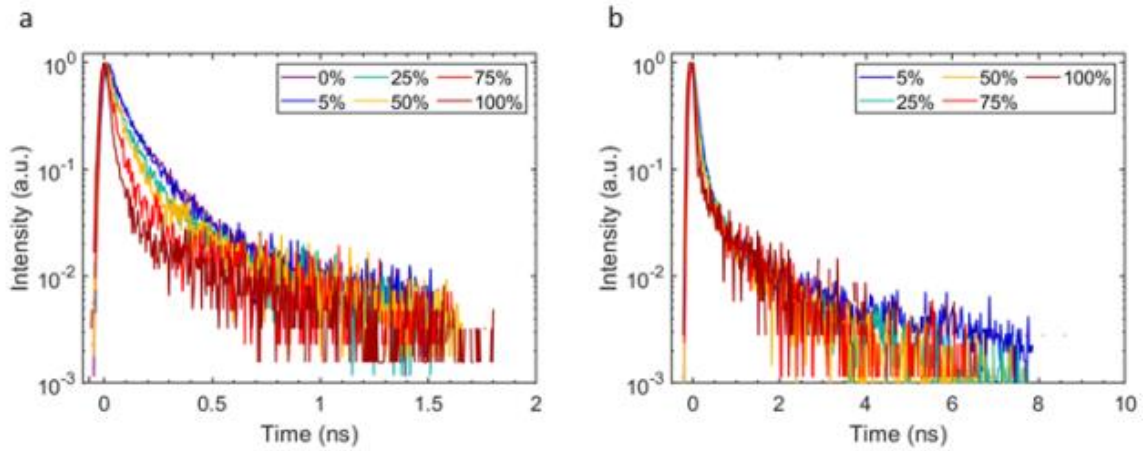

Figure 4.7 Time traces of the PL intensity decay for ADT:TET blends of different mixing ratios.

The optical bandgaps of ADT, TET[56], and 6PH are calculated and summarized in **Table 7**. Time traces extracted at the energetic position of the free exciton emission and the RSL are shown in **Figure 4.8** and**Figure 4.7** and have been analyzed by fitting to a biexponential decay (**Table 5**). In thin films the free exciton emission decays generally faster than the RSL and, in addition, exhibits a higher sensitivity to changes in the ADT concentration. The rates of the free exciton decay decrease linearly with decreasing ADT concentration independent of the spacer molecule (see **Figure 4.10a-b**). This, in combination with an increased decay rate of the free exciton emission of a neat ADT thin film compared to ADT in solution from **Figure 4.9a** gives insight into the photophysics of ADT. In solution, ADT exhibits a decay rate of 0.57 ns^{-1}, while in the polycrystalline solid state a new, much more rapid decay process with a rate of about 42 ns^{-1} appears. Furthermore, the linear dependence of this decay rate on the ADT concentration in blends demonstrates that two nearest neighbors are involved in this rapid decay and that the increase in lateral spacing with decreasing ADT concentration plays a minor role. On these time scales, SF is the most probable candidate for this system, also because SF has already been reported to occur in a variety of ADT derivatives[13, 20, 30]. Importantly, we can not only conclude that SF is the main decay path of the free exciton, but our results for ADT blends also allow us to elucidate its microscopic mechanism. The linear dependence of the SF rate on the chromophore concentration has been observed before for TET and referred to as the replacement effect[44, 57], indicating that SF occurs via incoherent population transfer from S_1 to ^{1}(TT). The deviation from this linear dependence found for TET blends with low ADT fractions can be explained by the similar band gaps of ADT and TET, which makes

an excitation of solely ADT impossible and can also enable an energy transfer from ADT to TET. Hence the excited state dynamics of TET have to be considered for these blends

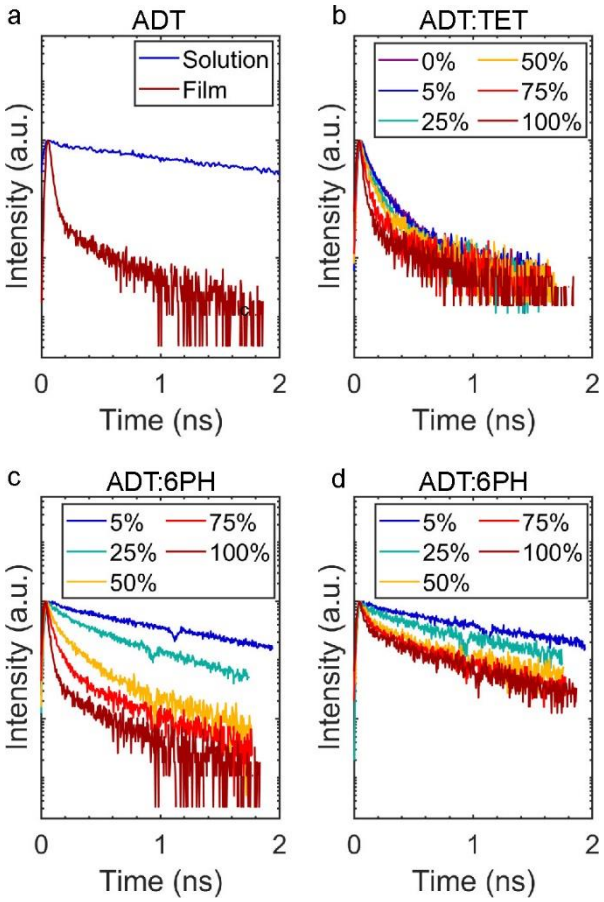

Figure 4.9 (a) Time traces of the singlet exciton emission of ADT in CHCl3 solution and in a neat ADT film. **(b,c)** Time traces of the free exciton emission in **(b)** ADT:TET and **(c)** ADT:6PH blends with different ADT concentrations, **(d)** time traces of the RSL in ADT:6PH blends with different ADT concentrations. ADT concentrations of the blends are given in molar % in the legend. The intensity is scaled logarithmically.

as well.

The ADT:TET mixtures are a prototypical system for heterofission, where the spontaneous fission of a singlet exciton leads to two triplets on chemically distinct molecules (here one triplet on ADT and one triplet on TET), since both SF chromophores have almost the same bandgap. Signs of heterofission are expected to be most pronounced

in the decay dynamics of the mixtures with 25 % ADT and 5 % ADT (**Figure 4.6b** and **Figure 4.9**), since there the PL signal has significant contributions from both, ADT, and TET. In these two mixtures there are two main relaxation paths for TET singlet excitons, namely TET SF and energy transfer to ADT and four decay paths for ADT singlet excitons, namely ADT SF, RSL state formation, fluorescence, and energy transfer to TET.

In the mixture with 5 % ADT, the decay paths of excitons on ADT and TET cannot be fully disentangled due to energy transfer between ADT and TET, but it is noteworthy that the time scale of the averaged singlet exciton decay is slower than expected from the replacement effect[44, 57] of TET alone, see **Figure 4.6b** in the main text. This indicates a significant contribution of long-lived singlets on ADT molecules isolated in a TET matrix and, thus, allows us to exclude heterofission of an ADT singlet into triplets on ADT and TET as a possible fast decay channel, which would lead to a fast quenching of long-lived emission. In contrast, in the 25 % ADT mixture a surprisingly high rate for SF is found compared to the expectation based on the replacement effect (**Figure 4.6**). This is probably caused by the coexistence of two comparably fast decay channels for TET singlets, one being TET SF and the other one being energy transfer to ADT followed by singlet homofission in ADT. We note that energy transfer from ADT to TET is unlikely here since the energy of S_1 of ADT is now lower than that of TET.

Since SF is mediated by states comparable to X_{RSL} in ADT derivates[13, 20], the dynamics of the RSL also give insight into the SF mechanism. The temporal evolution of the RSL intensity in **Figure 4.8** allows us to conclude that X_{RSL} is formed on a time scale faster than the instrument response (<10 ps) and, furthermore, that population transfer from the

exciton to X_{RSL} can be excluded as the major decay channel for the free exciton due to the lack of an increase in RSL intensity on the time scale of the free exciton emission decay. Lastly, the intensity decay of the RSL follows a similar trend with changing ADT concentration as that observed for the free exciton (**Table 5**), although less pronounced.

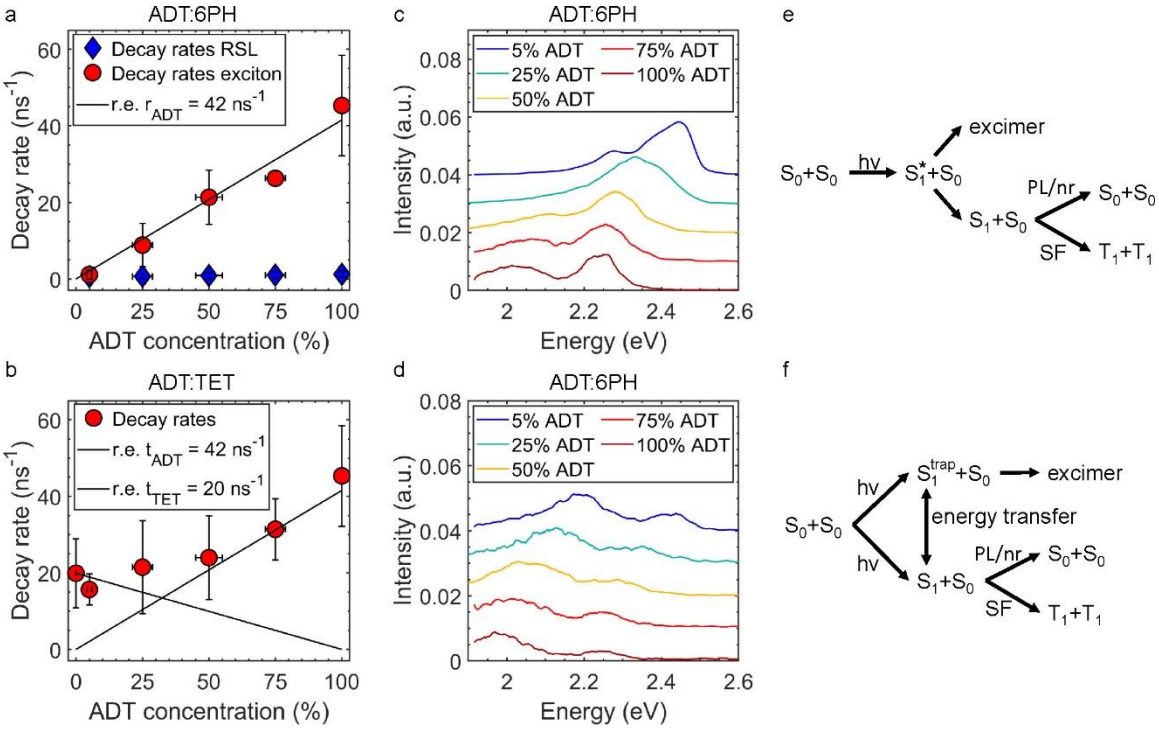

Figure 4.10 (a,b) Evolution of the SF rate and RSL decay rate of ADT:6PH **(a)** and ADT:TET **(b)** blends. For SF based on incoherent population transfer a linear behavior with changing ADT concentration is expected according to the replacement effect (r.e.) as sketched in the graphs. Note that the decay rate for 5% ADT in **(a)** might be dominated by the decay of excitons on isolated ADT molecules and that the decay rate for 100% ADT in **(a,b)** is close to the instrument resolution, which is 10 ps. **(c,d)** Time-integrated PL spectra of ADT:6PH blends in the time range **(c)** 0 to 2 ns and **(d)** >4 ns (100%, 75% ADT), >8 ns (50% ADT), >40 ns (25%, 5% ADT). Excitation at 400 nm, data noise filtered and vertically offset for clarity. **(e,f)** Sketches of possible decay mechanisms.

In order to shed further light on the decay dynamics, PL spectra of the different ADT:6PH blends have been extracted by integrating the intensity over two time windows. For the first, short time window, a time interval between 0 and 2 ns was chosen in which

both the exciton emission and the RSL are observed for blends with ADT concentrations above 5%. The starting time for the second, longer time window was chosen individually for each blend such that the decay of the exciton emission was almost complete. A noteworthy result of the comparison of the spectra in these two time windows is the shift of the RSL to lower energies with increasing time (compare **Figure 4.10c** and **Figure 4.10d**). This points toward the existence of energetically low-lying sites such as grain boundaries where X_{RSL} is long-lived[44, 55, 57, 58] and which are populated via exciton diffusion, dominating the spectrum at late times. Importantly, the simultaneous observation of exciton emission and RSL at short times indicates that X_{RSL} can also be formed within crystalline domains of the polycrystalline mixed films, i.e., is not unique to defect sites. However, the low-lying defect sites provide an additional decay channel via exciton diffusion, leading to the observed red shift of the RSL. This interpretation is supported by **Figure 4.6c**, where the change in peak positions of the RSL in the late time window with changing ADT concentration is also shown. We find the same trend as in the steady state PL data, suggesting that X_{RSL} exhibits the same sensitivity on changes in the polarizability of the local molecular environment, independent of the time window, and, thus, also a high CT admixture, indicating that it is the same state in both time windows.

Based on these results and in particular considering the different response of the two decay channels (exciton vs RSL) to changes in the polarizability, we can now discuss the nature of X_{RSL} and its role in the SF of ADT. The most important result is its dependence on the polarizability of the local molecular environment, for which we use the change in the energy of the free exciton emission as a measure. When **Figure 4.6c** and **d** are

compared, clearly, both the free exciton emission and the RSL follow similar trends with decreasing ADT concentration and changes in the band gap of the codeposited compound. As discussed before, the main reason for the shift in energy of the exciton emission is a change in the polarizability of the local molecular environment, and the same reasoning has also been applied to the shift in RSL energy. However, plotting both shifts against each other gives interesting insight into the above-mentioned CT state admixture to X_{RSL}[53, 54]. It allows us now to elucidate the nature of X_{RSL} and, in particular, to distinguish between an excimer and the triplet-pair state (^{1}(TT)) as possible origins. The former is expected to be highly sensitive to changes in polarizability due to a large CT admixture[2]. Consequently, the corresponding shift in the energetic position of the excimer emission with changing mixing ratio (and, thus, changing polarizability of the local molecular environment) should be larger than that of the free exciton emission and the slope in **Figure 4.6e** becomes >1. For the second case, in order to understand the sensitivity of the ^{1}(TT) state to changes in the polarizability, the exact nature of this state has to be discussed first. The ^{1}(TT) state consists of not only two triplets but also a small admixture of other states, for example of the CT state[59, 60], making the sensitivity of the ^{1}(TT) state to changes in the polarizability slightly higher than that of uncorrelated triplets[54]. However, the admixture of these states can be considered small for several reasons. From a theoretical standpoint, calculations on pentacene[37, 59] and tetracene[60] only showed a small admixture of these states to the ^{1}(TT) state and since SF is occurring via the coherent mechanism in pentacene[44], while, in contrast, we showed that in ADT the incoherent SF mechanism is driving SF, it can be expected that the admixture of these states is even smaller in ADT than in pentacene[61].

Additionally, from an experimental viewpoint, a large admixture of such states to ^{1}(TT) would make the ^{1}(TT) state visible in absorption and photoluminescence spectroscopy without the need for Herzberg–Teller coupling[59], which, however, contrasts with our results. Also, a large admixture would result in a high binding energy between the two triplets in the ^{1}(TT) state, which would result in clear differences of the excited state absorption fingerprints between ^{1}(TT) and uncorrelated triplets. However, previous studies on comparable singlet fission chromophores revealed that it is generally very challenging to find spectroscopic differences between these two[12]. For such states like ^{1}(TT), which have a dominant triplet pair contribution and only a small CT state admixture, the energetic position of the corresponding emission is expected to be more stable upon changes in the polarizability of the local molecular environment due to a stronger localization of the corresponding excitation. Hence, if X_{RSL} was of ^{1}(TT) nature, a slope ≤ 1 would be expected in **Figure 4.10e**. Clearly, the slope in **Figure 4.10e** is larger than 1, unambiguously demonstrating that X_{RSL}, the state related to this RSL, has a large CT state admixture and, thus, is of excimeric rather than of ^{1}(TT) character.

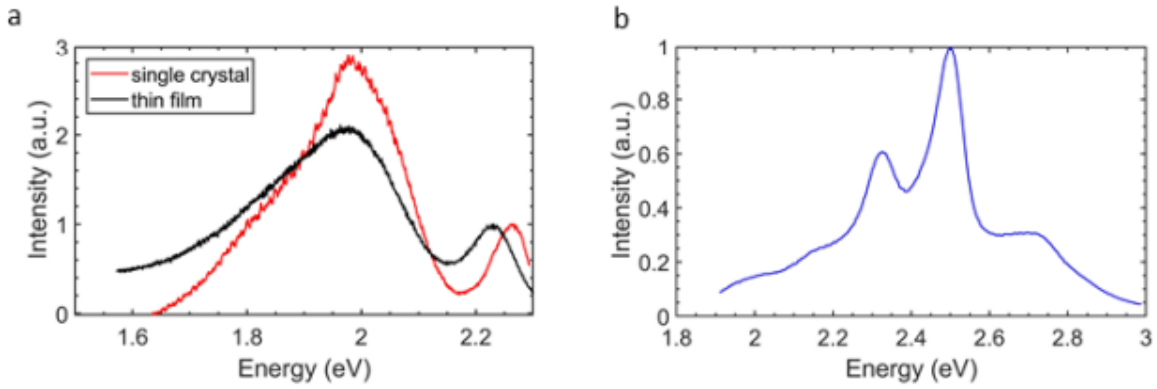

Figure 4.11 (a) Emission spectrum of a neat ADT thin film and an ADT single crystal. The single crystal spectrum has been performed with a LabRam HR 800 spectrometer (HORIBA Jobin Yvon, France) as well as a frequency-doubled Nd:YAG laser for 532 nm excitation wavelength. The crystal was kept under vacuum during the measurement. **(b)** PL quasisteady-state spectrum of ADT in solution. The peak at 2.7 eV is a scattering peak and hence not related to electronic transitions, the peak at 2.5 eV is assigned to the exciton and the peak at 2.3 eV to its vibronic progression.

Now, after X_{RSL} was identified as an excimer, the remaining question is whether it mediates SF or is a loss channel. We can rule out the excimer as the mediating species based on the lack of a concomitant increase of excimer luminescence on the time scale of the exciton decay (**Figure 4.9c-d**). Instead, two scenarios for the interrelation of excimer formation and SF are proposed (**Figure 4.10e-f**). In the first scenario photoexcitation leads to a nonrelaxed S_1 state, from where either ultrafast exciton relaxation to the free exciton band, followed by SF, or excimer formation can occur (**Figure 4.10e**). The second scenario assumes that excimer formation is facilitated at trap sites such as grain boundaries, while for the other sites SF is the dominant decay channel (**Figure 4.10f**). Since pronounced excimer emission is also observed in single crystals (**Figure 4.11**), despite the lack of grain boundaries and presumably a lower density of trap sites, the scenario in **Figure 4.10e** is favored. Importantly, neither the formation nor the decay of this excimer directly affects the SF process, suggesting neither a direct competition between SF and excimer formation

nor a mediation of SF by the excimer state in ADT, but instead the coexistence of two parallel channels at room temperature.

4.3 Conclusion

In conclusion, ADT blends with weakly interacting spacer molecules are a promising approach to clarify the origin of RSL features in PL spectra of SF materials. They allow us to clearly distinguish contributions from excimer and triplet-pair state emission based on their different response to changes in the polarizability of the local molecular environment and, thus, shed light on a current debate about the role of emissive states in molecular systems that undergo SF. Generally, this approach can be used to clarify the nature of RSL states in a variety of chromophores.

4.4 References

(1) He, R.; Chi, X.; Pinczuk, A.; Lang, D. V.; Ramirez, A. P. Extrinsic optical recombination in pentacene single crystals: Evidence of gap states. *Applied Physics Letters* **2005**, *87* (21), 211117. DOI: 10.1063/1.2135494.

(2) Birks, J. B. Excimers. *Reports on Progress in Physics* **1975**, *38* (8), 903-974. DOI: 10.1088/0034-4885/38/8/001.

(3) Hanna, M. C.; Nozik, A. J. Solar conversion efficiency of photovoltaic and photoelectrolysis cells with carrier multiplication absorbers. *Journal of Applied Physics* **2006**, *100* (7), 074510. DOI: 10.1063/1.2356795.

(4) Smith, M. B.; Michl, J. Recent Advances in Singlet Fission. *Annual Review of Physical Chemistry* **2013**, *64* (1), 361-386. DOI: 10.1146/annurev-physchem-040412-110130.

(5) Seiler, H.; Krynski, M.; Zahn, D.; Hammer, S.; Windsor, Y. W.; Vasileiadis, T.; Pflaum, J.; Ernstorfer, R.; Rossi, M.; Schwoerer, H. Nuclear dynamics of singlet exciton fission in pentacene single crystals. *Sci Adv* **2021**, *7* (26), eabg0869. DOI: 10.1126/sciadv.abg0869 PubMed.

(6) Birech, Z.; Schwoerer, M.; Schmeiler, T.; Pflaum, J.; Schwoerer, H. Ultrafast dynamics of excitons in tetracene single crystals. *The Journal of Chemical Physics* **2014**, *140* (11), 114501. DOI: 10.1063/1.4867696.

(7) Wilson, M. W. B.; Rao, A.; Clark, J.; Kumar, R. S. S.; Brida, D.; Cerullo, G.; Friend, R. H. Ultrafast Dynamics of Exciton Fission in Polycrystalline Pentacene. *J Am Chem Soc* **2011**, *133* (31), 11830-11833. DOI: 10.1021/ja201688h.

(8) Sanders, S. N.; Pun, A. B.; Parenti, K. R.; Kumarasamy, E.; Yablon, L. M.; Sfeir, M. Y.; Campos, L. M. Understanding the Bound Triplet-Pair State in Singlet Fission. *Chem* **2019**, *5* (8), 1988-2005. DOI: 10.1016/j.chempr.2019.05.012.

(9) Burdett, J. J.; Bardeen, C. J. Quantum Beats in Crystalline Tetracene Delayed Fluorescence Due to Triplet Pair Coherences Produced by Direct Singlet Fission. *J Am Chem Soc* **2012**, *134* (20), 8597-8607. DOI: 10.1021/ja301683w.

(10) Burdett, J. J.; Gosztola, D.; Bardeen, C. J. The dependence of singlet exciton relaxation on excitation density and temperature in polycrystalline tetracene thin films: Kinetic evidence for a dark intermediate state and implications for singlet fission. *The Journal of Chemical Physics* **2011**, *135* (21), 214508. DOI: 10.1063/1.3664630.

(11) Piland, G. B.; Bardeen, C. J. How Morphology Affects Singlet Fission in Crystalline Tetracene. *The Journal of Physical Chemistry Letters* **2015**, *6* (10), 1841-1846. DOI: 10.1021/acs.jpclett.5b00569.

(12) Stern, H. L.; Musser, A. J.; Gelinas, S.; Parkinson, P.; Herz, L. M.; Bruzek, M. J.; Anthony, J.; Friend, R. H.; Walker, B. J. Identification of a triplet pair intermediate in singlet exciton fission in solution. *Proc Natl Acad Sci U S A* **2015**, *112* (25), 7656-7661. DOI: 10.1073/pnas.1503471112 PubMed.

(13) Bossanyi, D. G.; Matthiesen, M.; Wang, S.; Smith, J. A.; Kilbride, R. C.; Shipp, J. D.; Chekulaev, D.; Holland, E.; Anthony, J. E.; Zaumseil, J.; et al. Emissive spin-0 triplet-pairs are a direct product of triplet–triplet annihilation in pentacene single crystals and anthradithiophene films. *Nature Chemistry* **2020**, *13* (2), 163-171. DOI: 10.1038/s41557-020-00593-y.

(14) Dover, C. B.; Gallaher, J. K.; Frazer, L.; Tapping, P. C.; Petty, A. J.; Crossley, M. J.; Anthony, J. E.; Kee, T. W.; Schmidt, T. W. Endothermic singlet fission is hindered by excimer formation. *Nature Chemistry* **2018**, *10* (3), 305-310. DOI: 10.1038/nchem.2926.

(15) Cruz, C. D.; Chronister, E. L.; Bardeen, C. J. Using temperature dependent fluorescence to evaluate singlet fission pathways in tetracene single crystals. *The Journal of Chemical Physics* **2020**, *153* (23), 234504. DOI: 10.1063/5.0031458.

(16) Tayebjee, M. J. Y.; Clady, R. G. C. R.; Schmidt, T. W. The exciton dynamics in tetracene thin films. *Physical Chemistry Chemical Physics* **2013**, *15* (35), 14797. DOI: 10.1039/c3cp52609g.

(17) Zimmerman, P. M.; Bell, F.; Casanova, D.; Head-Gordon, M. Mechanism for Singlet Fission in Pentacene and Tetracene: From Single Exciton to Two Triplets. *J Am Chem Soc* **2011**, *133* (49), 19944-19952. DOI: 10.1021/ja208431r.

(18) Musser, A. J.; Clark, J. Triplet-Pair States in Organic Semiconductors. *Annual Review of Physical Chemistry* **2019**, *70* (1), 323-351. DOI: 10.1146/annurev-physchem-042018-052435.

(19) Thampi, A.; Stern, H. L.; Cheminal, A.; Tayebjee, M. J. Y.; Petty, A. J.; Anthony, J. E.; Rao, A. Elucidation of Excitation Energy Dependent Correlated Triplet Pair Formation Pathways in an Endothermic Singlet Fission System. *J Am Chem Soc* **2017**, *140* (13), 4613-4622. DOI: 10.1021/jacs.7b06274.

(20) Yong, C. K.; Musser, A. J.; Bayliss, S. L.; Lukman, S.; Tamura, H.; Bubnova, O.; Hallani, R. K.; Meneau, A.; Resel, R.; Maruyama, M.; et al. The entangled triplet pair state in acene and heteroacene materials. *Nat Commun* **2017**, *8*, 15953-15953. DOI: 10.1038/ncomms15953 PubMed.

(21) Kolata, K.; Breuer, T.; Witte, G.; Chatterjee, S. Molecular Packing Determines Singlet Exciton Fission in Organic Semiconductors. *ACS Nano* **2014**, *8* (7), 7377-7383. DOI: 10.1021/nn502544d.

(22) Feng, X.; Krylov, A. I. On couplings and excimers: lessons from studies of singlet fission in covalently linked tetracene dimers. *Physical Chemistry Chemical Physics* **2016**, *18* (11), 7751-7761. DOI: 10.1039/c6cp00177g.

(23) Liu, H.; Nichols, V. M.; Shen, L.; Jahansouz, S.; Chen, Y.; Hanson, K. M.; Bardeen, C. J.; Li, X. Synthesis and photophysical properties of a "face-to-face" stacked tetracene dimer. *Physical Chemistry Chemical Physics* **2015**, *17* (9), 6523-6531. DOI: 10.1039/c4cp05444j.

(24) Ni, W.; Sun, L.; Gurzadyan, G. G. Ultrafast spectroscopy reveals singlet fission, ionization and excimer formation in perylene film. *Sci Rep* **2021**, *11* (1), 5220-5220. DOI: 10.1038/s41598-021-83791-z PubMed.

(25) Dron, P. I.; Michl, J.; Johnson, J. C. Singlet Fission and Excimer Formation in Disordered Solids of Alkyl-Substituted 1,3-Diphenylisobenzofurans. *The Journal of Physical Chemistry A* **2017**, *121* (45), 8596-8603. DOI: 10.1021/acs.jpca.7b07362.

(26) Ye, C.; Gray, V.; Mårtensson, J.; Börjesson, K. Annihilation Versus Excimer Formation by the Triplet Pair in Triplet-Triplet Annihilation Photon Upconversion. *J Am Chem Soc* **2019**, *141* (24), 9578-9584. DOI: 10.1021/jacs.9b02302 PubMed.

(27) Miller, C. E.; Wasielewski, M. R.; Schatz, G. C. Modeling Singlet Fission in Rylene and Diketopyrrolopyrrole Derivatives: The Role of the Charge Transfer State in Superexchange and Excimer Formation. *The Journal of Physical Chemistry C* **2017**, *121* (19), 10345-10350. DOI: 10.1021/acs.jpcc.7b02697.

(28) Mauck, C. M.; Hartnett, P. E.; Margulies, E. A.; Ma, L.; Miller, C. E.; Schatz, G. C.; Marks, T. J.; Wasielewski, M. R. Singlet Fission via an Excimer-Like Intermediate in 3,6-Bis(thiophen-2-yl)diketopyrrolopyrrole Derivatives. *J Am Chem Soc* **2016**, *138* (36), 11749-11761. DOI: 10.1021/jacs.6b05627.

(29) Walker, B. J.; Musser, A. J.; Beljonne, D.; Friend, R. H. Singlet exciton fission in solution. *Nature Chemistry* **2013**, *5* (12), 1019-1024. DOI: 10.1038/nchem.1801.

(30) Dean, J. C.; Zhang, R.; Hallani, R. K.; Pensack, R. D.; Sanders, S. N.; Oblinsky, D. G.; Parkin, S. R.; Campos, L. M.; Anthony, J. E.; Scholes, G. D. Photophysical characterization and time-resolved spectroscopy of a anthradithiophene dimer: exploring the role of conformation in singlet fission. *Physical Chemistry Chemical Physics* **2017**, *19* (34), 23162-23175. DOI: 10.1039/c7cp03774k.

(31) Young, R. M.; Wasielewski, M. R. Mixed Electronic States in Molecular Dimers: Connecting Singlet Fission, Excimer Formation, and Symmetry-Breaking Charge Transfer. *Accounts of Chemical Research* **2020**, *53* (9), 1957-1968. DOI: 10.1021/acs.accounts.0c00397.

(32) Schrauben, J. N.; Ryerson, J. L.; Michl, J.; Johnson, J. C. Mechanism of Singlet Fission in Thin Films of 1,3-Diphenylisobenzofuran. *J Am Chem Soc* **2014**, *136* (20), 7363-7373. DOI: 10.1021/ja501337b.

(33) Sandoval-Salinas, M. E.; Casanova, D. The Doubly Excited State in Singlet Fission. *ChemPhotoChem* **2020**, *5* (3), 282-293. DOI: 10.1002/cptc.202000211.

(34) Huang, Y.; Buyanova, I. A.; Phansa, C.; Sandoval-Salinas, M. E.; Casanova, D.; Myers, W. K.; Greenham, N. C.; Rao, A.; Chen, W. M.; Puttisong, Y. Competition between triplet pair formation and excimer-like recombination controls singlet fission yield. *Cell Reports Physical Science* **2021**, *2* (2), 100339. DOI: 10.1016/j.xcrp.2021.100339.

(35) Müller, U.; Roos, L.; Frank, M.; Deutsch, M.; Hammer, S.; Krumrein, M.; Friedrich, A.; Marder, T. B.; Engels, B.; Krueger, A.; et al. Role of Intermolecular Interactions in the Excited-State Photophysics of Tetracene and 2,2′-Ditetracene. *The Journal of Physical Chemistry C* **2020**, *124* (36), 19435-19446. DOI: 10.1021/acs.jpcc.0c04066.

(36) Zimmerman, P. M.; Zhang, Z.; Musgrave, C. B. Singlet fission in pentacene through multi-exciton quantum states. *Nature Chemistry* **2010**, *2* (8), 648-652. DOI: 10.1038/nchem.694.

(37) Zeng, T.; Hoffmann, R.; Ananth, N. The Low-Lying Electronic States of Pentacene and Their Roles in Singlet Fission. *J Am Chem Soc* **2014**, *136* (15), 5755-5764. DOI: 10.1021/ja500887a.

(38) Hervé, P.; Vandamme, L. K. J. General relation between refractive index and energy gap in semiconductors. *Infrared Physics & Technology* **1994**, *35* (4), 609-615. DOI: 10.1016/1350-4495(94)90026-4.

(39) Laquindanum, J. G.; Katz, H. E.; Lovinger, A. J. Synthesis, Morphology, and Field-Effect Mobility of Anthradithiophenes. *J Am Chem Soc* **1998**, *120* (4), 664-672. DOI: 10.1021/ja9728381.

(40) Mamada, M.; Katagiri, H.; Mizukami, M.; Honda, K.; Minamiki, T.; Teraoka, R.; Uemura, T.; Tokito, S. syn-/anti-Anthradithiophene Derivative Isomer Effects on Semiconducting Properties. *ACS Applied Materials & Interfaces* **2013**, *5* (19), 9670-9677. DOI: 10.1021/am4027136.

(41) Tylleman, B.; Vande Velde, C. M. L.; Balandier, J.-Y.; Stas, S.; Sergeyev, S.; Geerts, Y. H. Synthesis of Isomerically Pure anti-Anthradithiophene Derivatives. *Organic Letters* **2011**, *13* (19), 5208-5211. DOI: 10.1021/ol202089t.

(42) Nahm, R. K.; Engstrom, J. R. Who's on first? Tracking in real time the growth of multiple crystalline phases of an organic semiconductor: Tetracene on SiO₂. *The Journal of Chemical Physics* **2017**, *146* (5), 052815. DOI: 10.1063/1.4971288.

(43) Aufderheide, A.; Broch, K.; Novák, J.; Hinderhofer, A.; Nervo, R.; Gerlach, A.; Banerjee, R.; Schreiber, F. Mixing-Induced Anisotropic Correlations in Molecular Crystalline Systems. *Physical Review Letters* **2012**, *109* (15). DOI: 10.1103/physrevlett.109.156102.

(44) Zeiser, C.; Cruz, C.; Reichman, D. R.; Seitz, M.; Hagenlocher, J.; Chronister, E. L.; Bardeen, C. J.; Tempelaar, R.; Broch, K. Vacancy control in acene blends links exothermic singlet fission to coherence. *Nat Commun* **2021**, *12* (1), 5149-5149. DOI: 10.1038/s41467-021-25395-9 PubMed.

(45) Subramanian, S.; Park, S. K.; Parkin, S. R.; Podzorov, V.; Jackson, T. N.; Anthony, J. E. Chromophore Fluorination Enhances Crystallization and Stability of Soluble Anthradithiophene Semiconductors. *J Am Chem Soc* **2008**, *130* (9), 2706-2707. DOI: 10.1021/ja073235k.

(46) Lloyd, M. T.; Mayer, A. C.; Subramanian, S.; Mourey, D. A.; Herman, D. J.; Bapat, A. V.; Anthony, J. E.; Malliaras, G. G. Efficient Solution-Processed Photovoltaic Cells Based on an Anthradithiophene/Fullerene Blend. *J Am Chem Soc* **2007**, *129* (29), 9144-9149. DOI: 10.1021/ja072147x.

(47) Jurchescu, O. D.; Subramanian, S.; Kline, R. J.; Hudson, S. D.; Anthony, J. E.; Jackson, T. N.; Gundlach, D. J. Organic Single-Crystal Field-Effect Transistors of a Soluble Anthradithiophene. *Chemistry of Materials* **2008**, *20* (21), 6733-6737. DOI: 10.1021/cm8021165.

(48) Platt, A. D.; Day, J.; Subramanian, S.; Anthony, J. E.; Ostroverkhova, O. Optical, Fluorescent, and (Photo)conductive Properties of High-Performance Functionalized Pentacene and Anthradithiophene Derivatives. *The Journal of Physical Chemistry C* **2009**, *113* (31), 14006-14014. DOI: 10.1021/jp904021p.

(49) Kwon, O.; Coropceanu, V.; Gruhn, N. E.; Durivage, J. C.; Laquindanum, J. G.; Katz, H. E.; Cornil, J.; Brédas, J. L. Characterization of the molecular parameters determining charge transport in anthradithiophene. *The Journal of Chemical Physics* **2004**, *120* (17), 8186-8194. DOI: 10.1063/1.1689636.

(50) Tanaka, S.; Miyata, K.; Sugimoto, T.; Watanabe, K.; Uemura, T.; Takeya, J.; Matsumoto, Y. Enhancement of the Exciton Coherence Size in Organic Semiconductor by Alkyl Chain Substitution. *The Journal of Physical Chemistry C* **2016**, *120* (15), 7941-7948. DOI: 10.1021/acs.jpcc.5b12686.

(51) Broch, K.; Dieterle, J.; Branchi, F.; Hestand, N. J.; Olivier, Y.; Tamura, H.; Cruz, C.; Nichols, V. M.; Hinderhofer, A.; Beljonne, D.; et al. Robust singlet fission in pentacene thin films with tuned charge transfer interactions. *Nat Commun* **2018**, *9* (1), 954-954. DOI: 10.1038/s41467-018-03300-1 PubMed.

(52) Beljonne, D.; Yamagata, H.; Brédas, J. L.; Spano, F. C.; Olivier, Y. Charge-Transfer Excitations Steer the Davydov Splitting and Mediate Singlet Exciton Fission in Pentacene. *Physical Review Letters* **2013**, *110* (22). DOI: 10.1103/physrevlett.110.226402.

(53) Yamagata, H.; Norton, J.; Hontz, E.; Olivier, Y.; Beljonne, D.; Brédas, J. L.; Silbey, R. J.; Spano, F. C. The nature of singlet excitons in oligoacene molecular crystals. *The Journal of Chemical Physics* **2011**, *134* (20), 204703. DOI: 10.1063/1.3590871.

(54) Marcus, R. A. On the Theory of Shifts and Broadening of Electronic Spectra of Polar Solutes in Polar Media. *The Journal of Chemical Physics* **1965**, *43* (4), 1261-1274. DOI: 10.1063/1.1696913.

(55) Gao, Y.; Liu, H.; Zhang, S.; Gu, Q.; Shen, Y.; Ge, Y.; Yang, B. Excimer formation and evolution of excited state properties in discrete dimeric stacking of an anthracene derivative: a computational investigation. *Physical Chemistry Chemical Physics* **2018**, *20* (17), 12129-12137. DOI: 10.1039/c8cp00834e.

(56) Chen, Y.; Shen, L.; Li, X. Effects of Heteroatoms of Tetracene and Pentacene Derivatives on Their Stability and Singlet Fission. *The Journal of Physical Chemistry A* **2014**, *118* (30), 5700-5708. DOI: 10.1021/jp503114b.

(57) Arnold, S.; Alfano, R. R.; Pope, M.; Yu, W.; Ho, P.; Selsby, R.; Tharrats, J.; Swenberg, C. E. Triplet exciton caging in two dimensions. *The Journal of Chemical Physics* **1976**, *64* (12), 5104-5114. DOI: 10.1063/1.432184.

(58) Casanova, D. Theoretical investigations of the perylene electronic structure: Monomer, dimers, and excimers. *International Journal of Quantum Chemistry* **2015**, *115* (7), 442-452. DOI: 10.1002/qua.24869.

(59) Tempelaar, R.; Reichman, D. R. Vibronic exciton theory of singlet fission. I. Linear absorption and the anatomy of the correlated triplet pair state. *The Journal of Chemical Physics* **2017**, *146* (17), 174703. DOI: 10.1063/1.4982362.

(60) Morrison, A. F.; Herbert, J. M. Evidence for Singlet Fission Driven by Vibronic Coherence in Crystalline Tetracene. *The Journal of Physical Chemistry Letters* **2017**, *8* (7), 1442-1448. DOI: 10.1021/acs.jpclett.7b00230.

(61) Alvertis, A. M.; Lukman, S.; Hele, T. J. H.; Fuemmeler, E. G.; Feng, J.; Wu, J.; Greenham, N. C.; Chin, A. W.; Musser, A. J. Switching between Coherent and Incoherent Singlet Fission via Solvent-Induced Symmetry Breaking. *J Am Chem Soc* **2019**, *141* (44), 17558-17570. DOI: 10.1021/jacs.9b05561.

Chapter 5. Analysis of Molecular Photomechanical Performance Using a One-Dimensional Harmonic Model

After establishing the role of excimer formation in multi-exciton materials, we turn our attention to an alternative application to harnessing solar energy: photomechanical work. Photomechanical crystals and materials, however, lack an underlying theoretical model to predict the work efficiency and the ultimate limits to a molecular photomechanical system. This chapter remedies this deficiency with a simple, 1-D harmonic oscillator model to establish the upper limit of work efficiency that can be expected for a single molecule photomechanical actuator.

5.1 Introduction

The use of photons to transport energy is appealing thanks to their ability to propagate long distances with low loss, their resistance to electromagnetic interference, and their wide range of controllable parameters like wavelength, polarization, and coherence. Once they reach their destination, however, photons must be converted to a more useful form of energy, like heat or mechanical work. To generate mechanical work, one option is to convert them into an electrical potential that can be harnessed to drive actuator devices. This strategy requires two elements: a photovoltaic module to generate current, and a device to convert this electrical energy into a mechanical output, like an electric motor or piezoelectric crystal. Another option is to utilize a material that directly converts the absorbed photon into mechanical motion without relying on free electrons and external circuitry. Photomechanical materials have the property that their constituent nuclei change position after photon absorption, generating a force and displacement that can be harnessed

to perform mechanical work.[1-3] This change in atomic coordinates could result from heating (photothermal)[4-6], a change in electronic state (photostrictive)[7], or a chemical reaction (photochemical).[8]

The photochemical approach to photomechanical materials relies on harnessing molecular reactions, like cis-trans isomerization, to drive deformations in solid-state systems like polymers[9-11] and crystals.[12-17] To be useful in practical actuator devices, the photochemical product should be able to return to the reactant state either by thermal fluctuations (T-type reversibility) or by a second photon absorption (P-type reversibility).[18, 19] To assess the potential of this class of photomechanical materials, specifically their efficiency and work output, it would be useful to have a simple theoretical framework that could be used to analyze such systems at the molecular level. The Bell model for mechanochemistry[20] and the Marcus-Hush model for electron transfer [21] are examples of semiclassical approaches based on displaced harmonic oscillators. An analogous model for the photomechanical response of a molecule could provide the basis for interpretation of experimental results and the design of improved materials. Such a framework could also help address practical questions, like how the photomechanical

approach to energy conversion compares to the photovoltaic approach in terms of figures of merit like efficiency.

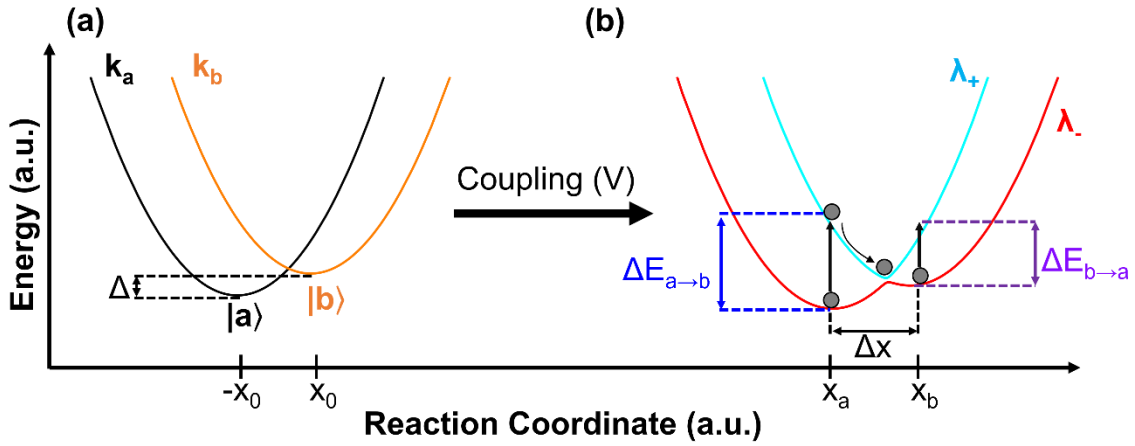

Figure 5.1 (a) Two uncoupled diabatic harmonic surfaces, centered at ± x_0, with energy offset Δ, that serve as the starting point for the calculations. **(b)** Adiabatic $\lambda_\pm$ energy surfaces created by electronic coupling term V, along with the relevant energy gaps.

The goal of this chapter is to develop a simple one-dimensional (1D) model that can serve as a starting point for more realistic models of the photomechanical response. First, we introduce the harmonic model with two states, denoted |a⟩ and |b⟩, that correspond to two different nuclear configurations. When an external force is applied, this simple model generates predictions that are qualitatively consistent with standard mechanochemistry models. We next analyze the photomechanical process and derive expressions for the work output, blocking force, and absorbed photon-to-work efficiency of the |a⟩ → |b⟩ reaction. If the starting state |a⟩ is the stable isomer (lower energy than |b⟩), we find that it is possible to attain photon-to-work efficiencies of >50%. If |a⟩ is higher in energy, i.e. a metastable isomer, then one-way efficiencies >100% are possible by releasing the stored potential energy. We also analyze the effects of nonadiabatic electronic coupling, unequal frequency potentials, and the |a⟩→|b⟩→|a⟩ cycling efficiency.

We conclude that photomechanical materials have the potential to surpass a photovoltaic-piezoelectric combination and approach that of a photovoltaic-motor combination. Given that most measured photomechanical efficiencies are orders of magnitude below the theoretical limits derived in this chapter, our results suggest that there is substantial room for improvement in this class of materials.

5.2 Results and Discussion

The model used for our calculations is shown in **Figure 5.1**.[22] Two harmonic potential energy surfaces represent electronic states $|a\rangle$ and $|b\rangle$. We always assume the system starts in state $|a\rangle$. The force constants are k_a and k_b, respectively, and the coordinate system is chosen so that the minima lie at $\pm x_0$ along the reaction coordinate in the absence of an applied force. State $|b\rangle$ is offset in energy by an amount Δ. If Δ is positive, then the initial state $|a\rangle$ is the lowest energy, stable state and state $|b\rangle$ can be associated with either a relaxed excited state or an isomerized molecule. If $\Delta<0$, then state $|a\rangle$ is a higher energy, metastable state that must be populated by some other process, e.g. previous absorption of a photon. Finally, states $|a\rangle$ and $|b\rangle$ are coupled by an interaction term V, which we assume to be a real number. The overall Hamiltonian is given by

$$\hat{H}=|a\rangle E_a\langle a|+|b\rangle E_b\langle b|+V(|a\rangle\langle b|+|b\rangle\langle a|) \qquad \text{(eqn. 5.1)}$$

with

$$E_a=\frac{1}{2}k_a(x+x_0)^2 \qquad \text{(eqn. 5.2)}$$

$$E_b=\frac{1}{2}k_b(x-x_0)^2+\Delta$$

(eqn. 5.3)

Diagonalization of this Hamiltonian generates two adiabatic potential energy surfaces (PESs) whose energies $\lambda_\pm$ are given by

$$\lambda_\pm(x)=\frac{1}{2}\left[E_a(x)+E_b(x)\pm\sqrt{\left(E_b(x)-E_a(x)\right)^2+4V^2}\right]$$

(eqn. 5.4)

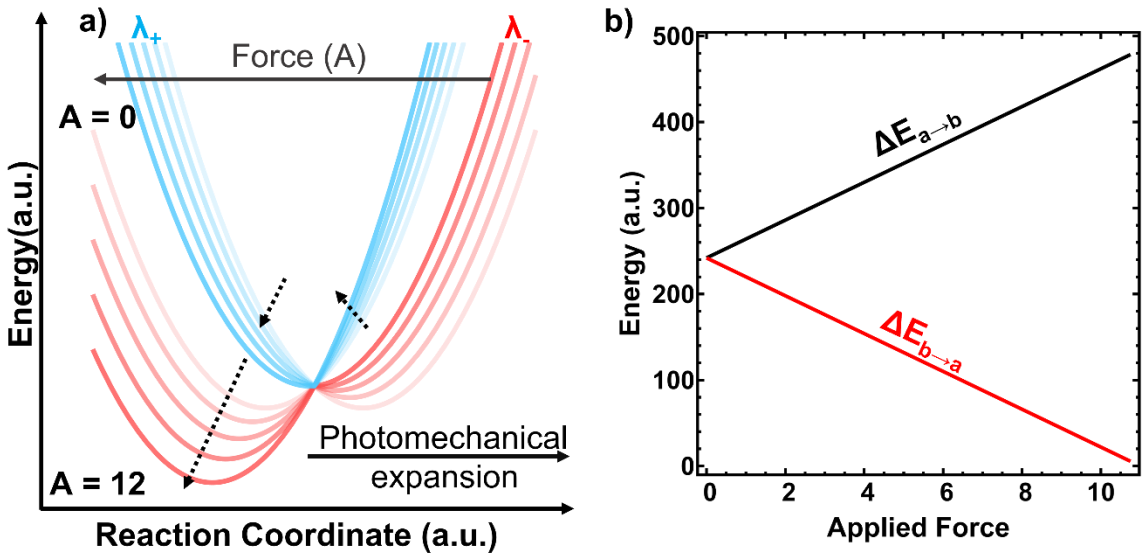

Figure 5.2 (a) As the force acting against photoisomerization increases, both the ground state (λ_-) and excited state (λ_+) energy minima shift to the left. Eventually the barrier between the ground state minima vanishes **(b)** The shifts in the optical gaps (ΔE) as a function of applied force A. For these calculations, $x_0 = 11$, $k_a = k_b = 1$, $A_{stop} = 11$.

If a constant force A is applied that pushes the system to the left in **Figure 5.1a**, i.e. toward state $|a\rangle$, we have an additional potential energy term $U(x)=-Ax$. This force resists the $|a\rangle$

$\rightarrow|b\rangle$ reaction and modifies the Hamiltonian. If we neglect V, the new $|a\rangle$ and $|b\rangle$ PES curves are given by

$$E_a(x)=\frac{1}{2}k_a\left(x-\left(-x_0-\frac{A}{k_a}\right)\right)^2+Ax_a-\frac{A^2}{2k_a}$$

(eqn. 5.5)

$$E_b(x)=\frac{1}{2}k_b\left(x-\left(+x_0-\frac{A}{k_b}\right)\right)^2+Ax_b-\frac{A^2}{2k_b}+\Delta$$

(eqn. 5.6)

The modified PESs are shown in **Figure 5.1b**. The applied force shifts the potential minima to new positions x_a and x_b. The barrier height between the new $|a\rangle$ and $|b\rangle$ minima (x_a and x_b) is lowered by the force and disappears when the potential curve of $|a\rangle$ crosses through the minimum of the $|b\rangle$ potential well, as shown in **Figure 5.2a**. The force at which the potential minimum at x_b disappears is denoted the blocking force or stop-force A_{stop} and represents the maximum force under which the system can maintain two stable points. Note that as A increases, the optical gaps between the $|a\rangle$ and $|b\rangle$ surfaces at stable points x_a and x_b also changes, with the gap at x_a increasing and that at x_b decreasing (**Figure 5.2b**).

At this point, it is useful to place this model in the context of mechanochemical systems, where the reaction rate depends on the ground state energy barrier between x_b and x_a.[23] If we assume that $|b\rangle$ is the reactant that must reach the lower energy product state $|a\rangle$, we can calculate the barrier as a function of *A* for various parameter values. **Figure 5.3** plots the barrier height $\Delta E^{\ddagger}$ versus A for various nonadiabatic coupling values V. For low *A* values, there is a linear dependence of $\Delta E^{\ddagger}$ on A, which saturates at larger forces. This linear dependence of $\Delta E^{\ddagger}$ on A is consistent with most theoretical treatments of the effects

of an applied force on reaction rates. [24, 25] Note that the net effect is to change the thermal $|b\rangle \rightarrow |a\rangle$ rate. No thermodynamic work is performed since the motion along the reaction coordinate is parallel to the applied force.

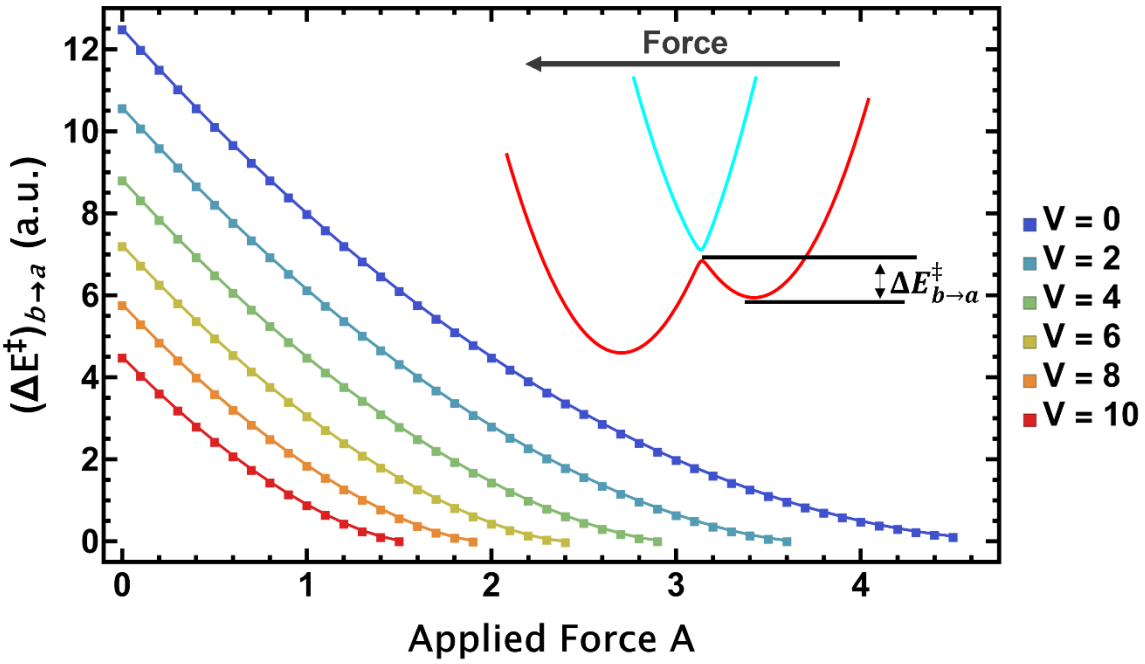

Figure 5.3 The dependence of the ground state activation energy $\Delta E^{\ddagger}_{b\to a}$ as the applied force A is increased for different values of the electronic coupling V. For these calculations, $k_a = k_b = 1$, $x_0 = -5$, and $\Delta = 0$. **Inse**t: Illustration of the ground state PES (red) showing $\Delta E^{\ddagger}_{b\to a}$.

We now turn to the photomechanical process in which the system is forced to work against the applied force by photoexcitation from $|a\rangle$ to $|b\rangle$. The system starts at x_a, absorbs a photon to go to the upper surface, and relaxes to x_b as shown in **Figure 5.1b**. The work output *W* in this case is given by the usual definition of force×distance,

$$W_{a\to b} = A(x_b - x_a) = A\Delta x \qquad \text{(eqn. 5.7)}$$

The input photon energy is just the difference between the |a⟩ and |b⟩ potentials at the starting position x_a,

$$\Delta E_{a\to b}=E_b(x_a)-E_a(x_a)$$

(eqn. 5.8)

With V = 0, we can use (eqn. 5.5-(eqn. 5.8 to find:

$$E_{a\to b}=2k_b x_0^2+2Ax_0\left(\frac{k_b}{k_a}\right)+\frac{A^2(k_b-k_a)}{2k_a^2}+\Delta$$

(eqn. 5.9)

$$W_{a\to b}=2Ax_0+A^2\left(\frac{1}{k_b}-\frac{1}{k_a}\right)$$

(eqn. 5.10)

These equations can be combined to obtain an expression for the |a⟩→ b⟩ efficiency $\eta_{a\to b}$,

$$\eta_{a\to b}=\frac{2Ax_0+A^2\left(\frac{1}{k_b}-\frac{1}{k_a}\right)}{2k_b x_0^2+2Ax_0\left(\frac{k_b}{k_a}\right)+\frac{A^2(k_b-k_a)}{2k_a^2}+\Delta}$$

(eqn. 5.11)

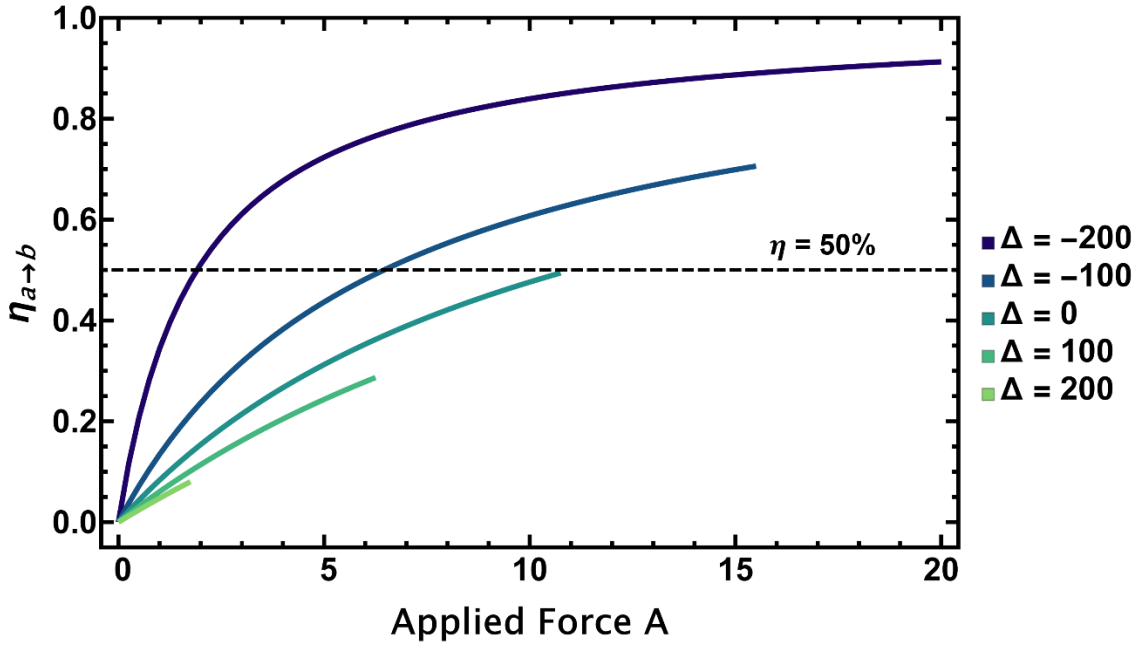

Figure 5.4 The photomechanical efficiency $\eta_{a\to b}$ plotted as a function of applied force A and different Δ energy offsets. These calculations were done with $x_0 = 11$, $k_a = k_b = 1$, and V = 0. For these parameters, the maximum efficiency occurs at A_{stop}.

The maximum A that can be applied to the system is limited by the necessity that there exist two stable minima that the molecule can be switched between. In other words, the efficiency will be maximized at A_{stop} and this maximum efficiency is η_{stop}. Again, for V=0 we calculate

$$A_{stop} = \left(\frac{k_b}{k_a - k_b}\right)\left[2k_a x_0 - k_b\sqrt{4k_a k_b x_0^2 - 2\Delta(k_b - k_a)}\right] \qquad \text{(eqn. 5.12)}$$

Substituting this value back into (eqn. 5.11 allows us to obtain a general expression for the efficiency at the stop-force (η_{stop}),

$$\eta_{stop}=\frac{2k_ak_b}{k_a^2-k_b^2}\left[\frac{\Delta(k_b-k_a)-2k_ak_bx_0^2+k_ax_0\sqrt{4k_ak_bx_0^2+2\Delta(k_a-k_b)}}{2k_ak_bx_0^2+\Delta(k_a-k_b)}\right]$$

(eqn. 5.13)

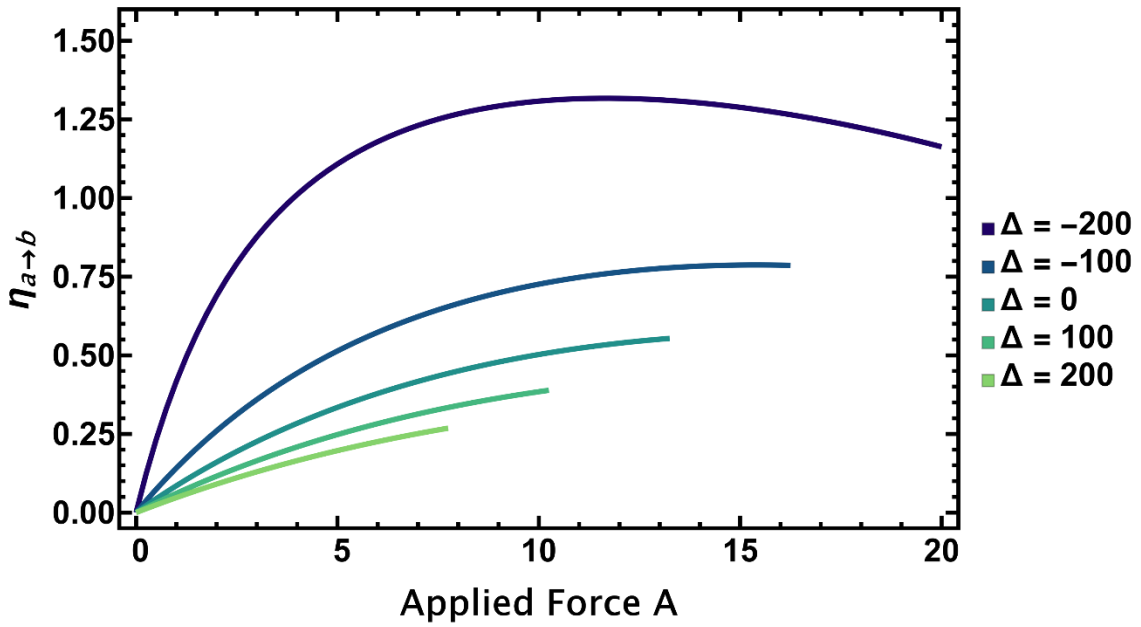

Figure 5.5 The forward reaction work efficiency plotted as a function of applied force for the system $x_0 = 11$, $k_a = 2.315$, $k_b = 1$, and $V = 0$. With sufficiently negative Δ, the one-way efficiency exceeds 100%, releasing the "stored energy" captured in the metastable state.

Note that this expression is valid for any value of Δ, positive or negative. In **Figure 5.4** we plot $\eta_{a\to b}$ as a function of A for $k_a/k_b = 1$. For this condition, $\eta_{a\to b}$ is an increasing function of A and is maximized at A_{stop} for all values of Δ. In fact, for the most common scenario where $\Delta \geq 0$, the efficiency is always maximized at A_{stop}. Only when $\Delta < 0$ and $k_a > k_b$ do we find that the maximum $\eta_{a\to b}$ does not occur at A_{stop} but at an intermediate force. In this case, the maximum $\eta_{a\to b}$ can even surpass 1.0 (**Figure 5.5**). For $\Delta < 0$, the large $\eta_{a\to b}$ values are an artifact of our neglect of the energetic cost of preparing this state

but serve to illustrate how the 1D system can be "pre-loaded" to produce more mechanical energy than the input photon.

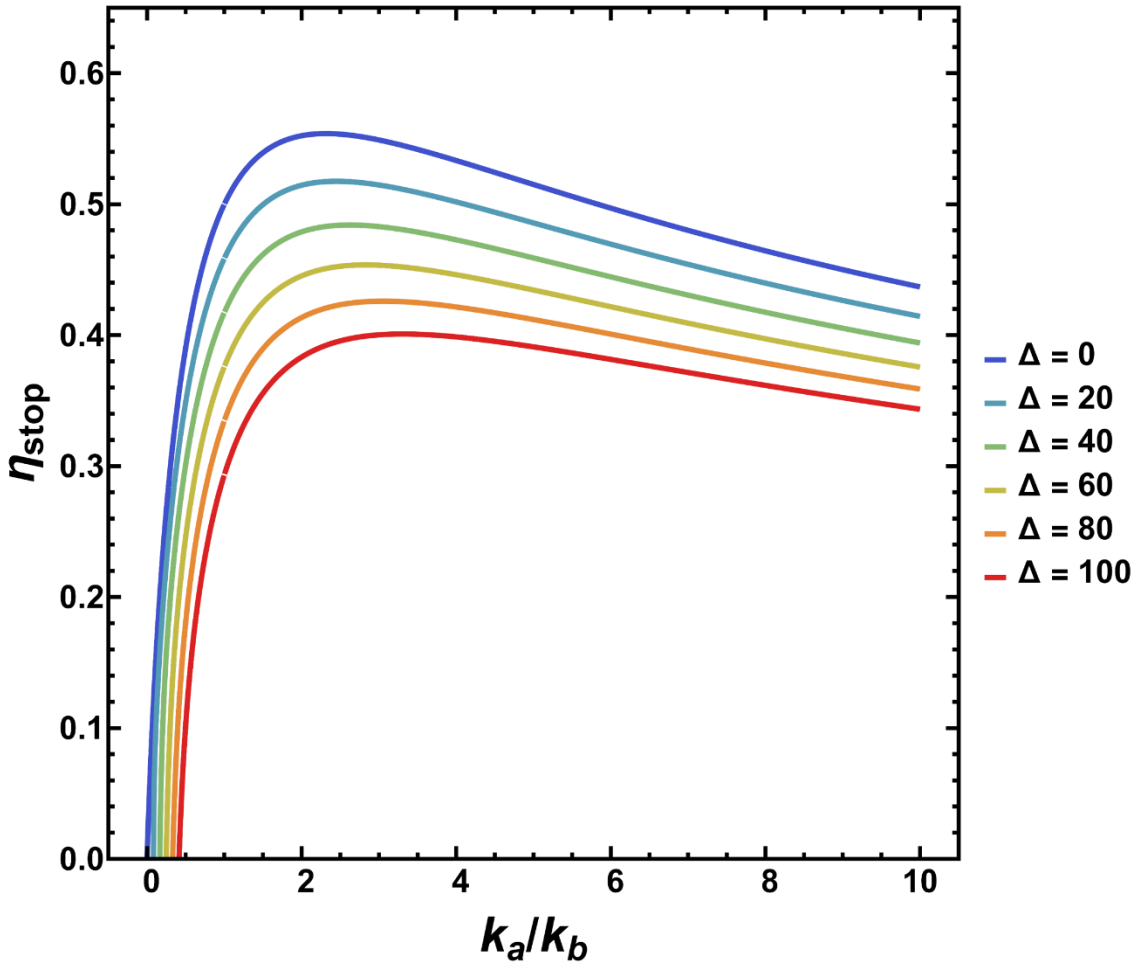

Figure 5.6 The photomechanical efficiency η_{stop} plotted as a function of k_a/k_b for different values of Δ. When $\Delta > 0$, smaller ratios of k_a/k_b become inaccessible (and thus $\eta = 0$) as only one stable minimum exists along under the absence of applied force.

For the remainder of this chapter, we will concentrate on the $\Delta \geq 0$ case that is most relevant for practical materials. Note that our model assumes the quantum yield for isomerization is unity in all cases. The molecular parameters that determine efficiency are k_a, k_b, Δ and V. To examine the role of the first three parameters in the limit of V=0, in

Figure 5.6 we plot η_{stop} versus the ratio k_a/k_b for various Δ values. The first observation is that η_{stop} is maximized for $\Delta=0$. For $\Delta>0$, the efficiency decreases as the input energy cost increases, as predicted by (eqn. 5.11) . The behavior of η_{stop} as a function of the force constants is more complex. When $k_a = k_b = k$, (eqn. 5.13 reduces to

$$\eta=\frac{2Ax_0}{2kx_0^2+2Ax_0+\Delta}$$

(eqn. 5.14)

In this limit, $A_{stop} = kx_0 - \Delta/(2kx_0)$ and we find:

$$\eta_{stop}=\frac{2kx_0^2-\frac{\Delta}{k}}{4kx_0^2+\Delta\left(1-\frac{1}{k}\right)}$$

(eqn. 5.15)

This expression leads to a maximum $\eta_{stop} = 0.5$ when $\Delta = 0$. But the largest η_{stop} values are obtained for $k_a/k_b > 1$ for all Δ values, meaning that the $|b\rangle$ PES has a lower frequency and a shallower well. We found a maximum efficiency η_{stop} of 0.554 for $k_a/k_b = 2.315$ and $\Delta = 0$. At larger Δ values, the maximum η_{stop} decreases and shifts to slightly larger k_a/k_b ratios, for example a maximum occurs at $k_a/k_b = 3.307$ when $\Delta = 100$.

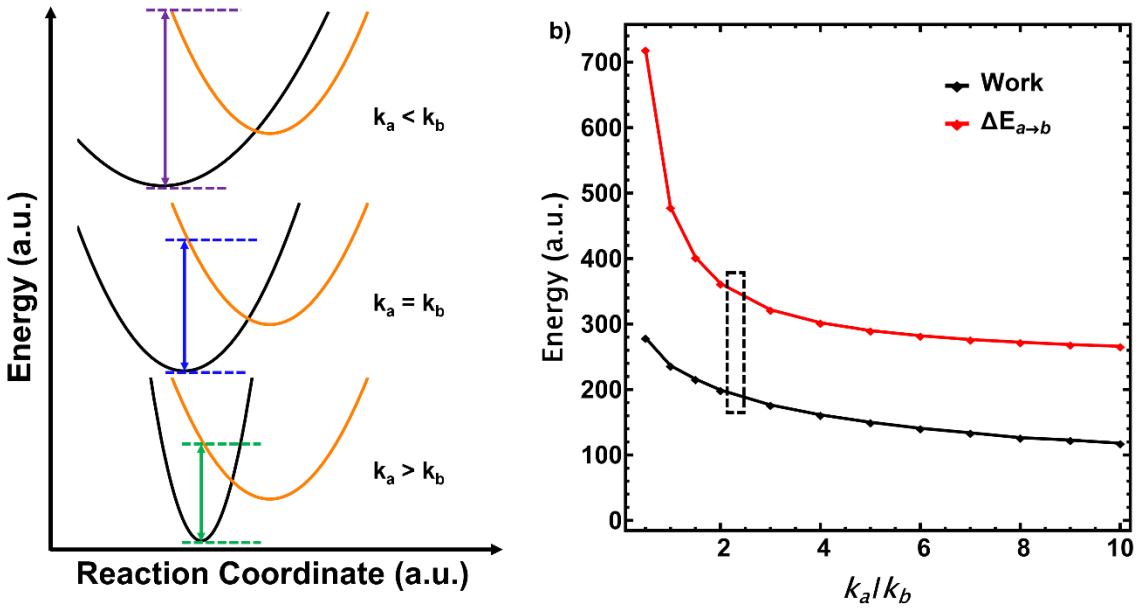

Figure 5.7 (a) Illustration of how changes in k_a/k_b lead to different $\Delta E_{a\to b}$ energy gaps. Both the energy cost and work output decrease as the k_a/k_b ratio increases, but at different rates, leading to the maximum in the efficiency seen in Figure 5. **(b)** Plots of the available work (black) and photon cost $\Delta E_{a\to b}$ (red) as k_a/k_b increases for $x_0 = 11$, $V = 0$, and $\Delta = 0$. The photon cost asymptotically approaches 250 a.u. as k_a/k_b increases, while the work continues to decrease and reduces the one-way efficiency at higher ratios of k_a/k_b. The maximum efficiency occurs in the dashed region ($k_a/k_b = 2.315$) where the photon cost has decreased more rapidly than the work output.

The origin of the higher η_{stop} values for $k_a/k_b > 1$ lies in the modified optical properties, rather than the increased force generation. The lower k_b value reduces the photon energy required to make the transition between $|a\rangle$ and $|b\rangle$ surfaces, as illustrated in Figure 6a. The different dependences of (eqn. 5.9 and (eqn. 5.10 on the force constants k_a and k_b means that it is possible to dramatically reduce the cost of the $\Delta E_{a\to b}$ photon by lowering k_b while only slightly decreasing the work output. Once k_b is much smaller than k_a, however, both the work output and photon input energies decline at the same rate. This can be seen from a plot of the $W_{a\to b}$ and $\Delta E_{a\to b}$ values as a function of the k_a/k_b ratio, shown in **Figure 5.7b**. The 10% gain in photon-to-work efficiency for $k_a > k_b$ provides a hint that

the work output can be enhanced by tuning the molecular vibrational structure. Previous workers have established that vibrational structure and coherence near conical intersections can have a large impact the quantum yield of a photochemical reaction[26-28] The results presented here assume that the photochemical quantum yield is unity, so the photon-to-work efficiency reflects how vibrational structure affects the light absorption process which occurs far from this type of intersection of the harmonic surfaces. In a real system, the effects of molecular vibrational structure on both the conical intersection and the absorption energy will both have to be considered in order to accurately calculate the overall photon-to-work efficiency.

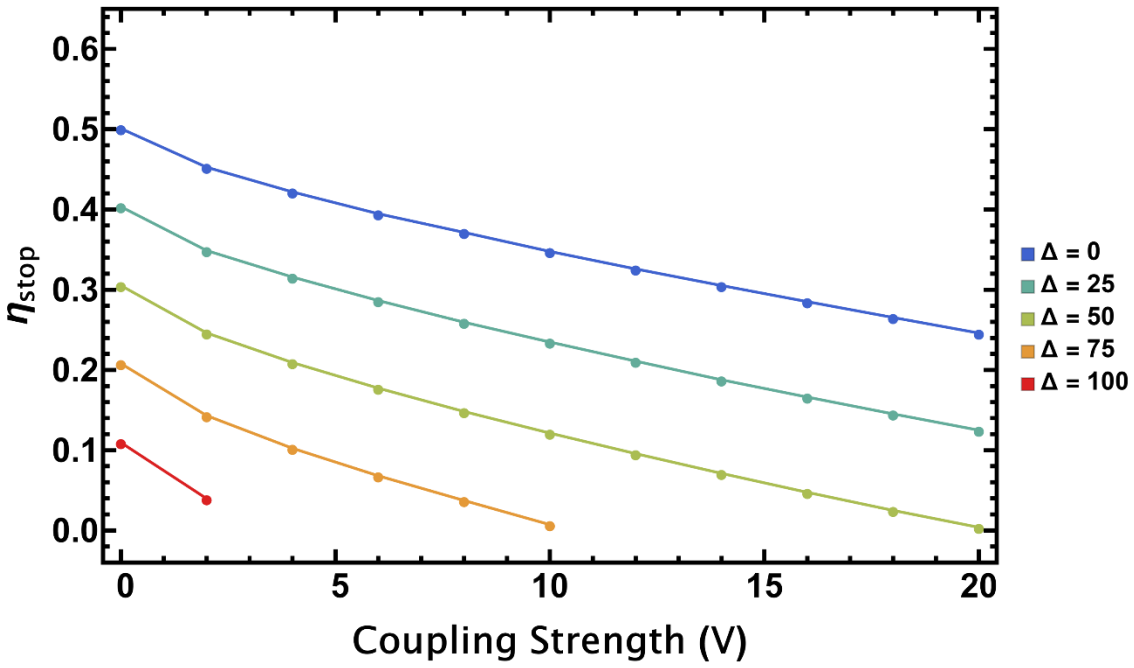

Figure 5.8 The photomechanical efficiency η_{stop} is plotted as a function of the electronic coupling V for various Δ values. For these calculations, $x_0 = 5$ and $k_a = k_b = 1$. Note that larger V couplings and Δ values result in smaller A_{stop} and thus η_{stop} values as the ground state barrier decreases.

If $V \neq 0$, the A_{stop} and η_{stop} values can be evaluated numerically by iteratively solving (eqn. 5.3, (eqn. 5.12, and (eqn. 5.13. Details are given in section **2.3.1**. The effect of V on η_{stop} is shown in **Figure 5.8**, which plots η_{stop} as a function of V for different values of Δ. In all cases, increasing V leads to a roughly linear decrease in η_{stop}. This can be understood as a consequence of the nonadiabatic coupling leading to a lowered activation barrier on the adiabatic ground state surface, which in turn lowers A_{stop}. At large V values, the second minimum at x_b disappears, preventing the calculation of η_{stop} values.

Finally, we consider the cycling efficiency of the 1D coupled harmonic system. We have already evaluated the efficiency in the $|a\rangle \rightarrow |b\rangle$ direction. The return $|b\rangle \rightarrow |a\rangle$ stroke does not contribute to the work against the applied force but does require extra photon energy, so the efficiency will always be decreased. In this case, the overall efficiency of the $|a\rangle \rightarrow |b\rangle \rightarrow |a\rangle$ cycle is just

$$\eta_{cycle} = \frac{W_{a\rightarrow b}}{\Delta E_{a\rightarrow b} + \Delta E_{b\rightarrow a}}$$

(eqn. 5.16)

We consider the case of $\Delta \geq 0$, where the starting state $|a\rangle$ is the lowest energy isomer. At the maximum η_{stop}, the $|a\rangle$ PES curve intersects the minimum of the $|b\rangle$ PES curve, and the photon energy required to make the $|b\rangle \rightarrow |a\rangle$ transition becomes negligible. In this case, the maximum $\eta_{cycle} = \eta_{stop} = 0.554$ for $k_a/k_b = 2.315$. This analysis indicates that the highest cycle efficiency will be attained for T-type materials, since in practice this return transition would be accomplished by thermal excitation rather than an optical photon. Lower A

values not only lead to lower forward $|a\rangle \rightarrow |b\rangle$ efficiencies but also require additional input photon energy to return the system from $|b\rangle$ to $|a\rangle$.

There are several reasons that the analysis presented above should be considered an upper limit for photomechanical efficiencies in real systems. First, we only considered the T = 0 K limit. When $\Delta E^{\ddagger} < kT$ we can expect thermal fluctuations to effectively remove the stationary point at the $|b\rangle$ curve minimum. In practice, this would lower A_{stop} and thus η_{stop}. Second, we have assumed that the photochemical quantum yield for the $|a\rangle \rightarrow |b\rangle$ reaction is unity. The efficiencies calculated above should be multiplied by a quantum yield factor that in practice is always less than 1.0 due to both radiative and nonradiative decay channels. Third, we have only considered a 1D system with coupled product-reactant modes. In a polyatomic molecule with many modes oriented orthogonal to the reaction coordinate, e.g. azobenzene[29-31], much of the input photon energy will be dissipated into vibrations that are not aligned with the applied force, further decreasing the efficiency.

How efficient could a molecular photoisomerization be in practice? Gaub and coworkers investigated the photomechanical response of single oligomer chains composed of azobenzene repeat units attached to an atomic force microscope tip. In these experiments, the applied force was not aligned with the cis-trans reaction coordinate, which is usually taken to be the C-N-N dihedral angle. Even given this misalignment, however, measurements of the chain contraction under load yielded an absorbed photon-to-work efficiency of 0.1 for a trans→cis photoisomerization.[32] This value is actually not far from the single-molecule theoretical limit derived in this chapter. However, once quantum

yields, absorption cross sections, and light propagation were taken into account, the calculated incident photon-to-work efficiency was estimated to be 7.5×10^{-6}.[33] Photomechanical crystals composed purely of photoactive molecules typically exhibit absorbed photon-to-work efficiencies of less than 1%.[34, 35], as do most polymer systems.[36] The large gap between the theoretical molecular limit and the measured efficiencies of suggests that there remains a substantial room to improve these materials.

The results presented above suggest that directional application of force could result in changes in molecular optical properties. Although redshifts are commonly observed in high pressure experiments, they usually result from changes in the medium polarizability due to increased density.[37, 38] When the molecular PESs are distorted by the application of a directional force, our model predicts a blueshift of the $|a\rangle\rightarrow|b\rangle$ absorption and a redshift of the $|b\rangle\rightarrow|a\rangle$ fluorescence. Although challenging, the measurement of optical properties during the directional pulling of single molecules could reveal the PES deformations illustrated in **Figure 5.2**. If applying a force leads to substantial absorption shifts, then a fruitful area for improving photomechanical materials might involve tuning of reactant-product vibrational structures to enhance efficiency. The fact that even in this simple model the maximum efficiency does not occur for $k_a/k_b = 1.0$ suggests that careful consideration of how molecular vibrations affect both photon absorption and mechanical response properties may be necessary to optimize these materials.

Lastly, we can compare molecular photomechanical elements to photovoltaic approaches for transforming photon energy into work. At 0 K and given an input photon at the semiconductor band edge, the photovoltaic energy conversion efficiency can

approach 1.0.[39] Piezoelectric actuators have a maximum electrical-to-mechanical conversion efficiency of 0.5 [40], so assuming no electrical losses, the PV-piezoelectric approach would yield an overall efficiency of 1.0 × 0.5 = 0.5. If the PV cell is attached to a DC electric motor, whose electrical-to-mechanical efficiency can approach 1.0[41], then the photon-to-work efficiency will also approach 1.0. Our results show that the photomechanical approach can be competitive with either photovoltaic approach in terms of theoretical efficiency. The photomechanical approach possesses several potential advantages, however, including 1) simplicity, since only a single element with no connections is required; 2) insensitivity to electromagnetic fields, since no free carriers are generated; 3) fast response, since the molecular shape change follows the photoisomerization time, which can be on the order of picoseconds. For a given application, the best approach will likely be determined by factors like device size, environment, and the available light source. It should be emphasized that the field of photomechanical materials is still relatively young compared to the fields of electromagnetic actuators and photovoltaics, so considerable improvement may be expected.

5.3 Conclusion

The simple 1-D model in this chapter represents a preliminary step in the development of a molecular model for the photomechanical process. It provides a way to estimate mechanical outputs like the stop-force, work, and efficiency from molecular parameters like vibrational frequencies, reaction coordinates, and electronic couplings. A central

result is that the theoretical photon-to-work efficiency of a molecule is comparable to that of photovoltaic devices. A second result is that the maximum efficiency is obtained when $k_a > k_b$, showing that the interplay between force-induced changes in the optical as well as the mechanical properties must be considered in the design of such molecules. It is hoped that this work will motivate more sophisticated theoretical studies and materials design that enable bulk photomechanical systems to approach the molecular performance limits.

5.4 References

(1) White, T. J. Photomechanical Materials, Composites, and Systems. 1 ed.; Wiley: Hoboken, New Jersey, 2017.

(2) Koshima, H. Mechanically Responsive Materials for Soft Robotics. Wiley: Weinheim, Germany, 2020.

(3) Kuzyk, M. G.; Dawson, N. J. Photomechanical materials and applications: a tutorial. *Adv. Optics Photonics* **2020**, *12*, 847-1011. DOI: 10.1364/AOP.387366.

(4) Han, B.; Zhang, Y.-L.; Chen, Q.-D.; Sun, H.-B. Carbon-Based Photothermal Actuators. *Adv. Funct. Mater.* **2018**, 1802235. DOI: 10.1002/adfm.201802235.

(5) Lui, B. F.; Bardeen, C. J. Using Small Molecule Absorbers to Create a Photothermal Wax Motor. *Small* **2021**, 2105356. DOI: 10.1002/smll.202105356.

(6) Hasebe, S.; Hagiwara, Y.; Komiya, J.; Ryu, M.; Fujisawa, H.; Morikawa, J.; Katayama, T.; Yamanaka, D.; Furube, A.; Sato, H.; et al. Photothermally Driven High-Speed Crystal Actuation and Its Simulation. *J. Am. Chem. Soc.* **2021**, *143*, 8866−8877. DOI: 10.1021/jacs.1c03588.

(7) Kundys, B. Photostrictive materials. *Appl. Phys. Rev.* **2015**, *2*, 011301. DOI: 10.1063/1.4905505.

(8) Kim, T.; Zhu, L.; Al-Kaysi, R. O.; Bardeen, C. J. Organic photomechanical materials. *ChemPhysChem* **2014**, *15*, 400-414. DOI: 10.1002/cphc.201300906.

(9) Ikeda, T.; Mamiya, J.-i.; Yu, Y. Photomechanics of liquid-crystalline elastomers and other polymers. *Angew. Chem. Int. Ed.* **2007**, *46*, 506-528. DOI: 10.1002/anie.200602372.

(10) Priimagi, A.; Barrett, C. J.; Shishido, A. Recent twists in photoactuation and photoalignment control. *J. Mater. Chem. C* **2014**, *2*, 7155-7162. DOI: 10.1039/C4TC01236D.

(11) White, T. J. Photomechanical Effects in Liquid Crystalline Polymer Networks and Elastomers. *J. Polym. Sci. B* **2018**, *56*, 695–705. DOI: 10.1002/polb.24576.

(12) Al-Kaysi, R. O.; Muller, A. M.; Bardeen, C. J. Photochemically driven shape changes of crystalline organic nanorods. *J. Am. Chem. Soc.* **2006**, *128*, 15938-15939.

(13) Kobatake, S.; Takami, S.; Muto, H.; Ishikawa, T.; Irie, M. Rapid and reversible shape changes of molecular crystals on photoirradiation. *Nature* **2007**, *446*, 778-781.

(14) Koshima, H.; Ojima, N.; Uchimoto, H. Mechanical motion of azobenzene crystals upon photoirradiation. *J. Am. Chem. Soc.* **2009**, *131*, 6890-6891.

(15) Bushuyev, O. S.; Tomberg, A.; Friscic, T.; Barrett, C. J. Shaping Crystals with Light: Crystal-to-Crystal Isomerization and Photomechanical Effect in Fluorinated Azobenzenes. *J. Am. Chem. Soc.* **2013**, *135*, 12556-12559.

(16) Nath, N. K.; Pejov, L. o.; Nichols, S. M.; Hu, C.; Saleh, N. i.; Kahr, B.; Naumov, P. e. Model for Photoinduced Bending of Slender Molecular Crystals. *J. Am. Chem. Soc.* **2014**, *136*, 2757−2766. DOI: 10.1021/ja4101497.

(17) Wang, H.; Chen, P.; Wu, Z.; Zhao, J.; Sun, J.; Lu, R. Bending, Curling, Rolling, and Salient Behavior of Molecular Crystals Driven by [2+2] Cycloaddition of a Styrylbenzoxazole Derivative. *Angew. Chem. Int. Ed.* **2017**, *56*, 9463 –9467.

(18) Durr, H.; Bouas-Laurent, H. *Photochromism : Molecules and Systems*; Elsevier, 1990.

(19) Kitagawa, D.; Kobatake, S. Strategy for Molecular Design of Photochromic Diarylethenes Having Thermal Functionality. *Chem. Rec.* **2016**, *16*, 2005–2015. DOI: 10.1002/tcr.201600060.

(20) Bell, G. I. Models for the Specific Adhesion of Cells to Cells. *Science* **1978**, *200*, 618-627. DOI: 10.1126/science.347575.

(21) Barbara, P. F.; Meyer, T. J.; Ratner, M. A. Contemporary Issues in Electron Transfer Research. *J. Phys. Chem.* **1996**, *100*, 13148-13168. DOI: 10.1021/jp9605663.

(22) Benderskii, V. A.; Vetoshkin, E. V.; Kats, E. I.; Trommsdorff, H. P. A semiclassical 1D model of ultrafast photoisomerization reactions. *Chem. Phys. Lett.* **2005**, *409*, 240-244. DOI: 10.1016_j.cplett.2005.05.025.

(23) Beyer, M. K.; Clausen-Schaumann, H. Mechanochemistry: The Mechanical Activation of Covalent Bonds. *Chem. Rev.* **2005**, *105*, 2921-2948. DOI: 10.1021/cr030697h.

(24) Evans, E.; Ritchie, K. Dynamic Strength of Molecular Adhesion Bonds. *Biophys. J.* **1997**, *72*, 1541-1555. DOI: 10.1016/S0006-3495(97)78802-7.

(25) Ribas-Arino, J.; Marx, D. Covalent Mechanochemistry: Theoretical Concepts and Computational Tools with Applications to Molecular Nanomechanics. *Chem. Rev.* **2012**, *112*, 5412−5487. DOI: 10.1021/cr200399q.

(26) Malhado, J. P.; Hynes, J. T. Photoisomerization for a model protonated Schiff base in solution: Sloped/peaked conical intersection perspective. *J. Chem. Phys.* **2012**, *137*, 22A543. DOI: 10.1063/1.4754505.

(27) Levine, B. G.; Martınez, T. J. Isomerization through conical intersections. *Ann. Rev. Phys. Chem.* **2007**, *58*, 613-634. DOI: 10.1146/annurev.physchem.57.032905.104612.

(28) Duan, H.-G.; Miller, R. J. D.; Thorwart, M. Impact of Vibrational Coherence on the Quantum Yield at a Conical Intersection. *J. Phys. Chem. Lett.* **2016**, *7*, 3491−3496. DOI: 10.1021/acs.jpclett.6b01551.

(29) Yu, J. K.; Bannwarth, C.; Liang, R.; Hohenstein, E. G.; Martínez, T. J. Nonadiabatic Dynamics Simulation of the Wavelength-Dependent Photochemistry of Azobenzene Excited to the nπ* and ππ* Excited States. *J. Am. Chem. Soc.* **2020**, *142*, 20680−20690. DOI: 10.1021/jacs.0c09056.

(30) Aleotti, F.; Soprani, L.; Nenov, A.; Berardi, R.; Arcioni, A.; Zannoni, C.; Garavelli, M. Multidimensional Potential Energy Surfaces Resolved at the RASPT2 Level for Accurate Photoinduced Isomerization Dynamics of Azobenzene. *J. Chem. Theory Comput.* **2019**, *15*, 6813−6823. DOI: 10.1021/acs.jctc.9b00561.

(31) Crecca, C. R.; Roitberg, A. E. Theoretical Study of the Isomerization Mechanism of Azobenzene and Disubstituted Azobenzene Derivatives. *J. Phys. Chem. A* **2006**, *110*, 8188-8203. DOI: 10.1021/jp057413c.

(32) Hugel, T.; Holland, N. B.; Cattani, A.; Moroder, L.; Seitz, M.; Gaub, H. E. Single-Molecule Optomechanical Cycle. *Science* **2002**, *296*, 1103-1106. DOI: 10.1126/science.1069856.

(33) Holland, N. B.; Hugel, T.; Neuert, G.; Cattani-Scholz, A.; Renner, C.; Oesterhelt, D.; Moroder, L.; Seitz, M.; Gaub, H. E. Single Molecule Force Spectroscopy of Azobenzene Polymers: Switching Elasticity of Single Photochromic Macromolecules. *Macromolecules* **2003**, *36*, 2015-2023. DOI: 10.1021/ma021139s.

(34) Dong, X.; Tong, F.; Hanson, K. M.; Al-Kaysi, R. O.; Kitagawa, D.; Kobatake, S.; Bardeen, C. J. Hybrid Organic-Inorganic Photon Powered Actuators Based on Aligned Diaryethene Nanocrystals. *Chem. Mater.* **2019**, *31*, 1016-1022. DOI: 10.1021/acs.chemmater.8b04568.

(35) Halabia, J. M.; Ahmeda, E.; Sofelab, S.; Naumov, P. Performance of molecular crystals in conversion of light to mechanical work. *Proc. Nat. Acad. Sci.* **2021**, *118*, e2020604118. DOI: 10.1073/pnas.2020604118.

(36) Cheng, L.; Torres, Y.; Lee, K. M.; McClung, A. J.; Baur, J.; White, T. J.; Oates, W. S. Photomechanical bending mechanics of polydomain azobenzene liquid crystal polymer network films. *J. Appl. Phys.* **2012**, *112*, 013513. DOI: 10.1063/1.4729771.

(37) Okamoto, B. Y.; Drickamer, H. G. High Pressure Studies of Solvent Effects on Anthracene Spectra. *Proc. Nat. Acad. Sci.* **1974**, *71*, 4757-4759. DOI: 10.1073/pnas.71.12.4757.

(38) Robertson, W. W.; King, A. D. Calculation of Pressure Shifts of Optical Absorption Spectra from Solvent Data. *J. Chem. Phys.* **1961**, *34*, 1511-1515. DOI: 10.1063/1.1701037.

(39) (Muller), M. F.; Freunek, M.; Reindl, L. M. Maximum Efficiencies of Indoor Photovoltaic Devices. *IEEE J. Photovoltaics* **2013**, *3*, 59-64. DOI: 10.1109/JPHOTOV.2012.2225023.

(40) Blackburn, J. F.; Cain, M. G. Coupling efficiency in piezoelectric actuators with direct current and alternating current excitation. *J. Appl. Phys.* **2013**, *113*, 184101. DOI: 10.1063/1.4803480.

(41) Almeida, A. T. d.; Ferreira, F. J. T. E.; Fong, J. A. C. Standards for Efficiency of Electric Motors. *IEEE Ind. Appl. Mag.* **2011**, *17*, 12-19. DOI: 10.1109/MIAS.2010.939427.

Chapter 6. Photomechanical Structures Based on Porous Alumina Templates Filled with 9-Methylanthracene Nanowires

Now that we've established a basis for modelling photomechanical molecules, the next step in implementing photomechanical organic crystals into practical devices is to develop a linear actuator that is analogous to piezoelectric stacking actuators. In this chapter, we will explore the use of a negative photochrome that is capable of ≈ 7% expansion along the long axis in nanorods of the crystal. Using our templated composite approach to photomechanical actuation, we demonstrate the drawbacks of brittle porous membranes and develop a recipe for optimal solvent annealing of organic crystals when filling porous templates.

6.1 Introduction

Photomechanical materials are designed to directly transform light into mechanical work[1, 2]. Most organic photomechanical crystals and polymers rely on a photochemical mechanism, such as the cis-trans photoisomerization of azobenzene[3], in order to generate this work. In order to efficiently generate macroscopic amounts of work, the photoreactive molecules (photochromes) must be organized in some way[4]. This organization is accomplished in a polymeric matrix by incorporating the photochrome into a liquid crystal elastomer[5]. The use of a polymer matrix allows the facile creation of differently sized and shaped structures using well-established methods such as molding and photolithography. Alternatively, the photochromes can order by self-assembling into a neat molecular crystal[6-15]. The potential advantages of photomechanical crystals include their higher photochrome density and elastic modulus[16]. Unlike in the case of polymers, however,

controlling the morphology of single crystals is very challenging and typically a broad distribution of sizes and shapes is obtained. Furthermore, molecular crystals are prone to fracture due to the internal stress that is generated by the build-up of photoproduct regions, especially if the crystals are larger than a few microns[6, 17, 18]. They also tend to dissolve or degrade when exposed to organic solvents or air, respectively; although attempts to encase crystals in protective layers of graphene[19], polymers[20], or metal organic frameworks[21] have had some success. Given these challenges, it is not obvious how to incorporate single crystals into practical actuator devices, despite their potential advantages.

We recently developed a composite approach to photomechanical materials in which the organic crystal component is organized inside a porous inorganic host[22, 23]. The host material was a commercially produced anodic aluminum oxide (AAO) disk with nominal 200 nm diameter channels that permitted the growth of oriented crystalline nanowires. By using diarylethene photochromes that undergo a ring-closing isomerization[24], the photoreaction of the organic component resulted in the composite structure undergoing a reversible bending motion. A milligram of this organic could reversibly lift 10 g or more. The bending templates are based on a bimorph structure of which the bottom part is converted into photoproduct while the top part remains unreacted (**Figure 6.1a**). The strain between the reactant and product domains leads to in-plane stress that is alleviated by bending. This mechanism of actuation was necessitated by the fact that only a thin layer near the surface could be isomerized by the input light. Diarylethene is a "positive" photochrome whose ring-closed isomer strongly absorbs the UV radiation, preventing it from penetrating throughout the template. If 100% conversion of the organic component

could be achieved, it could enable different modes of actuation. For example, if the conversion of the organic component leads to crystal expansion, this could be utilized to make a composite in which the nanowires generate a concerted upward push (**Figure 6.1b**), rather than bending.

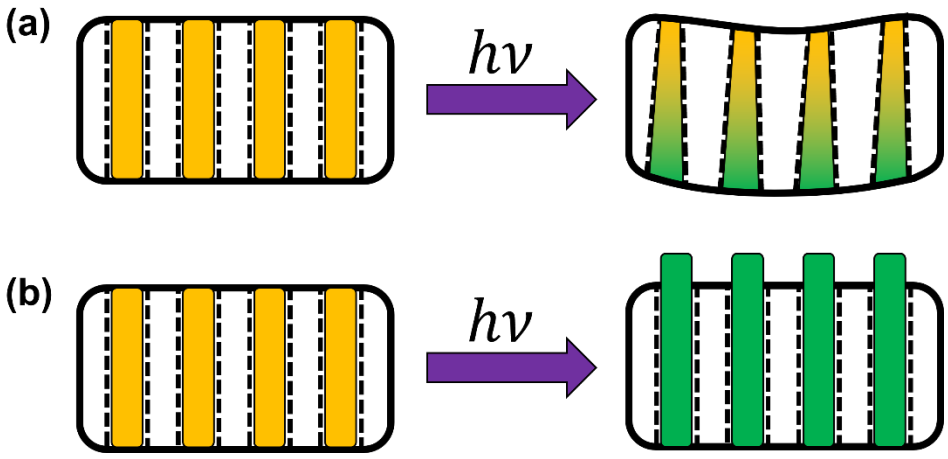

Figure 6.1 Schematic representation of the two possible methods of actuation in the organic-template system, (a) partial reaction of the crystal causing a change in curvature of the template and (b) full reaction of the crystal causing extension of organic nanorods through the surface of the template.

In order to create the composite photomechanical structure that is outlined in **Figure 6.1b**, several challenges must be overcome. First, the template must be completely filled with the organic, since any void spaces would serve to absorb the expansion inside of the channels, rather than forcing it outside of the template. Second, a "negative" photochromic reaction is required in order to allow the reaction to proceed to 100% completion[25], since a photoproduct that absorbs the excitation light will prevent it from reaching the unreacted portions of the sample, resulting in a bending bimorph as seen for the diarylethene reaction. Finally, the organic crystal must grow in an orientation that allows it to expand along the pore axis and not perpendicular to it.

In this chapter, we describe our efforts to realize the actuator structure that is shown in **Figure 6.1b** by utilizing crystalline 9-methylanthracene (9MA), a prototypical photomechanical material whose crystal structure, growth habits, and reactivity have been extensively characterized by our group and others[26-31]. Our goal is to fill AAO templates (Anodisc) with 9MA monomer and then convert it to its photodimer form. This conversion should result in an elongation along the monomer *c*-axis and the projection of this axis onto the nanowire axis should lead to a net increase in the height of the composite disk. It turns out that, in a real system, multiple nonidealities, including partial filling, crystal orientation, and debris from template polishing, all conspire to prevent the scenario that is illustrated in **Figure 6.1b** from being realized. While we observed template bending, showing that the photodimerization generates mechanical work, there was little sign of the surface disruption or vertical translation that would indicate that the wire elongation can be harnessed in order to create a linear translation. This chapter highlights some of the practical challenges that are involved in creating robust, reproducible actuators using the organic–inorganic composite approach, with the biggest one being how to uniformly fill the porous template with the organic active material. Future research directions which may be pursued in order to overcome these challenges are discussed.

6.2 Results and Discussion

The 9MA photodimerization reaction that provided the basis of the observed photo-mechanical response is shown in **Figure 6.2**. In order to grow crystalline 9MA nanowires in the AAO templates, we used a modified version of the slow solvent annealing method that has been developed previously[32] (see **Figure 2.1**). Briefly, the template was saturated with a concentrated solution of 9MA in CHCl3, then placed into a bell jar along with a variable amount of $CHCl_3$ solvent in a Kimwipe. The diffusion of the solvent vapor to the suspended template allowed the 9MA molecules to self-assemble in the AAO channels. After the solvent had completely evaporated from the bell jar (~24 h), the template was removed and polished so as to remove the excess 9MA that was on the surface. The resulting disk is the composite photomechanical material, but the inorganic AAO host can also be dissolved in a 20% aqueous H_3PO_4 acid solution in order to obtain isolated organic nanowires.

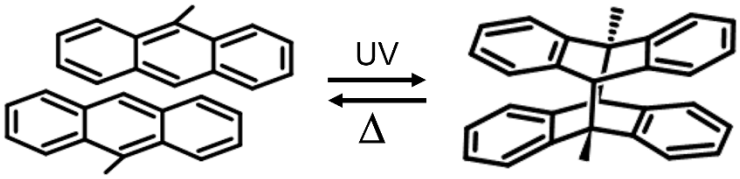

9-methylanthracene (9MA)

Figure 6.2 The [4 + 4] cycloaddition reaction that generates the 9MA photodimer after exposure to UV light. The reaction can be reversed by application of heat, but since 9MA sublimes readily at elevated temperatures it can be considered irreversible under ambient conditions.

The first question that we tried to address was whether the 9MA had completely filled the void space within the template. We determined the skeletal density of the Al_2O_3 in an empty template to be 3.0 ± 0.3 g/cm^3 (**Figure 2.10**). By measuring the mass and volume,

we calculated the void fraction to be 58% or 4.87×10^{-3} cm^3 out of a total disk volume of 7.96×10^{-3} cm^3, a result which is in good agreement with the previous estimates that have been reported in the literature[33]. Given the density of crystalline 9MA of 1.01 g/cm_3, this allowed us to estimate a maximum fill amount of 4.7 mg in a 12.7 mm diameter template. Using our standard solvent annealing Method 1 (in which 2000 μL of $CHCl_3$ was added to the Kimwipe), we only attained an average fill of 1.3 mg or 28%, as determined by the mass change of the filled template. Examination of the bell jar revealed that the excess solvent from the Kimwipe was condensing out of the vapor phase and redissolving the 9MA that had been deposited in the template. In some cases, the recondensed solvent was flowing back down to the bottom of the bell jar and bringing the 9MA with it. In order to minimize this effect, we reduced the amount of $CHCl_3$ that was added to the chamber from 2000 to 75 μL. This lower volume was the maximum amount that could completely fill the chamber volume of 180 cm^3 with vapor and avoid liquid condensation. Upon using this Method 2 with a lower volume of $CHCl_3$, we no longer observed solvent condensation or 9MA transport in the chamber. The average fill amount increased dramatically from 1.3 to 3.6 mg (77% of the maximum) after polishing.

In an attempt to further improve the filling of the AAO template, we functionalized the Al_2O_3 surface. Using a lauric acid treatment, we were able to make the surface more hydrophobic, increasing the H2O surface contact angle from 0° to >130° (**Figure 2.11**). This treatment visibly improved the wetting of the template during the initial deposition of the 9MA/$CHCl_3$ solution, but surprisingly it did not change the amount of filling to an extent that was outside the experimental error. This lack of effect for the surface treatment

was observed for both the high and low solvent exposure solvent annealing methods, as is summarized in **Figure 6.3**. The use of other carboxylic acid terminated molecules, like 3-phenylpropanoic acid, also had no discernible effect on the filling (**Figure 6.4**).

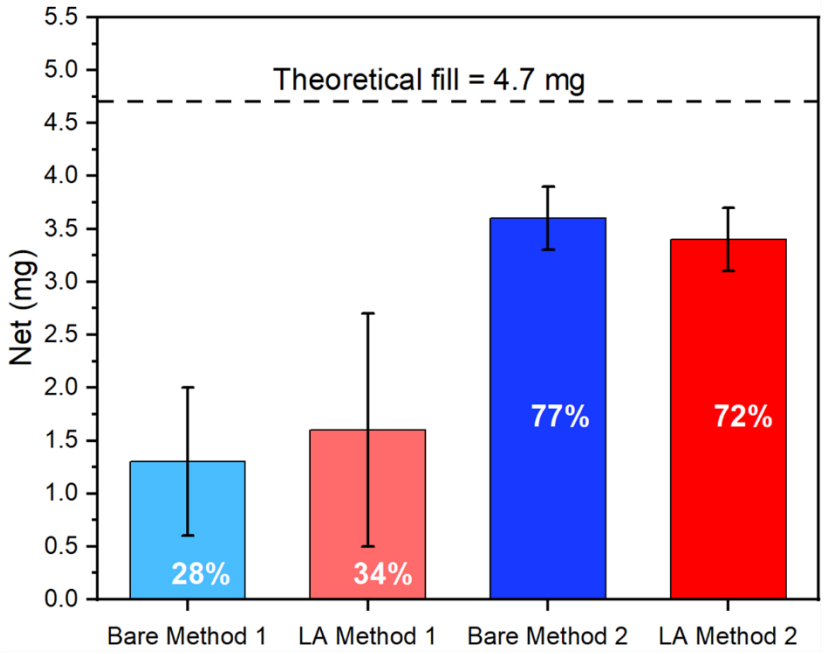

Figure 6.3 Measurements of the net mass of 9MA embedded in the AAO template after annealing and polishing. From left to right: light blue from using Method 1 (excess solvent) in a bare template, light red from using Method 1 with a lauric acid (LA) covered template, dark blue from using Method 2 (no excess solvent) in a bare template, and dark red from using Method 2 in an LA covered template. Surface functionalization of the AAO template had a negligible impact compared to the solvent annealing process.

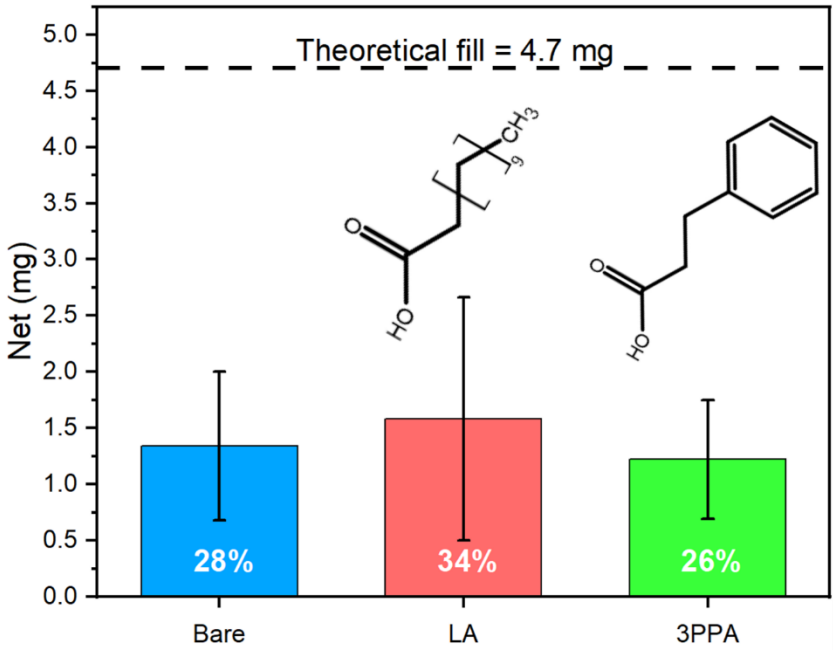

Figure 6.4 Comparison of the effect of surface functionalization on the AAO templates using the excess solvent method. Compared to the bare template, functionalizing the surface with lauric acid (LA) or 3-phenyl propanoic acid (3PPA) had a negligible effect outside of the margin of error.

After solvent annealing and polishing, GI-WAXS experiments on the filled templates were used in order to confirm that the 9MA was crystalline. The measured GI-WAXS pattern for a filled template, along with the assignment of the diffraction peaks, is shown in **Figure 6.5**. The GIWAXS experiment acquired diffraction information across a range of angles, so it was sensitive to crystal planes with different orientations with respect to the surface plane. Based on the measured pattern, b* is closely aligned with the surface normal and a* is about 13 degrees off of the film plane's direction (indicated by a white line). Therefore, c* in this case can be deduced to be almost parallel to the template's surface. Since the reciprocal axis c* and real crystal axis c are only 6 degrees away from each other, we conclude that the c-axis is also almost parallel to the template surface. The average

FWHM of the scattering peaks along the azimuthal direction in the samples is 3.7°, suggesting a high degree of alignment in relation to the film's normal direction.

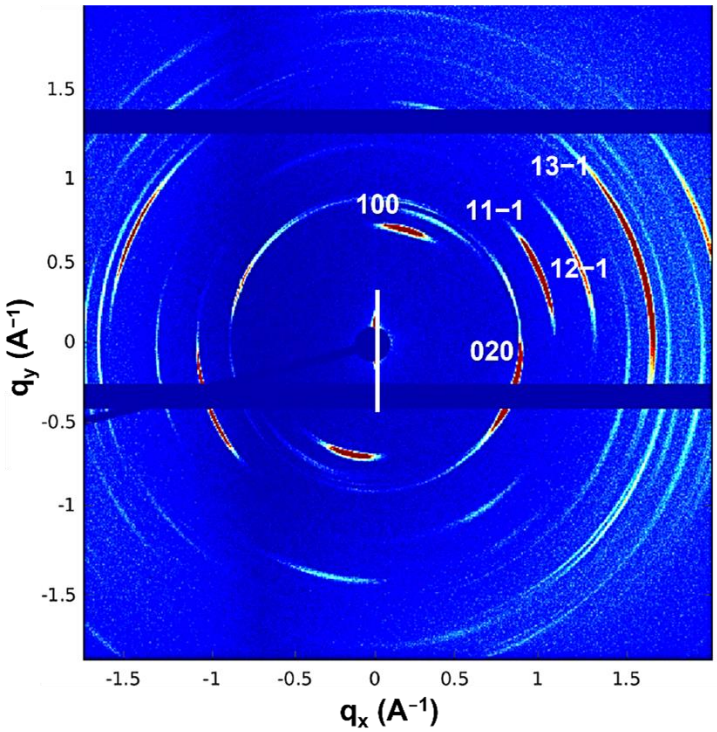

Figure 6.5 The GIWAXS pattern and accompanying face indexation for a 3 mm × 1 mm sample cut from a 9MA-filled template. The film plane direction is indicated by the white line near the origin. The FHWM of the scattering is 3.7° in the azithumal direction, indicating that the sample is highly oriented along the film normal and thus inside the pore axis.

Since the expansion of 9MA occurs along the c-axis[26, 31] and this axis is apparently oriented perpendicularly to the long axis of the nanowires (i.e., parallel to the template's surface), we were concerned about whether the nanowires would elongate after light exposure, as shown in **Figure 6.1b**. Examination of the isolated nanowires confirmed their photomechanical elongation. An example of an individual nanowire response is shown in **Figure 6.6**. The nanowire exhibited an expansion of ~7% along its long axis, similar to the 7% expansion seen for the microcrystal plates along the crystal c-axis[31]. The expansion

data and the GIWAXS data appeared to be contradictory, since the former is consistent with the nanowires growing along the c-axis, while the latter suggest that they grow perpendicular to the c-axis. However, this apparent contradiction assumes that polishing removes all of the excess surface crystallites and exposes only the vertically oriented nanorods that are embedded inside the AAO to the probing X-rays. As will be explained be-low, we found that the surface polishing procedure leaves a layer of mixed 9MA crystals and AAO debris on the surface, which probably makes a strong contribution to the observed GI-WAXS pattern.

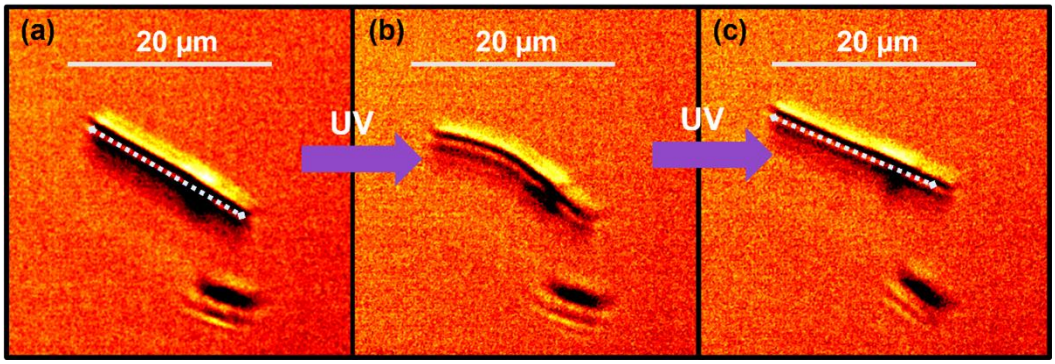

Figure 6.6 Optical microscope images of a 9MA nanorod suspended in aqueous solution **(a)** before, **(b)** during, and **(c)** after exposure to UV light. The nanorod extends roughly 7% along its long axis.

We next determined whether the negative photochromic reaction of the 9MA could enable 100% conversion inside the template. We assessed the conversion by exposing the template to varying durations of UV irradiation, followed by dissolving the organic component in a fixed volume of $CHCl_3$. The amount of the remaining 9MA could be determined using the Beer–Lambert law. We found that >98% of the initial 9MA monomer had disappeared after 24 h of 405 nm exposure, with most of the reaction having been completed within the first 5 h (**Figure 6.7**). This confirmed that the negative photochromic

reaction of 9MA could enable close to 100% conversion, even in the highly scattering AAO matrix.

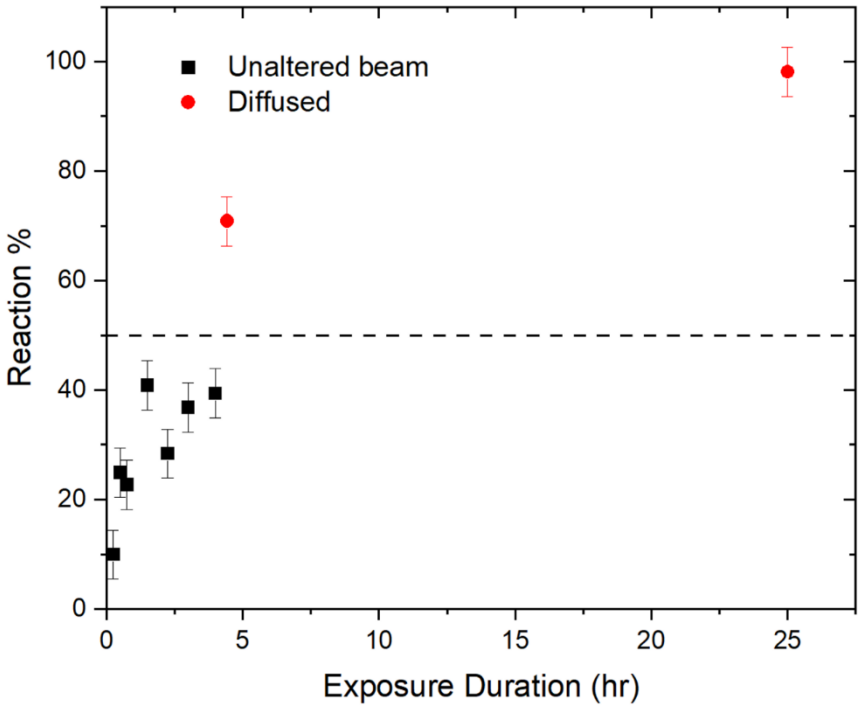

Figure 6.7 The percentage of the template that has been reacted when exposed to different durations of the UV source. In the first series, the beam spot size was approx. 96 mm^2 with a power density of ≈ 18 $\mu W/mm^2$. In the second series, the beam was expanded with a diffuser to complete cover the template at the sample stage with a power density of ≈ 19.5 $\mu W/mm^2$.

Having found a method to significantly improve the templates' fill fraction, although not up to 100%, we proceeded to measure their photomechanical responses. In order to be sensitive to micron-scale motions, we placed the template under one mirror in a Michelson interferometer. The irradiation of the supported template from the bottom resulted in the movement of a mirror on top of the template, as illustrated in **Figure 6.8a**. Pure translational motion would result in an oscillatory intensity pattern at the output due to constructive and destructive interference, while the angular tilting of the mirror can be measured by its spatial displacement from the reference beam. If the situation that is

illustrated in **Figure 6.1b** holds, we would expect to see pure translational motion as the nanowires extend above the template's surface. **Figure 6.8b** shows an example of the measured interferogram for a typical sample, along with images of the interferometer output before and after the irradiation. Both the interference and beam displacement are clearly present. The interferogram in **Figure 6.8b** can be modeled using the previously developed theory for interference signals in the presence of optical misalignment. In the experiments here, misalignment results from the photomechanical membrane moving one of the end mirrors. The equation for the integrated intensity at the interferometer output I_{photo} is given by[34, 35]:

$$I_{photo} = A^2 \pi w^2 \left(1 + \exp\left(\frac{-\left(k^2 w^4 + 4(L(t) - z)^2\right)\alpha(t)^2}{8w^2}\right) \times \cos\left(kL(t) + \frac{k}{2}(L(t) - z)\alpha(t)^2\right)\right) \quad \text{(eqn. 6.1)}$$

where w is the beam waist, k is the wave number of the probe, z is the distance to the detector, L is the optical path difference, and α is the angular off-set. For the calculations that are used in this chapter, $w = 1 \times 10^{-3}$ m, $k = 2\pi / 632.8 \times 10^{-9}$ m^{-1}, z = 1 m and we have neglected the factors due to the beam divergence and the Guoy phase shift. Neglecting these factors is justified when the beam diameter is much greater than the optical wavelength and there is no focusing inside the interferometer. Assuming a linear time dependence of the Δα and ΔL such that $L(t) = \Delta L(t - t_0)$ and $\alpha(t) = \Delta\alpha(t - t_0)$ where t_0 is the starting time for irradiation of the template, (eqn. 6.1) becomes:

$$I(t)=A^2\pi w^2\left(1+\exp\left(\frac{-\left(k^2w^4+4(\Delta L(t-t_0)-z)^2\right)\left(\Delta\alpha(t-t_0)\right)^2}{8w^2}\right)\times\cos\left(k\Delta L(t-t_0)+\frac{k}{2}(\Delta L(t-t_0)-z)\left(\Delta\alpha(t-t_0)\right)^2\right)\right)$$

(eqn. 6.2)

(eqn. 6.2) assumes that ΔL and $\Delta\alpha$ are independent, but if a circular template of diameter D tilts by an angle $\Delta\alpha$, then it can be shown that:

$$\Delta L(t)\approx\frac{D}{2}\times\Delta\alpha(t-t_0)$$

(eqn. 6.3)

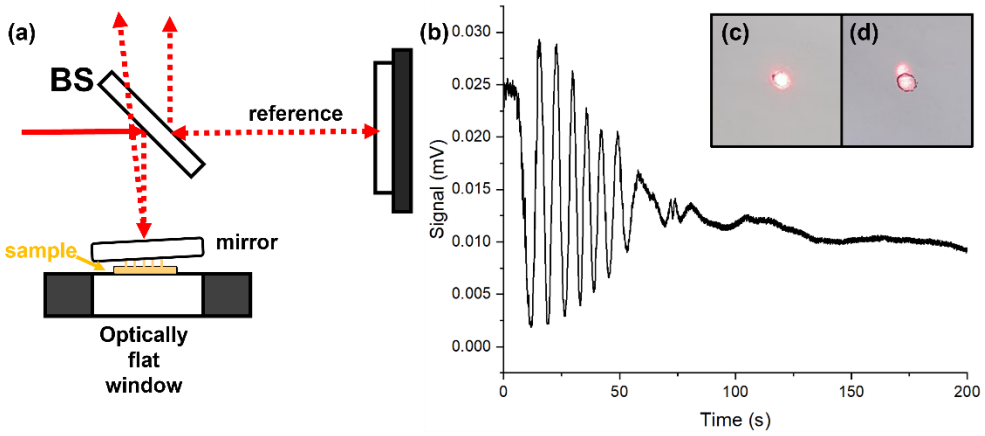

Figure 6.8 (a) Schematic of the interferometer set-up used to measure the photoinduced motion of the template. **(b)** Time-dependent photodiode signal from probe beams reflecting both interference and misalignment of probe beam due to angular tilt of the mirror during 405 nm irradiation. Complete misalignment causes a loss of signal that trends towards ≈50% of the maximum intensity. The insets capture the **(c)** initial and **(d)** final positions of the probe beam 4.9 m away from the sample due to the misalignment.

Using a value $\Delta\alpha = 4 \times 10^{-6}$ rad/s, (eqn. 6.2) can qualitatively reproduce the damped interferogram in **Figure 6.8b**, as shown in **Figure 6.9**. While there was considerable variability in the behavior of the filled templates (**Figure 6.10**), all of them showed some

combination of Δα and ΔL evolution. In general, the Δα tilting was the dominant effect, with the output beams having been displaced by about 0.51 mrad on average.

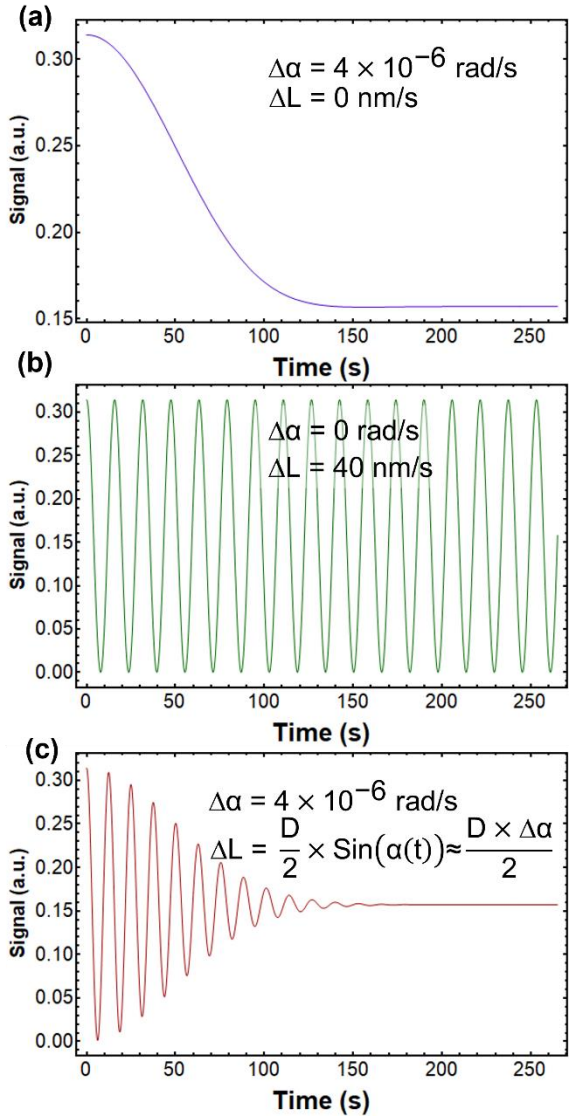

Figure 6.9 Simulated interferograms generated using eqn. 6.2 with the parameters listed in the figures. Patterns caused by changes in either **(a)** the angular error or **(b)** the optical path difference do not agree with the data in Figure 5. Only when **(c)** both parameters change is an interferogram that is comparable to that in Figure 5 obtained. ΔL and Δα are as described in the main text and D is the diameter of the AAO template.

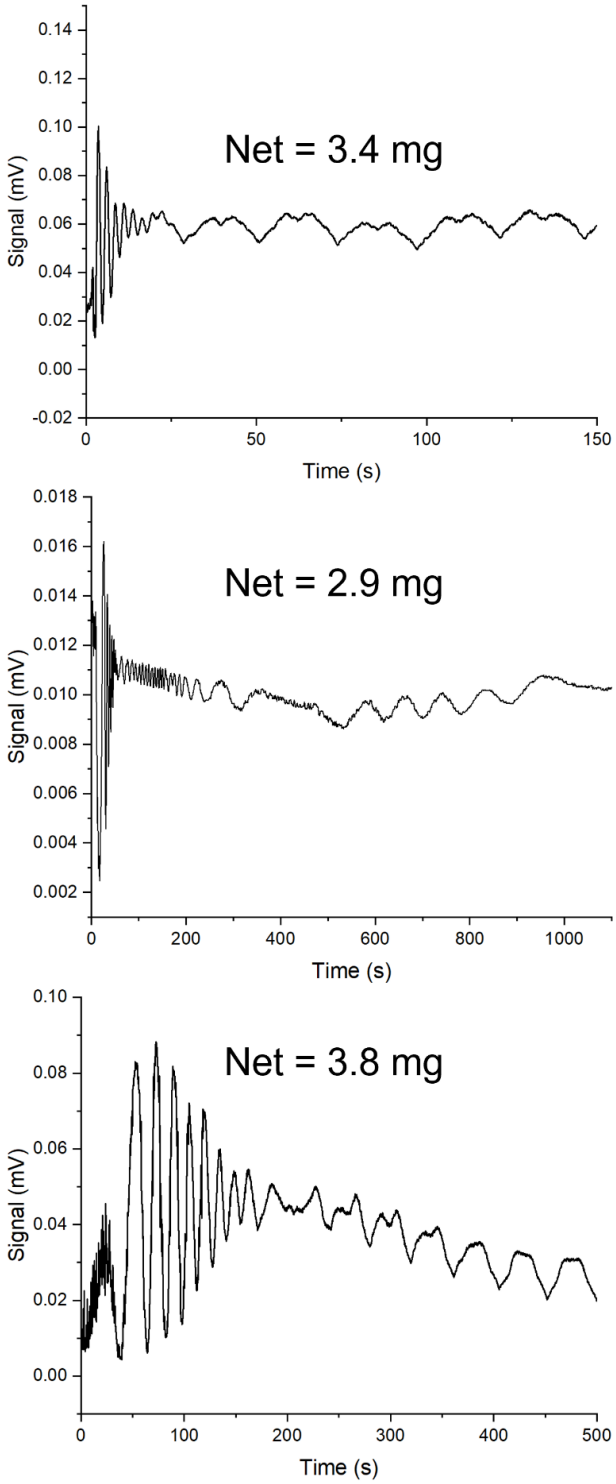

Figure 6.10 Example interferograms collected from three different templates filled with 9MA. The dominant behavior of each interferogram is the angular off-set building during the exposure duration, leading to the damping of the fringe heights. This angular error appears to vary significantly from sample to sample.

The analysis of the beams' deflection indicates that most of the mirror displacement arose from tilting and not translation. Closer examination of the template surface before and after UV irradiation using SEM and AFM confirmed the absence of any significant wire expansion above the template's surface. **Figure 6.12a,b** show AFM images of a template surface before and after UV irradiation. A few small changes are seen in the surface's morphology after UV exposure, but the overall features are remarkably similar. The lack of dramatic changes can be contrasted with the dramatic reconstruction that can be observed after 9MA single crystals undergo photoreaction[36]. For our samples, the surface features were not due to the presence of pure 9MA but instead appeared to be a rough crust of de-bris that was left over from the polishing process. This debris can be seen more clearly in SEM images of the templates before and after filling and polishing. The array of pores in the pristine template in **Figure 6.11a** is completely submerged under a layer that is composed of both AAO fragments and the organic in **Figure 6.11b**. Careful examination of this crust shows that it contains broken nanowires and AAO fragments that have been aligned to the horizontal plane by the polishing process (**Figure 6.11c**). Even though we used Al_2O_3 abrasives for most of the polishing process, the underlying AAO has clearly sustained notable damage.

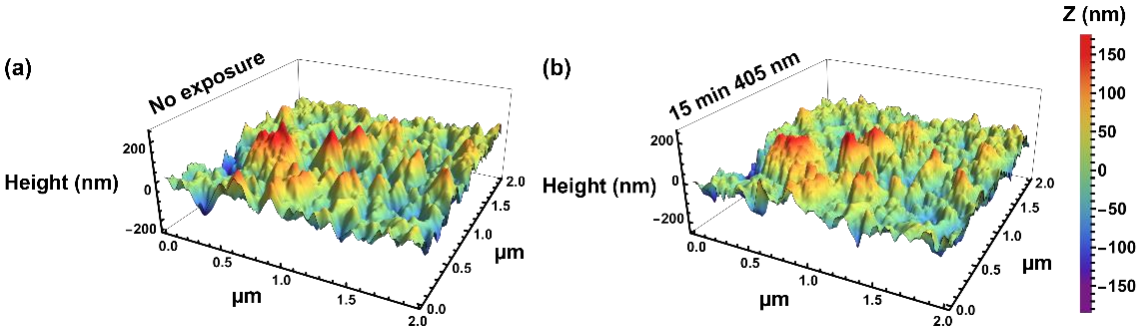

Figure 6.12 Atomic force microscope scan of a 9MA-filled template irradiated in-situ with a diffuse 405 nm laser. **(a)** before the 9MA was photo-dimerized and **(b)** after 15 min of exposure to 405 nm. There are slight changes in individual features but no obvious protrusions of nanowires from the surface.

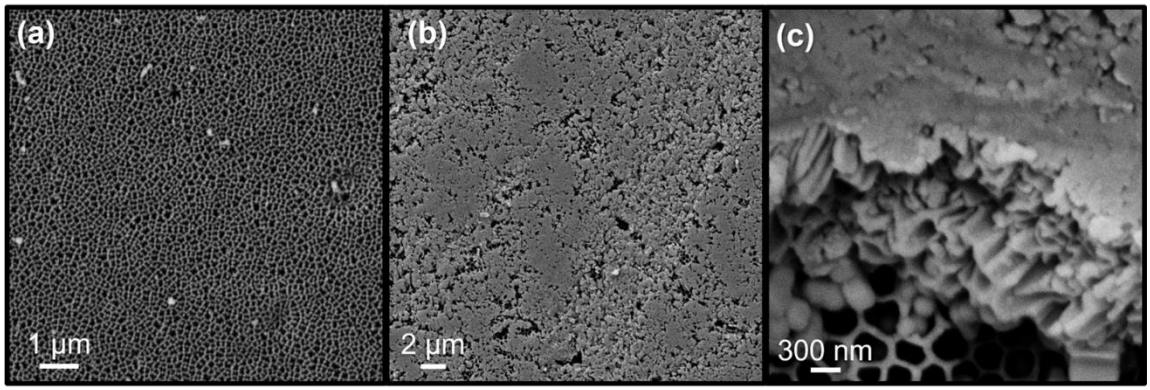

Figure 6.11 (a) SEM image of the pristine AAO surface in the absence of 9MA and polishing. **(b)** At low magnification, SEM image of the polished surface of a 9MA-filled template. **(c)** High magnification SEM image of the polished surface of a 9MA-filled template, showing surface debris that covers the channels and has been smoothed by polishing.

The combination of the void spaces inside the template that were due to incomplete filling and a surface debris layer may explain why we did not see nanowires expanding out of the template in order to act as linear actuators. Given the choice of protruding up from the template by breaking through the surface debris layer or extending down into empty spaces in the interior of the template, the expanding nanowires probably chose the path of least resistance. The presence of broken nanowires lying parallel to the surface also

explains why the GIWAXS measurements indicated that the crystal c-axis lay parallel to the template's surface. If the nanowires grow parallel to the c-axis, this axis should be normal to the template's surface for the vertical nanowires that are contained in the template. But if they are broken off and lie horizontal to the template surface, the c-axis would be in the direction that is indicated by the GIWAXS data. The presence of surface debris means that the GIWAXS experiment does not necessarily provide unambiguous information about the crystalline 9MA that is inside the template's pores, but it does confirm that the surface layer that was left by polishing is both crystalline and highly oriented. The surface debris that is left after polishing has complicated the analysis of powder X-ray diffraction experiments on other organic crystals in AAO templates as well[37, 38].

Although the negative photochromic reaction of crystalline 9MA can be used to generate the deformation of a composite membrane, we did not observe the purely vertical displacement that we had hoped for. However, sufficient lateral forces were generated to deform and bend the template. The origin of this horizontal stress component is not obvious, but several possible factors may have contributed. First, the horizontal surface layer was strongly attached to the template due to the force of polishing. Expansion along the c-axis of the horizontally oriented nanorods on the bottom of the template could drive some bending motion via the usual bimorph mechanism. Second, there may be a population of crystallites inside the template the c-axis of which is not perfectly aligned along the pore, which would allow the expansion to have some projection along the horizontal axis. Finally, the smaller changes in the dimensions of the a and b crystal axes [31] may provide

enough horizontal stress to slightly deform the template, irrespective of the c-axis expansion.

Our results highlight several challenges in the use of inorganic porous templates. First, it is difficult to achieve consistent, 100% filling using the solvent annealing method. Low filling fractions have also been found for the DAE photochrome in porous glass membranes, suggesting that this is a general problem. A completely different method of introducing the organic into the pores, perhaps melting the organic as opposed to using solvent annealing, might achieve higher filling but this may be more complicated to implement and may not lead to the same degree of crystallinity. Decreasing the thickness of the template and enlarging the pores may also facilitate organic filling. Although our simple surface functionalization did not improve the filling process, it is possible that a more sophisticated approach, perhaps using ligands that are tailored to the photochrome, could be more successful.

A second issue concerns the removal of the excess organic material that is left on the surface. For AAO, with a rough surface, we used high-grit polishing paper, but this method leaves a crust of dried slurry that can be several microns thick, as shown by the SEM images and the GIWAXS data. This crust can affect both the mechanical and light scattering properties. A gentler method that removes only the soft organic component would be desirable. Wiping the surface with a solvent soaked Kimwipe or cotton swab tended to remove the organic material from the surface and from inside the pores, so the right balance of mechanical and solvent forces must be found.

6.3 Conclusion

The results that are reported in this paper demonstrate that the photodimerization of 9MA can be used to power photomechanical motion in organic–inorganic hybrid actuator structures. A new experimental method for detecting motion, based on the analysis of a dynamically misaligned Michelson interferometer, has also been introduced. The results of this paper highlight the difficulties that are faced in the implementation of the organic–inorganic composite approach to photomechanical actuation. The reproducibility, linearity of motion, and overall response of the template were limited by our ability to completely fill the pores and remove debris from the surface. Taken together, the observations that are provided in this paper help to define the main challenges for the development of composite photomechanical materials that rely on molecular crystals as their active elements. Encouraging crystal growth in the porous host is a chemical problem, while re-moving excess organic material from the composite exterior is a materials processing problem. Both issues must be addressed in order to advance these composite materials toward practical applications as light-powered actuators.

6.4 References

(1) White, T. J. Photomechanical Effects in Materials, Composites, and Systems: Outlook and Future Challenges. In *Photomechanical Materials, Composites, and Systems*, John Wiley & Sons, Ltd: 2017; pp 393-403.

(2) Kuzyk, M. G.; Dawson, N. J. Photomechanical materials and applications: a tutorial. *Adv. Opt. Photon.* **2020**, *12* (4), 847. DOI: 10.1364/aop.387366.

(3) Taniguchi, T.; Asahi, T.; Koshima, H. Photomechanical Azobenzene Crystals. *Crystals* **2019**, *9* (9), 437. DOI: 10.3390/cryst9090437.

(4) Kim, T.; Zhu, L.; Al-Kaysi, R. O.; Bardeen, C. J. Organic Photomechanical Materials. *ChemPhysChem* **2014**, *15* (3), 400-414. DOI: 10.1002/cphc.201300906.

(5) Ikeda, T.; Mamiya, J.-i.; Yu, Y. Photomechanics of Liquid-Crystalline Elastomers and Other Polymers. *Angewandte Chemie International Edition* **2007**, *46* (4), 506-528. DOI: 10.1002/anie.200602372.

(6) Al-Kaysi, R. O.; Müller, A. M.; Bardeen, C. J. Photochemically Driven Shape Changes of Crystalline Organic Nanorods. *J Am Chem Soc* **2006**, *128* (50), 15938-15939. DOI: 10.1021/ja064535p.

(7) Kobatake, S.; Takami, S.; Muto, H.; Ishikawa, T.; Irie, M. Rapid and reversible shape changes of molecular crystals on photoirradiation. *Nature* **2007**, *446* (7137), 778-781. DOI: 10.1038/nature05669.

(8) Koshima, H.; Ojima, N.; Uchimoto, H. Mechanical Motion of Azobenzene Crystals upon Photoirradiation. *J Am Chem Soc* **2009**, *131* (20), 6890-6891. DOI: 10.1021/ja8098596.

(9) Morimoto, M.; Irie, M. A Diarylethene Cocrystal that Converts Light into Mechanical Work. *J Am Chem Soc* **2010**, *132* (40), 14172-14178. DOI: 10.1021/ja105356w.

(10) Naumov, P.; Kowalik, J.; Solntsev, K. M.; Baldridge, A.; Moon, J.-S.; Kranz, C.; Tolbert, L. M. Topochemistry and Photomechanical Effects in Crystals of Green Fluorescent Protein-like Chromophores: Effects of Hydrogen Bonding and Crystal Packing. *J Am Chem Soc* **2010**, *132* (16), 5845-5857. DOI: 10.1021/ja100844m.

(11) Bushuyev, O. S.; Tomberg, A.; Friščić, T.; Barrett, C. J. Shaping Crystals with Light: Crystal-to-Crystal Isomerization and Photomechanical Effect in Fluorinated Azobenzenes. *J Am Chem Soc* **2013**, *135* (34), 12556-12559. DOI: 10.1021/ja4063019.

(12) Nath, N. K.; Pejov, L.; Nichols, S. M.; Hu, C.; Saleh, N. i.; Kahr, B.; Naumov, P. Model for Photoinduced Bending of Slender Molecular Crystals. *J Am Chem Soc* **2014**, *136* (7), 2757-2766. DOI: 10.1021/ja4101497.

(13) Naumov, P.; Chizhik, S.; Panda, M. K.; Nath, N. K.; Boldyreva, E. Mechanically Responsive Molecular Crystals. *Chemical Reviews* **2015**, *115* (22), 12440-12490. DOI: 10.1021/acs.chemrev.5b00398.

(14) Wang, H.; Chen, P.; Wu, Z.; Zhao, J.; Sun, J.; Lu, R. Bending, Curling, Rolling, and Salient Behavior of Molecular Crystals Driven by [2+2] Cycloaddition of a Styrylbenzoxazole Derivative. *Angewandte Chemie International Edition* **2017**, *56* (32), 9463-9467. DOI: 10.1002/anie.201705325.

(15) Kitagawa, D.; Tsujioka, H.; Tong, F.; Dong, X.; Bardeen, C. J.; Kobatake, S. Control of Photomechanical Crystal Twisting by Illumination Direction. *J Am Chem Soc* **2018**, *140* (12), 4208-4212. DOI: 10.1021/jacs.7b13605.

(16) Spackman, P. R.; Grosjean, A.; Thomas, S. P.; Karothu, D. P.; Naumov, P.; Spackman, M. A. Quantifying Mechanical Properties of Molecular Crystals: A Critical Overview of Experimental Elastic Tensors. *Angewandte Chemie International Edition* **2021**, *61* (6). DOI: 10.1002/anie.202110716.

(17) Takahashi, S.; Miura, H.; Kasai, H.; Okada, S.; Oikawa, H.; Nakanishi, H. Single-Crystal-to-Single-Crystal Transformation of Diolefin Derivatives in Nanocrystals. *J Am Chem Soc* **2002**, *124* (37), 10944-10945. DOI: 10.1021/ja026564f.

(18) Bučar, D.-K.; MacGillivray, L. R. Preparation and Reactivity of Nanocrystalline Cocrystals Formed via Sonocrystallization. *J Am Chem Soc* **2006**, *129* (1), 32-33. DOI: 10.1021/ja0671161.

(19) Li, W.; Tierce, N. T.; Bekyarova, E.; Bardeen, C. J. Protection of Molecular Microcrystals by Encapsulation under Single-Layer Graphene. *ACS Omega* **2018**, *3* (7), 8129-8134. DOI: 10.1021/acsomega.8b00872 PubMed.

(20) Xu, P.; Yu, Q.; Chen, Y.; Cheng, P.; Zhang, Z. Protective Coating with Crystalline Shells to Fabricate Dual-Stimuli Responsive Actuators. *CCS Chemistry* **2022**, *4* (1), 205-213. DOI: 10.31635/ccschem.021.202000663.

(21) Chiba, H.; Morimoto, M.; Irie, M. Stepwise Assembly of Ultrathin Poly(vinyl alcohol) Films on Photoresponsive Diarylethene Crystals. *Chemistry Letters* **2021**, *50* (1), 84-86. DOI: 10.1246/cl.200693.

(22) Dong, X.; Tong, F.; Hanson, K. M.; Al-Kaysi, R. O.; Kitagawa, D.; Kobatake, S.; Bardeen, C. J. Hybrid Organic–Inorganic Photon-Powered Actuators Based on Aligned

Diarylethene Nanocrystals. *Chemistry of Materials* **2019**, *31* (3), 1016-1022. DOI: 10.1021/acs.chemmater.8b04568.

(23) Dong, X.; Guo, T.; Kitagawa, D.; Kobatake, S.; Palffy-Muhoray, P.; Bardeen, C. J. Effects of Template and Molecular Nanostructure on the Performance of Organic–Inorganic Photomechanical Actuator Membranes. *Advanced Functional Materials* **2019**, *30* (2), 1902396. DOI: 10.1002/adfm.201902396.

(24) Irie, M.; Fukaminato, T.; Matsuda, K.; Kobatake, S. Photochromism of Diarylethene Molecules and Crystals: Memories, Switches, and Actuators. *Chemical Reviews* **2014**, *114* (24), 12174-12277. DOI: 10.1021/cr500249p.

(25) Aiken, S.; Edgar, R. J. L.; Gabbutt, C. D.; Heron, B. M.; Hobson, P. A. Negatively photochromic organic compounds: Exploring the dark side. *Dyes and Pigments* **2018**, *149*, 92-121. DOI: 10.1016/j.dyepig.2017.09.057.

(26) Turowska-Tyrk, I.; Trzop, E. Monitoring structural transformations in crystals. 6. The [4 + 4] photodimerization of 9-methylanthracene. *Acta Crystallographica Section B Structural Science* **2003**, *59* (6), 779-786. DOI: 10.1107/s0108768103023255.

(27) Takegoshi, K.; Nakamura, S.; Terao, T. Solid-state photodimerization of 9-methylanthracene as studied by solid-state NMR. *Solid State Nuclear Magnetic Resonance* **1998**, *11* (3-4), 189-196. DOI: 10.1016/s0926-2040(98)00031-9.

(28) Mabied, A. F.; Müller, M.; Dinnebier, R. E.; Nozawa, S.; Hoshino, M.; Tomita, A.; Sato, T.; Adachi, S.-i. A time-resolved powder diffraction study of in-situ photodimerization kinetics of 9-methylanthracene using a CCD area detector and parametric Rietveld refinement. *Acta Crystallographica Section B Structural Science* **2012**, *68* (4), 424-430. DOI: 10.1107/s0108768112027450.

(29) Kim, T.; Zhu, L.; Mueller, L. J.; Bardeen, C. J. Mechanism of Photoinduced Bending and Twisting in Crystalline Microneedles and Microribbons Composed of 9-Methylanthracene. *J Am Chem Soc* **2014**, *136* (18), 6617-6625. DOI: 10.1021/ja412216z.

(30) Salzillo, T.; Venuti, E.; Della Valle, R. G.; Brillante, A. Solid-state photodimerization of 9-methyl-anthracene. *Journal of Raman Spectroscopy* **2016**, *48* (2), 271-277. DOI: 10.1002/jrs.5003.

(31) Morimoto, K.; Kitagawa, D.; Tong, F.; Chalek, K.; Mueller, L. J.; Bardeen, C. J.; Kobatake, S. Inside Back Cover: Correlating Reaction Dynamics and Size Change during the Photomechanical Transformation of 9-Methylanthracene Single Crystals (Angew. Chem. Int. Ed. 2/2022). *Angewandte Chemie International Edition* **2021**, *61* (2). DOI: 10.1002/anie.202116140.

(32) Al-Kaysi, R. O.; Bardeen, C. J. General method for the synthesis of crystalline organic nanorods using porous alumina templates. *Chemical Communications* **2006**, (11), 1224. DOI: 10.1039/b516732a.

(33) Abad, B.; Maiz, J.; Martin-Gonzalez, M. Rules to Determine Thermal Conductivity and Density of Anodic Aluminum Oxide (AAO) Membranes. *The Journal of Physical Chemistry C* **2016**, *120* (10), 5361-5370. DOI: 10.1021/acs.jpcc.6b00643.

(34) D'Agostino, G.; Robertsson, L. Relative beam misalignment errors in high accuracy displacement interferometers: calculation and detection. *Applied Physics B* **2010**, *103* (2), 357-361. DOI: 10.1007/s00340-010-4321-2.

(35) Smith, R.; Fuss, F. K. Theoretical analysis of interferometer wave front tilt and fringe radiant flux on a rectangular photodetector. *Sensors (Basel)* **2013**, *13* (9), 11861-11898. DOI: 10.3390/s130911861 PubMed.

(36) Kaupp, G. Photodimerization of Anthracenes in the Solid State: New Results from Atomic Force Microscopy. *Angewandte Chemie International Edition in English* **1992**, *31* (5), 595-598. DOI: 10.1002/anie.199205951.

(37) Chalek, K. R.; Dong, X.; Tong, F.; Kudla, R. A.; Zhu, L.; Gill, A. D.; Xu, W.; Yang, C.; Hartman, J. D.; Magalhães, A.; et al. Bridging photochemistry and photomechanics with NMR crystallography: the molecular basis for the macroscopic expansion of an anthracene ester nanorod. *Chem Sci* **2020**, *12* (1), 453-463. DOI: 10.1039/d0sc05118g PubMed.

(38) Yang, C.; Zhu, L.; Kudla, R. A.; Hartman, J. D.; Al-Kaysi, R. O.; Monaco, S.; Schatschneider, B.; Magalhães, A.; Beran, G. J. O.; Bardeen, C. J.; et al. Crystal structure of the meta-stable intermediate in the photomechanical, crystal-to-crystal reaction of 9-tert-butyl anthracene ester. *CrystEngComm* **2016**, *18* (38), 7319-7329. DOI: 10.1039/c6ce00742b.

Chapter 7. Towards Scalable Photomechanical Processing: Polymer and Molecular Microfibers

Although porous aluminum oxide membranes provide a template for growing photomechanically active nanorods, the energy wasted when deforming the template during actuation and the surface debris generated when removing the excess material prevent this method from being a scalable solution for photomechanical actuation. This chapter contains unpublished work that serves as a basis for developing scalable solutions for harnessing photomechanical work and will discuss two major methods: polymer microfibers hosts and molecular microfibers of organic crystals. Since these findings are relatively recent, this chapter will present the work as an introductory step towards these avenues in lieu of a complete story.

7.1 Polymer Microfibers

The first approach utilizes the high processibility of viscous, aqueous solutions of polyethylene oxide polymers. Many organic photoswitches are poorly soluble in water and as a result are effectively hosted in aqueous polymers as the photoactive materials are not co-dissolved with the polymer and retain their crystal properties. As demonstrated in section **2.1.7**, for photomechanical behavior that is dependent on crystal orientation (e.g. photodimerization of anthracene derivatives), co-dissolving the photoswitch and polymer results in monomeric behavior that can thwart photomechanical actuation. High molecular weight polyethylene oxide (M_w = 8,000 kg/mol, PEO-8M) aqueous solutions have facile processing requirements, allowing for both manual and programmed writing of polymer fiber designs[1, 2]. If photoswitching crystals can be successfully incorporated into the PEO-

8M solutions and retain their photomechanical properties, then this approach can be scaled up for large, more intricate designs of hybrid photomechanical materials. To this end, the procedures outlined in sections **2.1.5** and **2.1.6** are conducted to produce microfibers of PEO-8M embedded with 4-fluoro-9-anthracene carboxylic acid (4F9AC) nanorods and crystals.

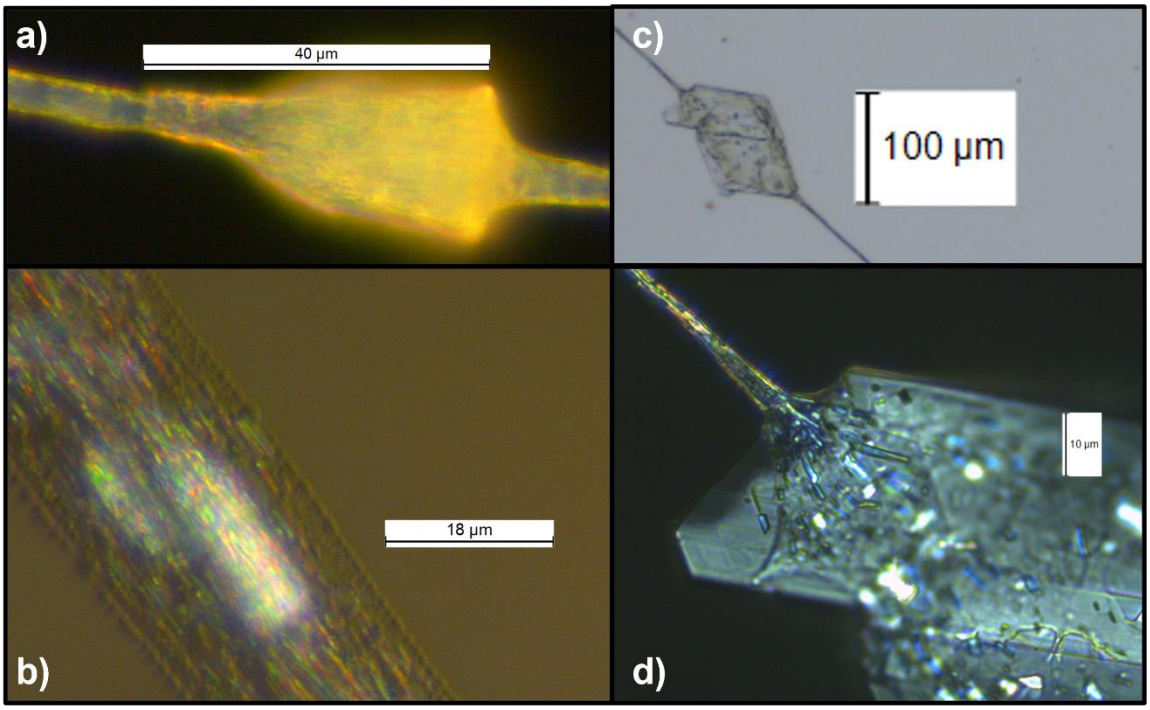

Figure 7.1 Optical microscopy images of PEO-8M microfibers embedded with (**a,b**) nanorods and (**c,d**) recrystallized/sublimed crystals of 4F9AC. To emphasis crystallinity, improve contrast, the images in **a** & **b** are collected after cross-polarization.

In anthracene derivatives, correction orientation of the crystals is crucial to harnessing the displacement generated by the photochemical reaction. Fibers and needles of fluorinated 9-anthracene-carboxylic acid derivates reversibly bend and curl when stimulated with near UV and UV irradiation, but fracture due to photosalient effects in larger microplates[3]. 4F9AC is embedded into PEO-8M solutions in one of two sources: template-grown nanorods or recrystallized/sublimed crystals. The former (**Figure 7.1a,b**)

produces better quality microfibers, as larger platelike crystals from the recrystallized/sublimed 4F9AC powder deform the polymer (**Figure 7.1c,d**).

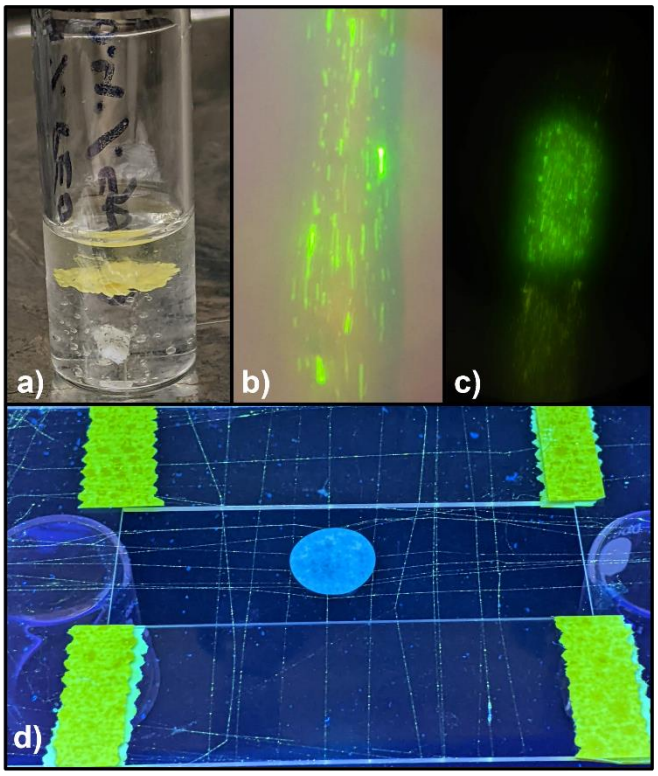

Figure 7.2 Optical images of PEO-8M+4F9AC microfibers. **A)** the 4F9AC nanorods (yellow) are insoluble in acidic (pH < 4) solution can are clearly separated from the polymer gel (bottom layer) and aqueous solution (top layer). Microfibers on the order of 20-100 µm drawn from the solution demonstrate green fluorescence typical to 4F9AC crystals (**b,c**) and can even support the weight of a 11 mg paper disk (**d**).

Precautions must be taken to avoid deprotonation of the carboxylic acid in 4F9AC, which increases solubility in the PEO-8M matrix and generates monomeric carboxylate. Weakly acidic buffers (pH 2-4) made with $NaHCO_3$ and H_3PO_4 used as a solvent for the PEO-8M typically prevents this (**Figure 7.2a**), however, at pH < 2, degradation of the polymer occurs overtime and within 1-2 weeks breaks down into smaller molecular weights of PEO. This generally decreases the viscosity of the solution and prevents the drawing of fibers. The embedded PEO-8M and 4F9AC microfibers retain the bulk

properties of the polymer host, allowing webs of the fiber to support the weight of objects much heavier than the fibers (**Figure 7.2d**). Unfortunately, these microfibers fail to actuate under UV irradiation whether they are free-standing (**Figure 7.2d**) or mounted directly onto a glass slide (**Figure 7.2b,c**).

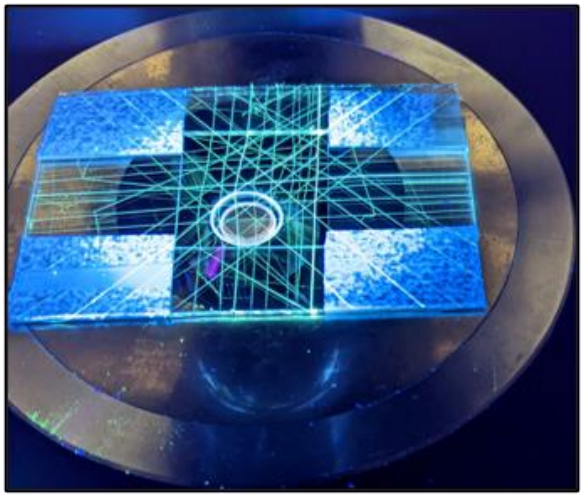

Figure 7.3 Cross-weave of 50% wt. PEO-8M/4F9AC under 365 nm irradiation. Fibers are free-standing in the central square of platform directly above the microscope objective.

Increasing the weight percentage of 4F9AC does not remedy this issue, unfortunately, as even at 50% wt. the 4F9AC nanorods cannot generate enough force to distort the PEO-8M (**Figure 7.3**). Despite the potential for reversible cycling of photomechanical bending, the 4F9AC nanorods face the same impedance matching issues that plague porous aluminum oxide templates, but PEO-8M remains a potential host for water-insoluble photomechanical crystals. Perhaps at the 100 nm -1 μm scale with high loading of the active material, the thin layer of PEO-8M will no longer dampen the photomechanical behavior, but fibers at this scale are prone to displacement by air currents and other environmental effects.

7.2 Molecular Microfibers

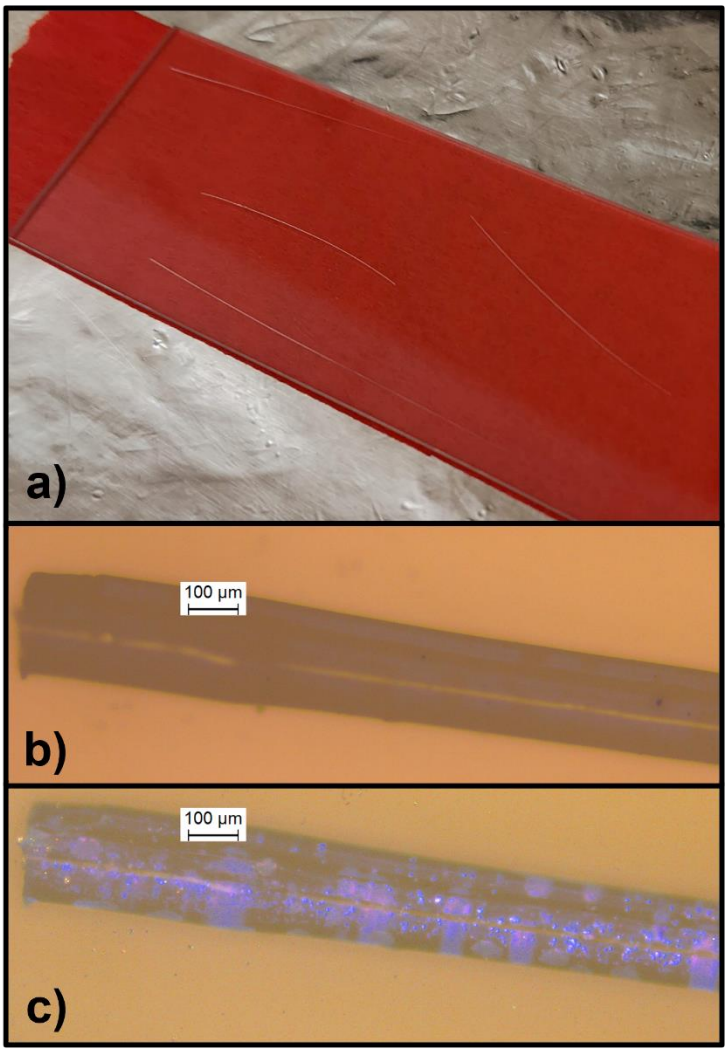

Figure 7.4 Optical images of commercial DAE microfibers (a). An individual fiber at 20x magnification b) before and c) after 365 nm irradiation. The familiar positive photochromism signifies the photoreaction occurs, albeit non-uniformly throughout the fiber.

In a more bottom-up approach, fibers of photomechanical organic crystals are hand-drawn directly from molten liquids as described in section **2.1.8**. Commercial diarylethene derivatives that are highly fluorinated demonstrate the best stability in air when molten, as spirooxazine and spiropyran oxidized readily and produced a maroon or black, tarry

substance when brought to their melting point. Drawing a needle from the molten liquid as it cools allows 500-250 μm diameter microfibers to be drawn at moderate lengths (1-10 cm). These microfibers typically taper to their shortest diameters at the end opposite to the needle and are amorphous. In **Figure 7.4a** several lengths of are mounted on top of a 25 x 75 mm glass slide and captured in an optical microscope before (**Figure 7.4**b) and after (**Figure 7.4c**) irradiation with a 365 nm flashlight. Due to the lack of crystallinity, the fibers do not demonstrate any obvious photomechanical actuation, neither along the length of the fiber nor across its diameter. However, the photochromism of DAE microfibers may still prove useful as a switchable optical fiber[4].

Coupling a HeNe (λ = 632.8 nm) laser into microfibers on the 10-100 μm diameter scale demonstrates potential multimodal waveguiding as the light (focal length ≈ 3.5 cm) is coupled several cm through the DAE fiber and projected onto a business card 20 cm away (**Figure 7.5c,d**). The increased optical loss and scattering on the business card is indicative of a change in the refractive index of the fiber due to generation of the photoproduct, but the output quality of the fiber is poor in both cases. The positive photochromism results in a meager 4% change in power, which might be improved if the crystallinity of the fibers could be improved. However, the rapid cooling during the hand drawing results in many nucleation sites and thus the amorphous quality of the fiber. These optical fibers are coupled without a cladding and if encapsulated properly, may demonstrate improved optical coupling and a larger change in optical loss when utilized as a photoswitching fiber.

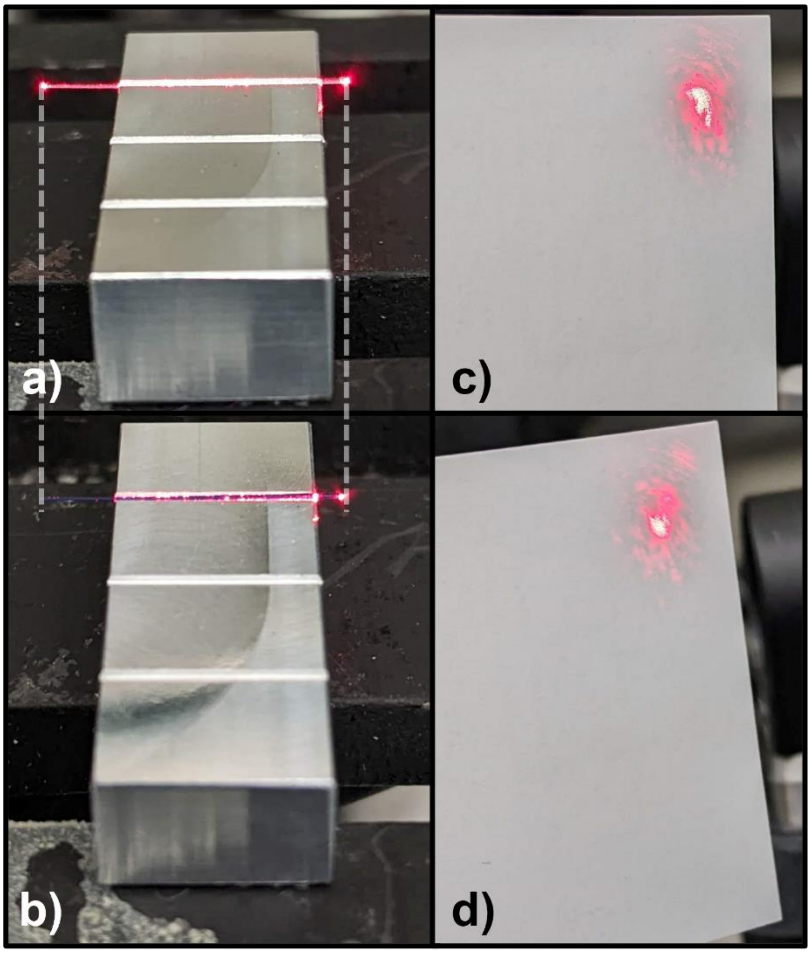

Figure 7.5 An unreacted optical fiber of DAE (**a**) mounted in a custom aluminum v-block. The coupled light is projected onto a business card 20 cm away (**c**). After exposure to 365 nm light, the fiber turns royal blue (**b**) and alters the pattern on the business card (**d**) demonstrating increased loss.

Both methods have promising characteristics for scaling photomechanical and photochromic materials into larger applications but face fundamental challenges that prevent their adoption. Future work in these areas will need to concentrate on improving: (i) the force generated by the active material in the PEO-8M microfibers and (ii) the coupling of the photoswitching optical fiber if there is any hope for future applications of these methods.

7.3 References

(1) Dotivala, A. C.; Puthuveetil, K. P.; Tang, C. Shear Force Fiber Spinning: Process Parameter and Polymer Solution Property Considerations. *Polymers* **2019**, *11* (2), 294.

(2) Huang, S.; Zhao, C.; Pan, W.; Cui, Y.; Wu, H. Direct Writing of Half-Meter Long CNT Based Fiber for Flexible Electronics. *Nano Letters* **2015**, *15* (3), 1609-1614. DOI: 10.1021/nl504150a.

(3) Zhu, L.; Tong, F.; Salinas, C.; Al-Muhanna, M. K.; Tham, F. S.; Kisailus, D.; Al-Kaysi, R. O.; Bardeen, C. J. Improved Solid-State Photomechanical Materials by Fluorine Substitution of 9-Anthracene Carboxylic Acid. *Chemistry of Materials* **2014**, *26* (20), 6007-6015. DOI: 10.1021/cm502866e.

(4) Kim, M.-S.; Maruyama, H.; Kawai, T.; Irie, M. Refractive Index Changes of Amorphous Diarylethenes Containing 2,4-Diphenylphenyl Substituents. *Chemistry of Materials* **2003**, *15* (24), 4539-4543. DOI: 10.1021/cm030304v.

Chapter 8. Conclusions and Outlook

This dissertation accomplishes four key advances for multi-excitonic and photomechanical materials. First, the intermediate and interaction distance of triplet-triplet annihilation (TTA) is investigated with tris (2-phenyl pyridine) iridium (III) ($Ir(ppy)_3$) sensitized pyrene solutions. Since the excimer formation is sensitive to the intermolecular separation of a pyrene excited singlet and ground state pair, careful analysis of the pyrene excimer and monomer ratios (E/M) provides spatial information about the TTA products. After photon upconversion, there is a two-fold increase in the concentration dependence of E/M compared to direct excitation of pyrene. This effect persists throughout solvents of varying viscosity, but its origin is presently unclear as this factor has no obvious connection to the kinetics. Regardless, the extrapolation of E/M at infinitesimal concentrations of pyrene trends to zero, indicating that the excimer is not formed directly through TTA in pyrene. Given that the critical encounter radius is 2-5 Å for pyrene excimers, the correlated triplet pair involved in TTA must for at a distance greater than this. This indication that TTA may be possible with longer range energy transfer mechanisms merits further investigation as it may enable the opportunity to design efficient, solid-state systems for photon upconversion that do not rely on elastomers or gels. Further studies with shorter excitation pulses may provide more kinetic information on the TTA process and shed further light on this phenomenon.

Following this discovery, solid films of co-deposited anthradithiophene (ADT), tetracene (TET), and [6]-phenacene (6PH) present a solid-state analogue for investigating the origin of the red-shifted luminescence (RSL) in singlet-fission (SF) materials. Films of

ADT/6PH, ADT/TET, and TET/6PH are blended at various concentrations and inspection of the films' steady-state and time-resolved photoluminescence reveals that the RSL in delayed fluorescence originates from the excimer due to its dependence on the polarizability of the environment. Furthermore, at lower concentrations of the SF material, the photoluminescence is consistent with monomeric ADT or TET, demonstrating that 6PH behaves as an inert spacer. Thus, the excimer formation channel in SF materials behaves as a parallel pathway and is not directly involved in SF, which is consistent with the behavior of pyrene in sensitized TTA solutions. It is then beneficial to design annihilating molecules with enough steric hindrance to prevent excimer formation, but still facilitate the energy transfer necessary for SF and TTA. This approach to investigating the concentration dependence of SF and TTA molecules in the solid state proves to be a useful tool in furthering our understanding of these multi-exciton processes.

Next, a model for predicting photon-to-work efficiencies for a photomechanical molecule is developed using a 1D harmonic oscillator to approximate the photomechanical cycle. Prior to our model, there was no framework to predict the performance of photomechanical molecules and the work in this thesis serves as a simple method to achieve this goal. Our model predicts a red-shift in the backreaction energy-gap under duress of applied force, establishing a maximum force that a 1D photomechanical reaction can sustain before the reaction stops. Using this stopping force as an upper limit on the work that can be performed, our model predicts a maximum theoretical efficiency of 55.4%. Contemporary studies place experimental efficiencies below 1%, leaving plenty of room for improvement as photomechanical research continues to grow.

Lastly, in an effort to realize scalable and effective actuators based on organic photomechanical crystals, nano-porous aluminum oxide templates were functionalized with lauric acid and 3-phenyl propanoic acid. Although this surface functionalization had a negligible impact on the loading of 9-methylanthracene (9MA) into the pores of the template, optimization of the solvent annealing process brought it from a meager 30% to over 70% of the theoretical maximum filling. 9MA's characteristic 7% expansion along the crystal c-axis rendered it a candidate for templated linear actuation, but no protruding nanorods were observed. The displacement of the sample mirror is tracked with a Michelson interferometer and through modelling of the interferogram, reveals that the photomechanical motion results from a change in curvature of the composite. However, as a negative photochrome nearly 100% of the 9MA ,unlike previous composites with positive photochromes like diarylethene.

Two new avenues for photomechanical materials are briefly explored using polymer-hosted and molecular microfibers. Microfibers of polyethylene oxide (M_w = 8,000 kg/mol, PEO-8M) are pulled by hand from a viscous, aqueous solution. Nanorods and micron scale needles of 4-fluoro-9-anthracene carboxylic acid (4F9AC) are injected into PEO-8M solutions before fibers are drawn. Despite retaining the crystalline properties of 4F9AC, such as the green dimer fluorescence, no photomechanical motion is observed. Despite the high processability of PEO-8M, its malleability dampens the force generated by 4F9AC and renders the composite motionless. Likewise, amorphous, molecular fibers of commercial diarylethene (DAE) can be pulled directly from the molten liquid but do not photoactuate. Fibers up to 10 cm in length and 10-100 μm in diameter can be produced

through simple hand-drawn techniques for melt pulling. These fibers retain their photochromic behavior and behave as lossy optical fibers, but do not produce a significant difference in optical coupling when the photoreaction occurs. Nevertheless, both options have promising applications should the obstacles be overcome. The facile processing conditions of PEO-8M can allow the fabrication of complicated networks of microfibers that can be readily adapted into industrial technologies. A photoswitch that is water insoluble with a large, reversible volume change would be the ideal candidate for this type of composite. Additionally, optical coupling of DAE molecular fibers can be improved with the addition of a cladding or improvement on the crystallinity of the fibers. The former is a more immediately available research venture, while the latter requires a more-involved approach and apparatus for slowing down the solidification of the fiber.